Michel Electrons Analysis in the Fine-Grained Detectors for T2K

by

Jiae Kim

B.Sc., The Yonsei University, 2008

A THESIS SUBMITTED IN PARTIAL FULFILLMENT OF
THE REQUIREMENTS FOR THE DEGREE OF

MASTER OF SCIENCE

in

THE FACULTY OF GRADUATE STUDIES

(Physics)

THE UNIVERSITY OF BRITISH COLUMBIA

(Vancouver)

December 2011

Abstract

Over the decades, neutrino physics has advanced remarkably. Confirmation of neutrino oscillation is one of the important results. It indicates that neutrinos have non-zero mass and flavor mixing.

T2K is an experiment designed to observe neutrino oscillations. It is an accelerator-based experiment with a baseline of 295 km across Japan from Tokai to Kamioka. The accelerator and the near detector are at Tokai and the far detector is at Kamioka. The near detector characterizes neutrino interactions in the absence of oscillation effects. Fine-Grained Detectors (FGDs) are a part of the near detector, which provide target mass and track particles emerging from neutrino interactions occurring in the detector.

The primary neutrino interaction channel mode of interest is the charged-current quasi-elastic (CCQE) interaction. In CCQE interactions, a charged-lepton and a proton are in the final state. The neutrino energy is reconstructed and its flavor is identified by the charged lepton. Other, non-CCQE neutrino interactions have another particles in the final state such as pions. The pions may stop in an FGD and decay to produce muons, which in turn stop and decay to produce electrons. The electrons from muon decay at rest are called Michel electrons. Michel electrons are a powerful tool to distinguish CCQE and non-CCQE interactions.

This thesis describes the studies of Michel electron activity in the near detector using cosmic rays. In Monte Carlo simulation studies, the Michel electron detection efficiency is 0.642±0.012, whereas in data, it is 0.593±0.003. The difference of the data and the Monte Carlo is 0.087±0.012.

Table of Contents

List of Tables

List of Figures

Chapter 1

Neutrino Physics

1.1 History

The neutrino, named by Enrico Fermi, means "a little neutral object" [1]. This subatomic fundamental particle was postulated theoretically first by Pauli as one of solutions to missing energy in beta decays. At first, the beta decay process was thought to be the decay of a nucleus to another nucleus by emitting a single electron:

$$N(Z, A) \rightarrow N^{'}(Z + 1, A) + e^{-} \tag{1.1}$$

where N and $N^{'}$ are two different nuclei.

By the energy conservation law, the released electron energy would have a single energy equal to

$$E_e = \frac{m_N^2 - m_{N'}^2 + m_e^2}{2m_N} \tag{1.2}$$

The electron energy should be fixed when the three masses are specified. But the observed spectrum was continuous, not constant, and not even discrete [2]. To make the decay satisfy the conservation laws and solve this spectrum problem, there should exist another undetected particle. In 1956, the hypothesis was confirmed and the existence of neutrinos was proved by Reines and Cowan. It was one of six neutrinos and anti-neutrinos, the electron anti-neutrino ($\bar{\nu}_e$) [3]. They used the inverse beta decay in their experiment:

$$\bar{\nu}_e + p \rightarrow e^{+} + n \tag{1.3}$$

The anti-neutrinos in the initial state were nuclear fission products that occurred in the nuclear detector. The detector had a target of water and $CdCl_2$. These anti-neutrino interactions were detected by identifying photons from the annihilation of the emitted positrons and a delayed photon from the capture of the neutrons.

Since then, physicists tried to explain why some reactions occur, while others do not. For example, $\mu \to e + \gamma$ had never been observed. Feinberg pointed out that the branching ratio $(\mu \to e + \gamma)/(\mu \to e + \nu + \bar{\nu})$ should be of order 10^{-4}, unless the neutrinos associated with muons are different from those associated with electrons [4]. However, the limit on the branching ratio was much less than this, indicating that there is something wrong. This is called the two-neutrino hypothesis, and it was tested in 1962 by L. Lederman, M. Schwartz and J. Steinberger. They inserted a target in a proton beam to produce charged pions. The pions decay to muons and neutrinos in flight:

$$\pi^+ \to \mu^+ + \nu \tag{1.4}$$

$$\pi^- \to \mu^- + \bar{\nu} \tag{1.5}$$

Using about 10^{14} anti-neutrinos from π^- decay, the physicists investigated two reactions:

$$\bar{\nu} + p^+ \to \mu^+ + n \tag{1.6}$$

$$\bar{\nu} + p^+ \to e^+ + n \tag{1.7}$$

If only one type of neutrino exists, the two reactions should happen equally. But they did not detect electrons. The absence of electron events suggested the existence of another type of neutrino, the muon neutrino (ν_μ) [5].

In the 1970s, the existence of the third lepton τ was confirmed and physicists inferred the existence of its associated neutrino, named the tau neutrino (ν_τ). This last neutrino was observed finally in 2000 by DONUT experiment [6]. Now, the lepton families have three charged leptons, three charged anti-leptons, three neutrinos, and three anti-neutrinos.

As the name suggests, neutrinos are extremely light. Until fairly recently, it was assumed that the neutrinos are massless. However, a series of recent experiments have shown that neutrinos have non-zero mass. The first indication of neutrino mass starts from the solar neutrino problem. The neutrinos produced in the Sun are electron neutrinos. But the flux of ν_e from the Sun observed on Earth was less than it was predicted to be. In 1968, one physicist, B. Pontecorvo, had a new theory. He said that the electron neutrinos produced in Sun converted in traveling to Earth to a different species [7]. Now we call this "neutrino oscillation".

Neutrino oscillation is a consequence of the non-zero neutrino masses and neutrino mixing. The flavor eigenstates , which are ν_e, ν_μ and ν_τ, are superpositions of the mass eigenstates, which are energy eigenstates. This causes flavor mixing. This is described in more detail in Section 1.3.2.

1.2   In the Standard Model

In the Standard Model, there are three types of neutrino. They do not have charge, so they cannot feel the electromagnetic field. They do not have color, so they cannot feel the strong field either. They only interact via the weak interactions. In the weak interactions, only left-handed neutrinos can be coupled to the weak interaction gauge bosons. While other fermions can be both right-handed and left-handed via other interactions, neutrinos only can interact as left-handed particles [8].

1.2.1   Neutrino Mass

The Standard Model Lagrangian consists of three parts:

$$\mathscr{L}_{SM} = \mathscr{L}_{kinetic} + \mathscr{L}_{Higgs} + \mathscr{L}_{Yukawa} \tag{1.8}$$

$\mathscr{L}_{Yukawa}$ is the interaction of the Higgs scalar fields to the Dirac fermion fields. Generally, the Yukawa couplings are not diagonal. Since the discussion is focused only on the lepton sector, consider the lepton component of the Yukawa couplings:

$$-\mathscr{L}_{Yukawa} = Y_{ij}^l \overline{\mathscr{E}}_{Li} \phi l_{Rj} + h.c. \tag{1.9}$$

where L/R denote left-handed and right-handed and i/j denote different mass eigenstates.

In the language of field theory, leptons are expressed by a doublet containing the left handed charged lepton and its corresponding neutrino and a singlet containing the right handed component of the charged lepton:

$$\mathscr{E}_L = \begin{pmatrix} l_L \\ \nu_L \end{pmatrix}, l_R$$

Here Y in Equation 1.9 is a non-diagonal coefficient matrix and ϕ is the Higgs field. After spontaneous symmetry breaking when the Higgs field obtains a vacuum expectation value v, the Higgs field is rewritten as

$$\phi = \frac{1}{\sqrt{2}}(v + h(x)) \tag{1.10}$$

where v is a constant and $h(x)$ describes the fluctuations of the field about the vacuum expectation value. Then, the Yukawa couplings break into one with and one without couplings to $h(x)$:

$$
\begin{aligned}
-\mathscr{L}_{Yukawa} &= v Y_{ij}^{l} \bar{l}_{Li} l_{Rj} + h.c. + (\text{couplings to } h(x)) \\
&= (m_l)_{ij} \bar{l}_{Li} l_{Rj} + h.c. + (\text{couplings to } h(x)) \tag{1.11}
\end{aligned}
$$

It is assumed that there are no right-handed neutrinos, since they would not interact in the Standard Model. A mass term requires left and right-handed components of the filed. Therefore, there are no neutrino mass terms. This is the reason why neutrinos are considered massless in the Standard Model. Generally, the mass matrix is non-diagonal. But it is easy to diagonalize the matrix by introducing transformation matrices, V_{lL} and $V_{lR}^{\dagger}$. Since right-handed neutrinos are not included in this theory, we have the freedom of choosing the transformation matrix V for neutrinos such that $V_l = V_{\nu}^{\dagger}$. That means the couplings of leptons and weak interaction gauge bosons are isolated for each flavor after transformations. This is why flavor mixing is forbidden in lepton sector when the neutrino is massless.

Despite the masslessness of neutrinos in the Standard Model, the mass of neutrinos have been questioned since Fermi developed his theory of neutrinos. Several experiments have attempted to measure the mass of neutrinos directly via beta decays, pion decays, and tau lepton decays. However, they did not find any evidence of neutrino mass. Another way to probe neutrino mass is to search for neutrino oscillations. In 1957, B. Pontecorvo proposed the possibility of oscillations between neutrinos and anti-neutrinos [9].

1.2.2 Neutrino Interactions

Since neutrinos have no charge, they cannot be seen via electromagnetic interactions used in current detector technologies. Generally, electromagnetic interactions are required to detect particles. They can only be inferred by seeing other particles which emerge from neutrino interactions that interact electromagnetically or strongly. Neutrino interactions only occur through weak gauge bosons. There are two types of weak interactions, Charged-Current (CC) interactions and Neutral-Current (NC) interactions. The basic Feynman diagrams at tree level are shown in Figure 1.1.
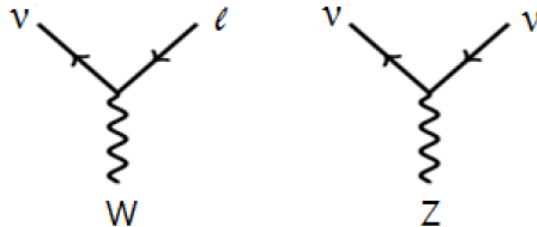
Figure 1.1: CC and NC Feynman diagrams at tree level.

Channels	
CC quasi-elastic	$\nu + n \rightarrow l + p$
CC resonant pion	$\nu + n \rightarrow l + n + \pi^+$
CC coherent pion	$\nu + A \rightarrow l + A + \pi^+$
NC resonant pion	$\nu + n \rightarrow \nu + n + \pi^0$
NC coherent pion	$\nu + A \rightarrow \nu + A + \pi^0$

Table 1.1: List of the CC and NC neutrino interactions. The top channels are CC interactions in which a charged lepton emerges. The bottom ones are NC interactions in which a neutrino emerges. A denotes a nucleus.

The outgoing charged leptons from CC channels must have the same flavor as the incoming neutrinos. That is, the flavor of the incoming ν can be identified by the outgoing charged lepton. In the same manner, the flavor of outgoing neutrinos and incoming neutrinos in NC interactions must be identical. Then, in the CC channels, the flavor of the neutrino can be inferred by charged lepton. For example, if μ^- is detected in the final state, the incoming neutrino is a ν_μ. However, in the NC channels, we cannot know the neutrino flavors because there is no charged lepton in the final state. Some example interactions for both CC and NC channels are shown in Table 1.1. The examples in the table are channels that are typically observed in the T2K experiment, where the neutrino flux is peaked at 0.6 GeV.

Figure 1.2 shows the neutrino interaction cross sections as a function of neutrino energy [10]. At around 0.6 GeV, the cross section of charged-current quasi-elastic (CCQE) interactions is the highest among CC interac-
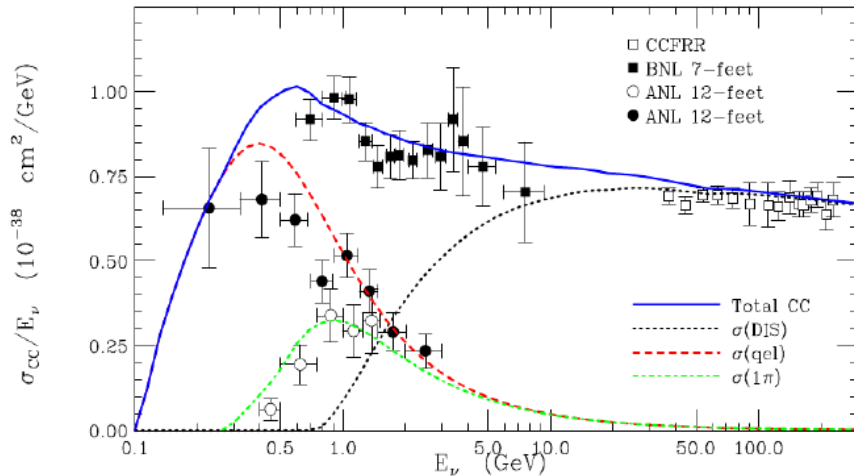
Figure 1.2: Cross sections for different neutrino interactions at various energy range [10].

tions. CCQE interactions are the main signal in T2K neutrino oscillation measurement. They are chosen because the neutrino energy E_ν can be well reconstructed by two-body kinematics. In CCQE ($\nu + n \to l + p$), the energy of the neutrino can be approximately calculated using the energy and direction of the final state lepton by

$$E_\nu^{rec} \approx \frac{m_p^2 - (m_n - m_l)^2}{2(m_n - E_l + \sqrt{E_l^2 - m_l^2} \cos \theta_l)} \tag{1.12}$$

where n denotes the neutron, p denotes the proton, and l denotes the charged lepton after the interaction.

A smaller number of single pion interactions occur as well. In these cases, since there are three particles in the final state, the assumed kinematics is incorrect. Thus, the neutrino energy cannot be well estimated via this formula. The hardest cases are the neutral current channels. Since there is no outgoing charged lepton, we will not know the neutrino flavors.

Neutrino Sources	Cross Section (cm^2)	Neutrino Flux at Earth $(\text{cm}^{-2}\text{sec}^{-1})$
$H + H + e^- \rightarrow D + \nu$	1.72×10^{-45}	1.7×10^8
^7Be decay	2.9×10^{-46}	3.9×10^9
^8B decay	1.35×10^{-42}	1.3×10^7
^{13}N decay	2.1×10^{-46}	1.0×10^9
^{16}O decay	7.8×10^{-46}	1.0×10^9

Table 1.2: The estimated solar neutrino fluxes and cross sections for the reaction $^{37}\text{Cl}(\nu, e^-)\,^{37}\text{Ar}$.

1.3 Neutrino Oscillation

1.3.1 Evidence of the Neutrino Oscillation

In the 1960s, J. N. Bahcall did most of the calculations detailing the production and spectra of neutrinos produced in solar fusion processes [11]. Table 1.2 shows cross sections and flux for several sources. At around the same time, R. Davis and colleagues detected solar neutrinos and measured their flux based on the neutrino capture reaction $^{37}\text{Cl}(\nu, e^-)^{37}\text{Ar}$. They concluded that the neutrino flux from ^8B decay in the Sun was equal to or less than 2×10^6 cm^{-2}sec^{-1} [12], while Bahcall's prediction was $(1.3 \pm 0.6) \times 10^7$ [13]. This was the beginning of the solar neutrino problem.

Solar Neutrino Problem

The Sun is a source of neutrinos via fusion processes such as [14]

$$p + p \rightarrow \ ^2\text{H} + e^+ + \nu_e \tag{1.13}$$

$$p + e^- + \rightarrow \ ^2\text{H} + \nu_e \tag{1.14}$$

Figure 1.3 shows the neutrino flux at the Earth for different reactions producing neutrinos [15]. The Homestake experiment was the first to observe the solar neutrino flux at the Earth form the Sun [16]. They observed the solar neutrinos from the decay

$$^8\text{B} \rightarrow^8 \text{Be} + e^+ + \nu_e \tag{1.15}$$

and compared the result to the prediction that was made by Bahcall in the Standard Solar Model. The SSM is a theoretical framework for understanding the physics of the Sun. The model treats the Sun as a spherical bulb with four basic assumptions [17]:

- The Sun is in hydrostatic equilibrium. In other words, gravity and pressure in the Sun are locally balanced.

- Energy in the Sun is transferred via radiation, conduction, convection, and neutrino losses.

- The only energy sources are thermonuclear reactions.

- The Sun was initially homogeneous in its distribution.

The measured neutrino flux traveling to the Earth was less than the prediction by the model. This is the solar neutrino problem [18].

After the Homestake experiment, the Kamiokande experiment, using a large water Čerenkov detector, published a result consistent with the Homestake experiment [19]. The solar neutrino problem was finally solved by SNO and Super Kamiokande (higher statistics than Kamiokande) [20]. Whereas the Homestake experiment used radiochemical detectors, SNO and Super Kamiokande used water Čerenkov detectors. SNO used heavy water (D_2O) that allowed sensitivity of NC processes whereas SK used normal water (H_2O). SNO observed ^8B neutrinos via three different interaction channels: CC interactions, NC interactions and elastic scatterings

$$\nu_e + d \rightarrow e^- + p + p \tag{1.16}$$

$$\nu_\alpha + d \rightarrow \nu_\alpha + p + n \tag{1.17}$$

$$\nu_\alpha + e^- \rightarrow \nu_\alpha + e^- \tag{1.18}$$

where d denotes a deuteron.

Figure 1.4 is solar flux result from SNO [21].

Without oscillations, all measured neutrinos would be electron neutrinos. However, by measuring the neutrino flux via CC, NC and elastic scattering channels SNO found that there was a deficit of electron neutrinos that appeared as other neutrino flavors. In the ν_e transition to ν_μ or ν_τ, the result from NC channels are independent of neutrino oscillation, so it agrees with the ^8B solar neutrino flux predicted by the SSM [15]. The initial CC result
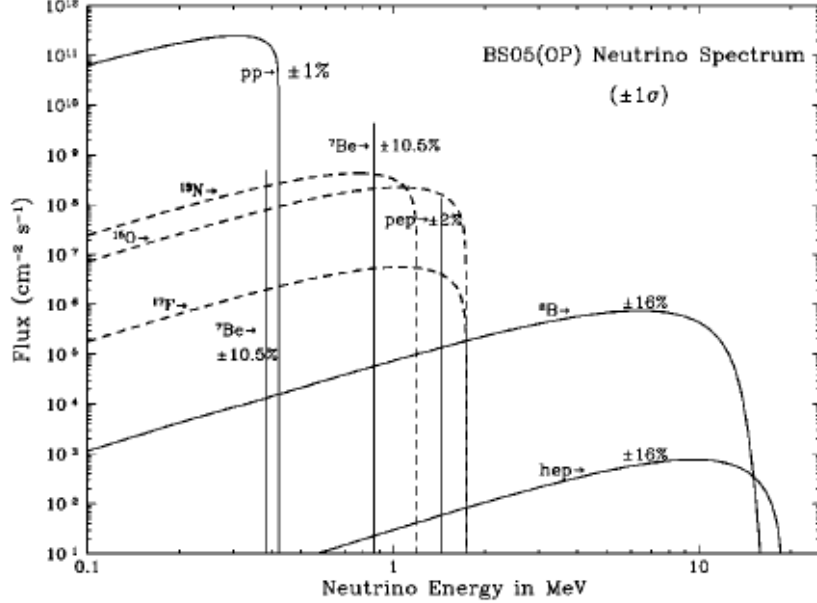
Figure 1.3: Solar neutrino flux at various energy range for different interactions [15]. The horizontal axis is the ν_e flux and the vertical axis is the $\nu_\mu(\nu_\tau)$ flux. The dotted lines are limits from the SSM prediction. The colored bands represent the measured fluxes via different interactions at 68% C.L. and the solid-lined contours are the 68%, 95% and 99% joint probability for ϕ_e and $\phi_{\mu(\tau)}$.

from SNO combined with the result from the Super-Kamiokande provided evidence for neutrino oscillation of solar neutrinos [22].

Atmospheric Neutrino Problem

Primary cosmic rays entering the Earth's atmosphere are mostly made of protons (up to 90 %). When they enter the atmosphere, hadronic interactions produce hadrons such as pions and kaons which then decay to produce neutrinos. The pions decay into μ and ν_μ, then subsequently the μ decay into e, ν_e, and ν_μ. These neutrinos are called atmospheric neutrinos.

Since the dominant interaction producing neutrinos is the decay chain $\pi^+ \rightarrow \mu^+ + \nu_\mu$ and subsequently $\mu^+ \rightarrow e^+ + \overline{\nu}_\mu + \nu_e$ [23], atmospheric neutrinos are electron and muon neutrinos, but mostly ν_μ:

9
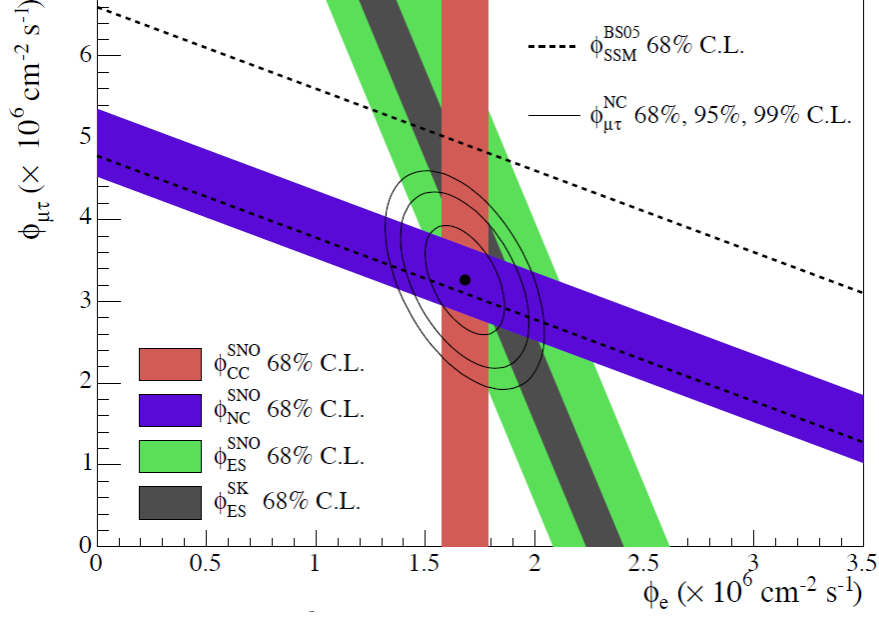
Figure 1.4: Solar neutrino result. The x axis is the flux of ν_e and the y axis is the flux of ν_μ or ν_τ from SNO measurements. The red band is from the SNO CC result. The blue is from the SNO NC result and the light green is from the SNO elastic scattering result. The dark green band is from the Super-Kamiokande elastic scattering result. The bands represent the 1σ error. The sum of the neutrino fluxes is consistent with the SSM expectation (dashed line) [21].

$$\pi^+ \rightarrow \mu^+ + \nu_\mu$$
$$\mu^+ \rightarrow e^+ + \overline{\nu}_\mu + \nu_e \tag{1.19}$$

$$\pi^- \rightarrow \mu^- + \overline{\nu}_\mu$$
$$\mu^- \rightarrow e^- + \nu_\mu + \overline{\nu}_e \tag{1.20}$$

While the muon neutrinos and anti-neutrinos are produced during both pion and muon decays, the electron neutrinos are produced only in muon decays. Hence, the amount of $\nu_\mu, \overline{\nu}_\mu$ is approximately twice as much as ν_e.

Since cosmic rays come from everywhere, the ratio of ν_μ flux and ν_e flux would be isotropic without oscillations. But an anisotropic flux of ν_μ was observed by Super-Kamiokande experiment. It is caused by the transition of ν_μ to ν_τ. (i.e. neutrino oscillation)

1.3.2   Oscillation Probability

In 1962, Z. Maki, M. Nakagawa, and S. Sakata formulated a theory for neutrino flavor oscillation [24], and in 1968, Pontecorvo also developed a theory of neutrino oscillations to explain the solar neutrino problem [7]. If neutrinos have non-zero and non-degenerate mass and their flavor eigenstates are not identical to their mass eigenstates, then the neutrinos can change their flavor [25].

The neutrino flavor states, $|\nu_\alpha\rangle$, can be written by as a linear combination of mass eigenstates, $|\nu_i\rangle, i = 1, 2, 3$:

$$|\nu_\alpha\rangle = \sum U_{\alpha i}^* |\nu_i\rangle \tag{1.21}$$

where U is a unitary matrix. This mixing matrix is referred to as the PMNS matrix [24], similar to the CKM matrix in the quark sector [26]. There are many ways to parametrize the PMNS matrix. Usually, it is written in the following form:

$$U = \begin{pmatrix} c_{12}c_{13} & s_{12}c_{13} & s_{13}e^{-i\delta} \\ -s_{12}c_{23} - c_{12}s_{23}s_{13}e^{i\delta} & c_{12}c_{23} - s_{12}s_{23}s_{13}e^{i\delta} & s_{23}c_{13} \\ s_{12}s_{23}- & c_{23}c_{13} & \end{pmatrix}$$

where $c_{ij} = \cos\theta_{ij}, s_{ij} = \sin\theta_{ij}$.

To see how neutrinos oscillate, we would like to study the time evolution of a neutrino flavor eigenstate. Assume that a neutrino is in a flavor eigenstate, $|\nu_\alpha\rangle$, at $t = 0$. Then we apply the time evolution operator to the state. Mass eigenstates are also energy eigenstates, so they have a simple time dependence. This gives

$$|\nu_\alpha(t)\rangle = e^{-iHt}|\nu_\alpha(0)\rangle = \sum U_{\alpha i}^* e^{-i(E_i t - p_i L)}|\nu_i(0)\rangle \tag{1.22}$$

where E_i and p_i are the energy and momentum of $|\nu_i\rangle$.

The mass eigenstates can be expressed by the flavor eigenstates using the inverse relation:

$$|\nu_i\rangle = \sum U_{i\beta}|\nu_\beta\rangle \qquad (1.23)$$

Substituting Equation 1.23 into Equation 1.22, we get

$$|\nu_\alpha(t)\rangle = \sum U_{i\beta}e^{-i(E_it-p_iL)}U^*_{\alpha i}|\nu_\beta\rangle \qquad (1.24)$$

Since neutrino masses cannot exceed the upper limit of 1 eV [27] and the typical value of neutrino energies is MeV or greater, they travel close to the speed of light and are relativistic. This allows us to approximate $t \approx L$. Moreover, neutrino masses are small enough so that $E = \sqrt{p_i^2 + m_i^2} \approx p_i + m_i^2/2p_i$. Then, Equation 1.24 can be rewritten as

$$|\nu_\alpha(L)\rangle = \sum U_{i\beta}e^{-i(p_i+m_i^2/2p_i-p_i)L}U^*_{\alpha i}|\nu_\beta\rangle = \sum U_{i\beta}e^{-im_i^2L/2p_i}U^*_{\alpha i}|\nu_\beta\rangle$$
$$(1.25)$$

Lastly, we assume the energy are all same, $E_i = E$:

$$|\nu_\alpha(L)\rangle = \sum U^*_{\alpha i}e^{-im_i^2L/2E}|\nu_i\rangle = \sum U_{i\beta}e^{-im_i^2L/2E}U^*_{\alpha i}|\nu_\beta\rangle \qquad (1.26)$$

From Equation 1.26, we can get the amplitude of $\nu_\alpha \rightarrow \nu_\beta$ and the probability for the transition from ν_α to ν_β

$$\text{Amp}(t) = \langle\nu_\beta|\nu_\alpha(t)\rangle = \sum U_{i\beta}e^{-im_i^2L/2E}U^*_{\alpha i} \qquad (1.27)$$

$$\text{Prob}(\nu_\alpha \rightarrow \nu_\beta) = |\text{Amp}(t)|^2 = |\sum U_{i\beta}e^{-im_i^2L/2E}U^*_{\alpha i}|^2 \qquad (1.28)$$

Following from Equation 1.28, the transition probability from the flavor α to the flavor β after L is

$$
\begin{aligned}
P(\nu_\alpha \rightarrow \nu_\beta) &= \delta_{\alpha\beta} - 4\sum \text{Re}(U^*_{\alpha i}U_{\beta i}U_{\alpha j}U^*_{\beta j})\sin^2\frac{\Delta m_{ij}^2 L}{4E} \\
&\quad -2\sum_{i>j}\text{Im}(U^*_{\alpha i}U_{\beta i}U_{\alpha j}U^*_{\beta j})\sin^2\frac{\Delta m_{ij}^2 L}{2E} \qquad (1.29)
\end{aligned}
$$

where $\Delta m_{ij}^2 = m_i^2 - m_j^2$. For oscillation between anti-neutrinos, the probability is similar but with a plus sign for the last term. So far, a total of 7 parameters have been found, three mixing angles, three neutrino masses,

and single CP phase. But, by the condition of $\Delta m_{12}^2 + \Delta m_{13}^2 + \Delta m_{23}^2 = 0$, only two of three masses are actually independent. That is, the total independent parameters in neutrino oscillations in the case of 3 flavors and mass eigenstates is six.

The first conclusive evidence that neutrinos do oscillate and therefore have to have mass, comes from the Super Kamiokande experiment [28]. They observed a zenith-angle dependence of the rate of muon neutrinos produced in the atmosphere by cosmic rays relative to expectation. Afterwards, the atmospheric neutrino oscillation was confirmed by K2K [29].

The solar neutrino oscillation was confirmed by SNO, the Super Kamiokande, and KamLAND [30].

The results from the experiments are

$$|\Delta m_{31}^2| = 2.40 \times 10^{-3} \text{eV}^2, \Delta m_{21}^2 = 7.65 \times 10^5 \text{eV}^2 \qquad (1.30)$$

$$|\Delta m_{21}^2| \ll |\Delta m_{31}^2| \qquad (1.31)$$

More detail about these experiments will be discussed in Section 1.3.3.

The sign of the solar mass difference is known. But the sign of the atmospheric mass difference is unknown. Two ways of arranging the masses, normal ($m_1 < m_2 < m_3$) and inverted ($m_3 < m_1 < m_2$) hierarchy, are possible as shown in Figure 1.5.
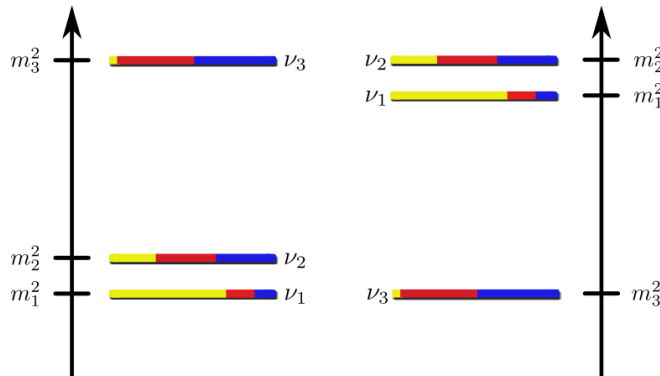
Figure 1.5: Two different mass hierarchies. The left is normal hierarchy, and the right is inverted. ν_1, ν_2 and ν_3 are mass eigenstates and colors represent flavor eigenstates. Yellow is ν_e, red is ν_μ and blue is ν_τ.

If the normal hierarchy is correct, m_3 is larger than m_1 so that $m_{31}^2 > 0$. However, if the inverted hierarchy is correct, $\Delta m_{31}^2 < 0$. The neutrino

oscillation probability in matter is different to the probability in vacuum and the mass hierarchies affect the oscillation probability in the matter [31].

1.3.3 A Review of Experiments

In the Standard Model, which has three neutrinos, the neutrino mixing is determined by six independent parameters; three mixing angles, one CP violation parameter, and two mass difference squares. Over the last decade, many experiments have been performed to measure the parameters and understand neutrino oscillations. Currently, we know two mixing angles, θ_{12}, θ_{23}, limits on θ_{13}, the mass splitting, Δm_{21}^2, and the absolute value of the other mass splitting $|\Delta m_{32}^2|$. θ_{12} and Δm_{21}^2 are solar neutrino parameters and are sometimes called θ_{sol} and Δm_{sol}^2. Likewise, θ_{23} and Δm_{32}^2 are atmospheric neutrino parameters, and are sometimes called θ_{atm} and Δm_{atm}^2.

But, we do not know yet the CP violation parameter, δ, the sign of Δm_{atm}^2, and the last mixing angle θ_{13}. Many experiments around the world are investigating neutrino oscillations to improve our knowledge.

Neutrino experiments can be categorized by four neutrino sources and two mass difference regions. The four neutrino sources are solar, atmospheric, accelerator, and reactor.

Table 1.3 is a summary of recent experiments. Some are no longer in operation, while others are still active and some are under construction. Figure 1.6 also summarizes mass and mixing sensitivity regions of several experiments.

SNO, Super-K, Kamiokande, KamLAND and other experiments using solar or reactor neutrinos have produced measurements of $\Delta m_{21}^2, \theta_{12}$. The best-fit parameters are $\Delta m_{21}^2 = 7.59^{+0.20}_{-0.21} \times 10^{-5} \text{eV}^2$ and $\tan^2 \theta_{12} = 0.457^{+0.040}_{-0.029}$ [10]. Table 1.4 summarizes these results [32].

Meanwhile, Super-K, a large water Čerenkov detector, measured Δm_{32}^2 and θ_{23}. The allowed mass region is between 1.9×10^{-3} and $3.0 \times 10^{-3} \text{eV}^2$ and $\sin^2 2\theta_{23} > 0.90$.

The K2K experiment in the 1.3 GeV energy range, confirmed these measurements. The best-fit parameters are $|\Delta m_{32}^2| = 2.8 \times 10^{-3} \text{eV}^2$ and $\sin^2 2\theta_{23} = 1.00$. MINOS also measured the parameters in atmospheric region. Their best-fit values are $|\Delta m_{32}^2| = 2.43 \times 10^{-3} \text{eV}^2$ at $\sin^2 2\theta_{23} > 0.90$. Table 1.5 lists of some important results of atmospheric neutrino parameters [33].

---

[1]Daya Bay has two near detectors. These baselines are the distances between a far detector and the two near detectors.

Experiment	Sources	Flavor	Detector	E_ν	L
SNO	solar	$\nu_{\mu,e,\tau}$	Čerenkov	3.5MeV	$\sim 10^8$km
Super-K	atmospheric/ solar	$\nu_{\mu,e,\tau}$	Čerenkov	~ 1GeV	$\sim 10^4$km
KamLAND	reactor	$\overline{\nu}_e$	Scintillator	3 MeV	180km
CHOOZ	reactor	$\overline{\nu}_e$	Scintillator	3 MeV	1 km
Double CHOOZ	reactor	$\overline{\nu}_e$	Scintillator	3 MeV	1.05 km
Daya Bay	reactor	$\overline{\nu}_e$	Čerenkov	3 MeV	1.6 km/ 1.9 km [1]
RENO	reactor	$\overline{\nu}_e$	Scintillator	3 MeV	1.4 km
OPERA	accelerator	ν_μ	Scintillator	17 GeV	730 km
MINOS	accelerator	ν_e, ν_μ	Scintillator	~ 5GeV	735km
MiniBooNE	accelerator	ν_e, ν_μ	Čerenkov	800MeV	540m
K2K	accelerator	ν_μ	Scintillator, Čerenkov	1GeV	250km
T2K	accelerator	ν_μ	Scintillator, Čerenkov	1GeV	300km

Table 1.3: List of neutrino experiments. L is distance between the ν beam and the far detector, called baseline.

A new generation of neutrino experiments have focused on the measurement of the last mixing angle, θ_{13}. It can be measured directly using $\overline{\nu}_e$ oscillation. In the ν_μ appearance oscillation, the dominant term is $2\sin^2\theta_{23}\sin^2 2\theta_{13}$ and $\sin^2\theta_{23}$ is close to 1. So the measurements on θ_{13} are in terms of $2\sin^2\theta_{23}\sin^2 2\theta_{13}$ in the case of $\nu_\mu \to \nu_e$ appearance.

The first experiments searching for $\overline{\nu}_e$ disappearance was CHOOZ. The experiment was a short baseline (1 km) reactor neutrino experiment and the neutrino energy was around 3 MeV. Since CHOOZ did not see evidence of neutrino oscillations, it set an upper limit of $\sin^2\theta_{13} < 0.15$.

K2K was another experiment looking for θ_{13}. However, it used accelerator with accelerator neutrino beam. The experiment searched for ν_e appearance signals in ν_μ beam. They also set a limit the measurement, $\sin^2 2\theta_{13} < 0.26$. The summary is on Table 1.6.

Recently, MINOS and T2K published new results on θ_{13}. The MINOS re-

---
[1]The mass region is allowed at $\sin^2 2\theta_{23} = 1.00$
[2]68% C.L.

Data	$|\Delta m_{21}^2|$ (eV^2)	$\tan^2 2\theta_{21}$
Global	$5.89_{-2.16}^{+2.13} \times 10^{-5}$	$0.457_{-0.041}^{+0.038}$
Global + KamLAND	$7.59_{-0.21}^{+0.20} \times 10^{-5}$	$0.457_{-0.029}^{+0.040}$

Table 1.4: Measured solar neutrino parameters. The first row is global-fit parameters, and the second row is combined result of global-fit and KamLAND [32].

Data	Δm_{32}^2 (eV^2)	$\sin^2 2\theta_{23}$
Super-K	$1.9 \times 10^{-3} < \Delta m^2 < 3.0 \times 10^{-3}$	> 0.90
K2K	$1.9 \times 10^{-3} < \Delta m^2 < 3.5 \times 10^{-3}$ [1]	1.00
MINOS	$|\Delta m^2| = (2.43 \pm 0.13) \times 10^{-3}$ [2]	> 0.90

Table 1.5: Measured atmospheric neutrino parameters (90% C.L.) [33].

sults are $2\sin^2 \theta_{23}\sin^2 2\theta_{13} = 0.041_{-0.031}^{+0.047}$ or $2\sin^2 \theta_{23}\sin^2 2\theta_{13} = 0.079_{-0.053}^{+0.071}$ for normal and inverted mass hierarchy respectively with $|\Delta m_{32}^2| = 2.32 \times 10^{-3}$ eV^2 [34], $\theta_{23} = 0.785 \pm 0.100$ [35]. They further report the upper limit on θ_{13}, $2\sin^2 \theta_{23}\sin^2 2\theta_{13} < 0.12(0.20)$ at 90% C.L. for normal(inverted) hierarchy [36]. Meanwhile, T2K find $0.03(0.04) < \sin^2 2\theta_{13} < 0.28(0.34)$ at 90% C.L. for normal(inverted) mass hierarchy with $\sin^2 2\theta_{23} = 1.0$ and $|\Delta m_{23}^2| = 2.4 \times 10^{-3}$ eV^2 [37]. Because the result depends on the mass hierarchies they publish two different results based on normal or inverted hierarchy.

Data	θ_{13} limit (90% C.L.)
CHOOZ	$\sin^2 2\theta_{13} < 0.15$
K2K	$\sin^2 2\theta_{13} < 0.26$

Table 1.6: θ_{13} measurements [33].
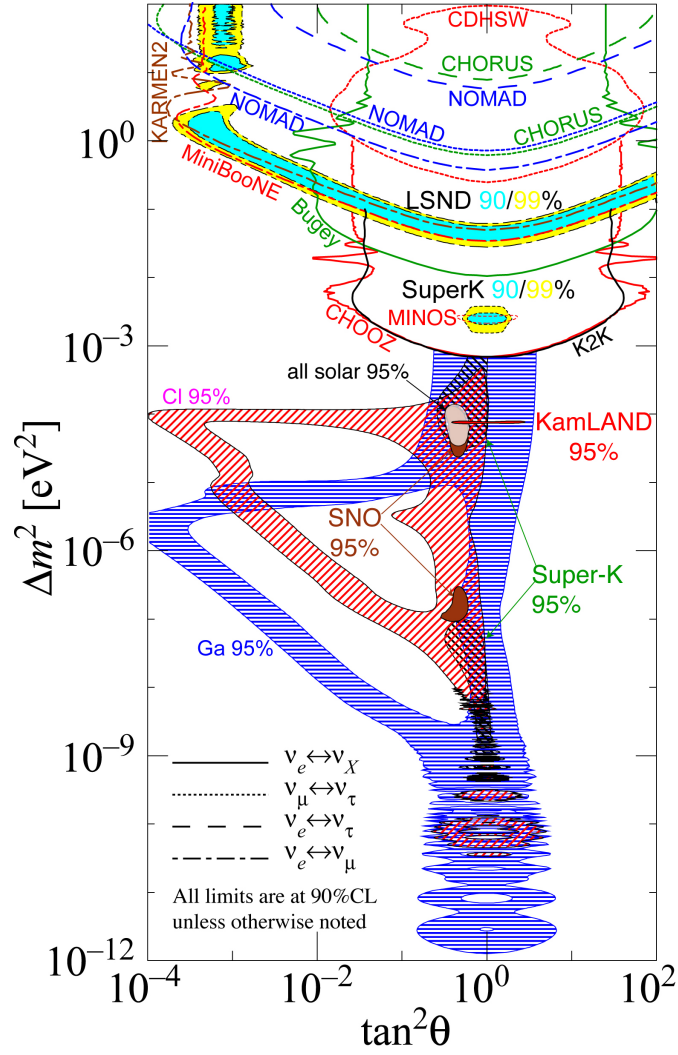
Figure 1.6: Allowed neutrino mass and mixing region for different neutrino experiments. This figure is taken from http://hitoshi.berkeley.edu/neutrino/.

Chapter 2

T2K
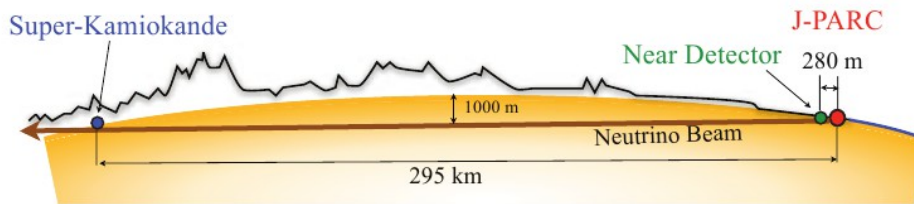
Figure 2.1: Overview of the T2K experiment across Japan.

T2K is a "long-baseline"neutrino oscillation experiment from Tokai to Kamioka in Japan. The experiment uses a high intensity proton beam to produce the neutrino beam using the J-PARC accelerator facilities in Tokai. Accelerated protons interact on a target to produce pions. The produced pions decay to μ and ν_μ in flight. The neutrinos are measured at the near detector (ND280), located 280 m away from the beam. Measurements at the near detector provide understanding of the neutrino beam and interaction properties in the absence of neutrino oscillation effects. After that, the neutrino beam travels 295 km to the far detector, the Super-Kamionkande detector (SK) at Kamioka.

The neutrinos from the J-PARC beam are mostly muon neutrinos, which typically oscillate to ν_τ at SK. However, we cannot identify the ν_τ at SK, because it is kinematically forbidden to produce the tau leptons via charged weak interactions. The reason for this is that the tau mass is much larger than our mean neutrino energy, 0.6 GeV. Therefore, $\nu_\mu \rightarrow \nu_\tau$ oscillations are measured by ν_μ disappearance. The measured neutrino events at SK are expected to be reduced by $\nu_\mu \rightarrow \nu_\tau$ oscillations. Within ν_μ disappearance, we make a more precise measurement of the mixing angle θ_{23} and Δm_{32}^2. This is one goal of T2K. On the other hand, if $\nu_\mu \rightarrow \nu_e$ oscillations occur, more ν_e are detected at SK. This ν_e appearance is used to measure the last mixing angle θ_{13}. This is the other goal of the experiment.

2.1 Measurement Theory

The neutrino transition probabilities of ν_e appearance and ν_μ disappearance in vacuum are

$$P(\nu_\mu \to \nu_e) \approx \sin^2 2\theta_{13} \sin^2 \theta_{23} \sin^2\left(\frac{\Delta m_{31}^2 L}{4E_\nu}\right) \tag{2.1}$$

$$P(\nu_\mu \to \nu_\mu) \approx 1 - \sin^2 2\theta_{23} \sin^2\left(\frac{\Delta m_{31}^2 L}{4E_\nu}\right) \tag{2.2}$$

where L is the neutrino path length and E_ν is the neutrino energy. The probability depends on two mixing angles, one of the three mass-squared differences, and L/E_ν. Reactor- and accelerator-based experiments with a fixed, well-known baseline can make precise measurements of Δm^2. The neutrino energy can be tuned to choose the L/E that maximizes the oscillation probability.

For T2K, L is 295 km, which is the distance between Tokai and Kamioka. This is the reason why T2K is called a long-baseline experiment. The distribution of E_ν from the neutrino beam peaks around 0.6 GeV to maximize $P(\nu_\mu \to \nu_e)$ and minimize $P(\nu_\mu \to \nu_\mu)$. N_{SK}^{obs} is the number of observed events at SK, and N_{SK}^{exp} is the number of expected events at SK.

More precisely, the number of neutrino events at SK is as a function of the reconstructed neutrino energy. It is given as

$$N_{SK}^{exp}(E_\nu^{rec}; \Delta m^2, \theta) =$$
$$\int dE_\nu M_{SK}(E_\nu^{rec}, E_\nu) \times P(E_\nu; \Delta m^2, \theta)\phi_{SK}(E_\nu)\sigma(E_\nu)\epsilon_{SK}(E_\nu)$$

where ϕ_{SK} is the neutrino flux, σ is the neutrino cross section, ϵ is the neutrino detection efficiency and M is the detector response function representing the probability to observe E_ν as E_ν^{rec}, the reconstructed neutrino energy [38].

The estimation of $\phi_{SK}, \sigma, \epsilon$ and M is necessary. Since the T2K neutrino beam is originally generated from pion and kaon decays, the cross sections of the pion and kaon production are key parameters to estimate ϕ_{SK}. The estimation is done using a beam Monte Carlo simulation called JNUBEAM that uses NA61/SHINE measurements for the pion production cross section [39].

The neutrino energy has to be inferred by the kinematics of the particles detected in the neutrino interaction. The neutrino energy in CCQE

interactions ($\nu_l + n \rightarrow l + p$) is calculated by the lepton momentum p_l and scattering angle θ_l with respect to the beam direction:

$$E_\nu^{rec} = \frac{(m_n - V)E_l + (m_p^2 - m_l^2)/2 - (m_n - V)^2/2}{(m_n - V) - E_l + p_l \cos\theta_l} \qquad (2.3)$$

where V is the average nuclear potential of oxygen [38].

At SK, events are identified by Čerenkov rings. More description about Čerenkov radiation will be given in Section 2.3.

In CCQE interactions, the proton is usually below Čerenkov threshold [40], and thus there is typically only one Čerenkov ring from the outgoing lepton. In other interactions, typically multiple rings are detected because they have more than one charged particle in the final state. Therefore, CCQE and non-CCQE interactions can be distinguished by counting the number of rings. However, π^+ from non-CCQE interactions and μ^+ produced from the π^+ can be below Čerenkov threshold. But, in this case, an electron is produced in the muon decay, so we can also use the electrons to distinguish CCQE and non-CCQE interactions.

The signal events for the ν_μ disappearance are clear single ring events, called μ - like events, in CCQE interactions. One of the main backgrounds is from charged-current single π production (CC1π^+). In the final state of CC1π^+ interactions, π and μ are produced. If the Čerenkov ring from the pion is not observed, or the Michel electron is not observed, then the CC1π^+ is mistaken as a single μ-like ring. Likewise, the signal events for the ν_e appearance are fuzzy single ring events, called e - like events, in CCQE interactions. One of backgrounds for ν_e appearance is the ν_e contamination in the neutrino beam from muon decays ($\pi^+ \rightarrow \mu^+\nu_\mu$ and $\mu^+ \rightarrow e^+\bar{\nu}_\mu\mu_e$) and $K^\pm/K^0$ decays. The fraction of ν_e contamination in the ν_μ beam is about 1%.

The other main background is NC single π^0 production (NC1π^0). When π^0 decays, two gamma rays are produced. The photons convert into e^+e^- pairs and produce e - like rings in the detector. If these two rings from the two photons overlap or one of two rings is missed, the event will look like an electron event.

2.1.1 Off-Axis Configuration

T2K is the first experiment that uses off-axis configuration. The off-axis angle is the angle between the neutrino beam and the detectors.

Figure 2.2 shows the neutrino energy flux for different angles and the corresponding probability[31]. For on-axis angle, the neutrino energy has a
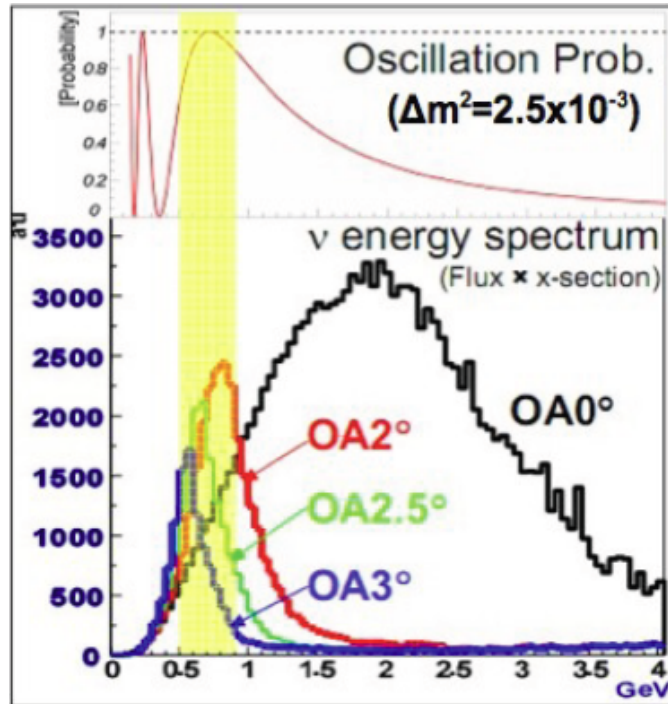
Figure 2.2: Neutrino flux for three different off-axis angles and corresponding oscillation probability.

peak at 2 GeV. Going further off-axis angle, the peak energy of the neutrinos becomes lower. At the 2.5 degrees off-axis, the peak of the flux is at $\sim$ 0.6 GeV, and here, the oscillation probability is maximized. In addition, the tail in neutrino energy distribution is shortened so that the number of high energy non-CCQE and NC interactions are reduced. Therefore, T2K sets the off-axis angle at 2.5 degrees.
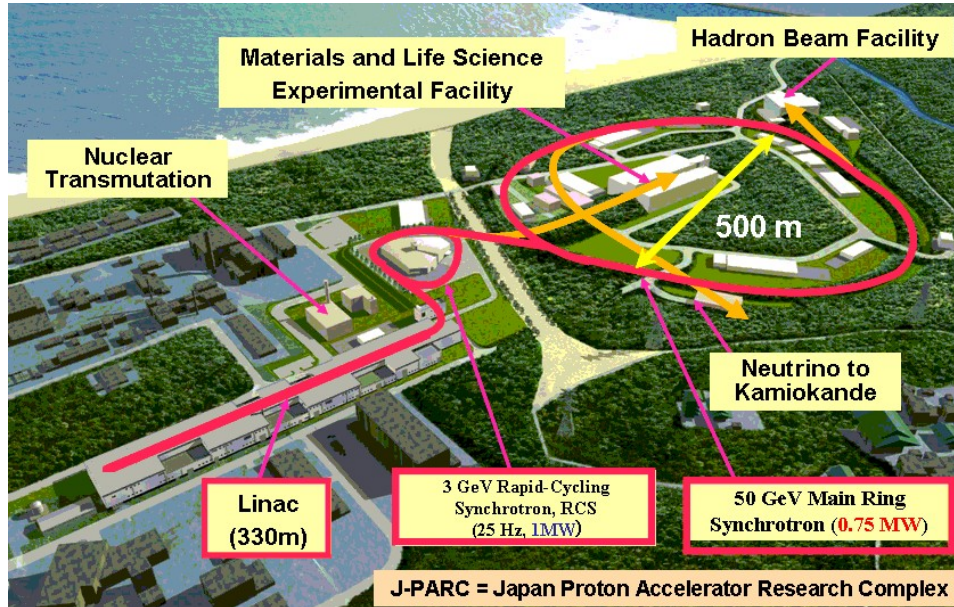
Figure 2.3: Map of J-PARC facilities.

2.2 Beamline

The T2K primary beamline transports protons extracted from the Main Ring (MR) at J-PARC, Japan. The proton beam is accelerated in three steps through a series of accelerators. First, it is the LINAC where the protons are accelerated to 181 MeV. Second, the boosted protons are fed to the 3 GeV synchrotron, called RCS. The beam increases in energy to 3 GeV. Finally, some of the 3 GeV proton beam enters the MR, and is accelerated up to 30 GeV [41]. The overall facility is shown in Figure 2.3.

The extracted beam from the MR is delivered to the target, where a large number of pions and some kaons are produced by interactions. The target itself is a thin carbon rod, ~ 90 cm long.

The phase 1 goal of T2K is to accumulate 8.33×10^{21} protons on target (POT), but as of December 2011 we have 1.43×10^{20} POT. Figure 2.4 shows the history of POT and the protons-per-pulse [42].

The secondary particles (predominantly pions) from proton interactions are focused by the magnet horns and passed to the decay pipe. More specifically, the pions are focused to the beam direction by the magnet horns.

The dominant processes in the decay volume are
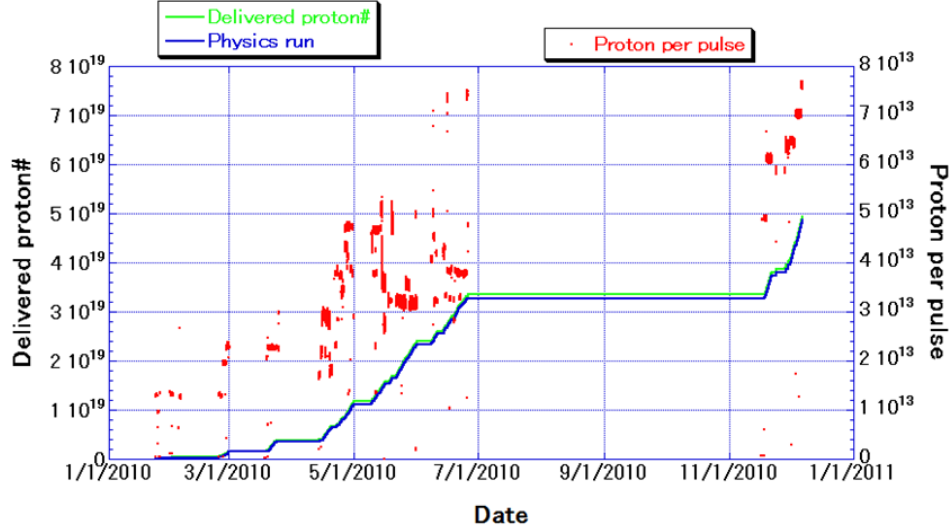
Figure 2.4: History of protons on target (POT). Solid line is the integrated number of delivered protons from the beginning of the experiment. The scale is in the left axis. Red dots are the number of protons per beam pulse, and the scale is in the right axis [42].

$$\pi^+ \to \mu^+ + \nu_\mu$$
$$K^+ \to \mu^+ + \nu_\mu$$
$$K^+ \to \mu^+ + \nu_\mu + \pi^0$$
$$K^+ \to e^+ + \nu_e + \pi^0$$
$$\mu^+ \to e^+ + \nu_e + \overline{\nu}_\mu$$

Figure 2.5 shows the neutrino energy flux at ND280 for different parent decay modes. The ν_μ is mostly from π^+ decays and most of the ν_e is from kaon and muon decays.

At the end of the decay pipe, the muon flux monitor (MUMON) sits to measure the properties of the muons penetrating the beam dump, including the profile center and intensity to ensure that the beam axis is correct [38].

Two kinds of near detectors are 280 m away as described in Section 2.4, one on the beam axis (on-axis) and one off-axis. The off-axis neutrino beam will be observed at the far detector. Figure 2.6 shows overall schematic [43].

23
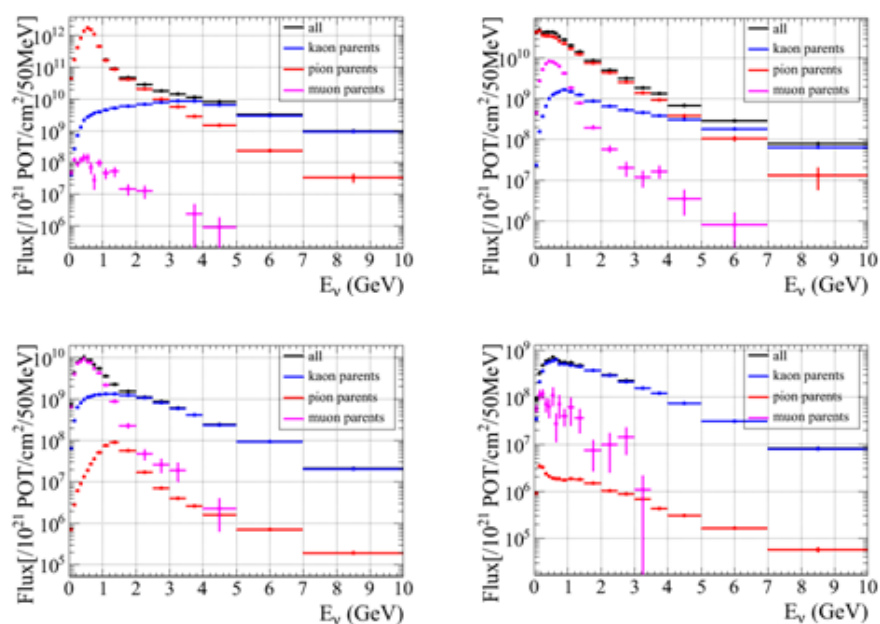
Figure 2.5: The neutrino fluxes at ND280 for different parent decay modes. The left column is of ν_μ (top) and ν_e (bottom). The right column is of $\overline{\nu}_\mu$ (top) and $\overline{\nu}_e$ (bottom). These figures are taken from http://www.t2k.org.
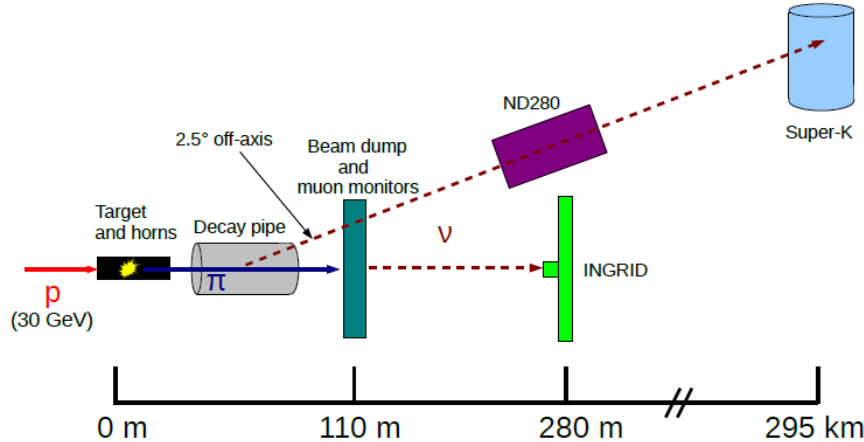
Figure 2.6: Simplified schematic of T2K beamline. Primary proton enters the target station and produce secondary pions and kaons. The particles decay into charged leptons and neutrinos in the decay pipe. The neutrinos are observed by ND280 and SK.

2.3   The Super-Kamiokande Detector

The Super-Kamiokande detector (SK) is the far detector for T2K. It is the world's largest contained water Čerenkov detector, located 1000 m under a mountain [44]. Figure 2.7 shows the outline of SK. It is 39.3 m in diameter and 41.4 m in height, filled with 50,000 tones of ultra-pure water. About 13,000 photomultipliers are installed on the detector walls. It is divided into two sections, the inner-detector (ID) and the outer-detector (OD). The ID is used to detect and reconstruct events, while the OD is a veto for background events such as cosmic muons or other interactions in the surrounding material [45].

Čerenkov radiation is electromagnetic radiation which is produced when charged particles, such as electrons, pass through a medium faster than the speed of light in that medium [46]. The radiation is detected by photomultiplier tubes (PMTs), which are very sensitive photosensors with high gain of 10^7 (at a supply voltage from 1700 to 2000 V), low noise rate of 3 kHz, and good time resolution of 2 ns [47]. These properties allow PMTs to detect a large fraction of single photon signals.

Figure 2.8 provides an illustration of Čerenkov radiation. The left shows
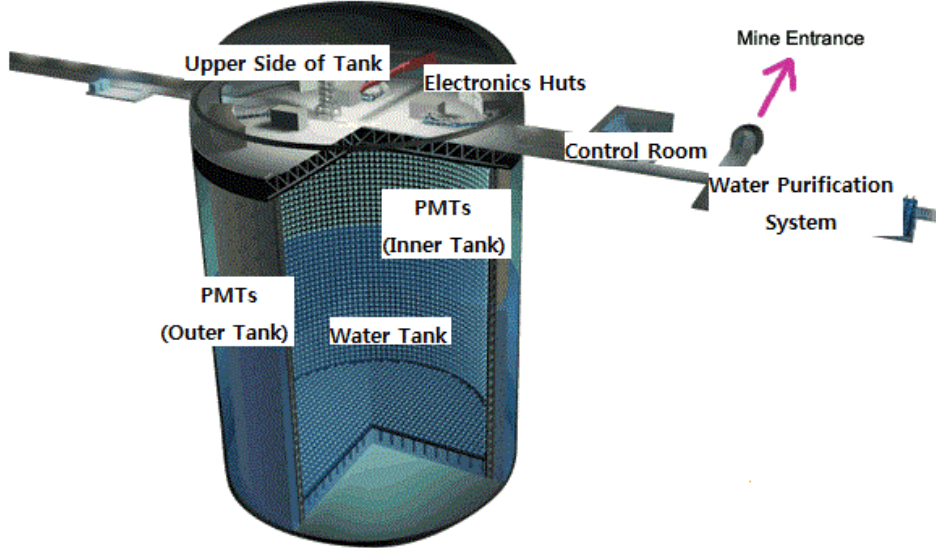
Figure 2.7: Outline of the Super-Kamiokande detectors. This figure is taken from http://www-sk.icrr.u-tokyo.ac.jp/sk/index-e.html .

a light cone of a neutrino-nucleus CCQE interaction, in which a muon is produced, emitting Čherenkov radiation. The recoil proton is below Čerenkov threshold, so it does not produce a ring. The right figure shows a lengthwise section of the cone. The emitted radiation from charged particles constructs a wavefront in the shape of a cone with an angle related to the speed of the particle in the medium [48]. Therefore, its cross section is a ring. The angle of the cone is expressed as

$$\cos\theta = \frac{c}{vn(\lambda)} = \frac{1}{\beta n(\lambda)} \tag{2.4}$$

where c is the speed of light, v is the speed of light in medium and n is the refractive index of medium. n depends on wavelength of light λ.

Muons and electrons are distinguished by looking at how well-defined the edge of the ring is. Particles with heavy mass will not radiate significantly in the water, so that they create a well-defined ring. In other words, massive particles such as muons make sharp rings. However, light particles such as electrons will lose energy radiatively and scatter, so that secondary particles are released. They make fuzzy rings. As a result, a ring from a muon has a
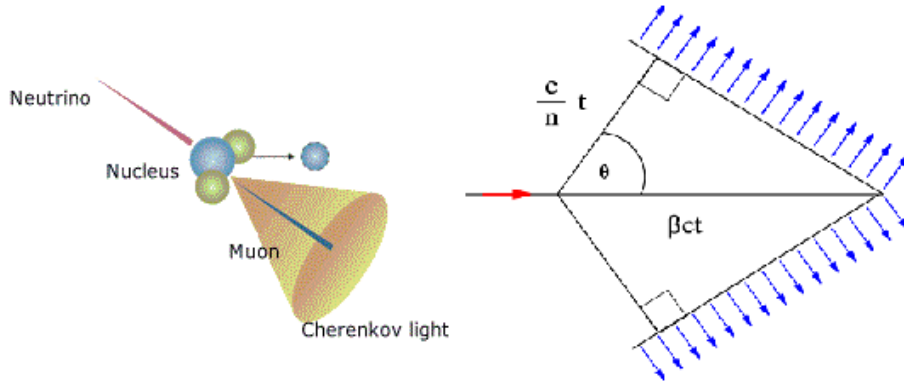
Figure 2.8: The left figure shows Čerenkov light in a cone shape. It is nucleus scattering, which is the relevant for ~ 1 GeV neutrinos. The right figure shows lengthwise section of a light cone. The angle θ is determined by speed, travel time, and refractive index of the medium. These figures are taken from http://en.wikipedia.org/wiki/.

much sharper edge than an electron ring. The top figure in Figure 2.9 is an example of a μ - like event. The bottom figure is an e - like event.

2.4 The Near Detectors

The near detector complex consists of two detectors. One is the on-axis detector, INGRID, measuring the neutrino beam profile. The other one is the off-axis detector, ND280, that measures the interaction rates, neutrino energy spectrum, and interaction kinematics of the off-axis neutrino beam directed towards SK. ND280 consists of several detectors enclosed within a dipole magnet, which provides a magnetic field. Figure 2.10 shows how both ND280 and INGRID are installed together within the near detector complex.
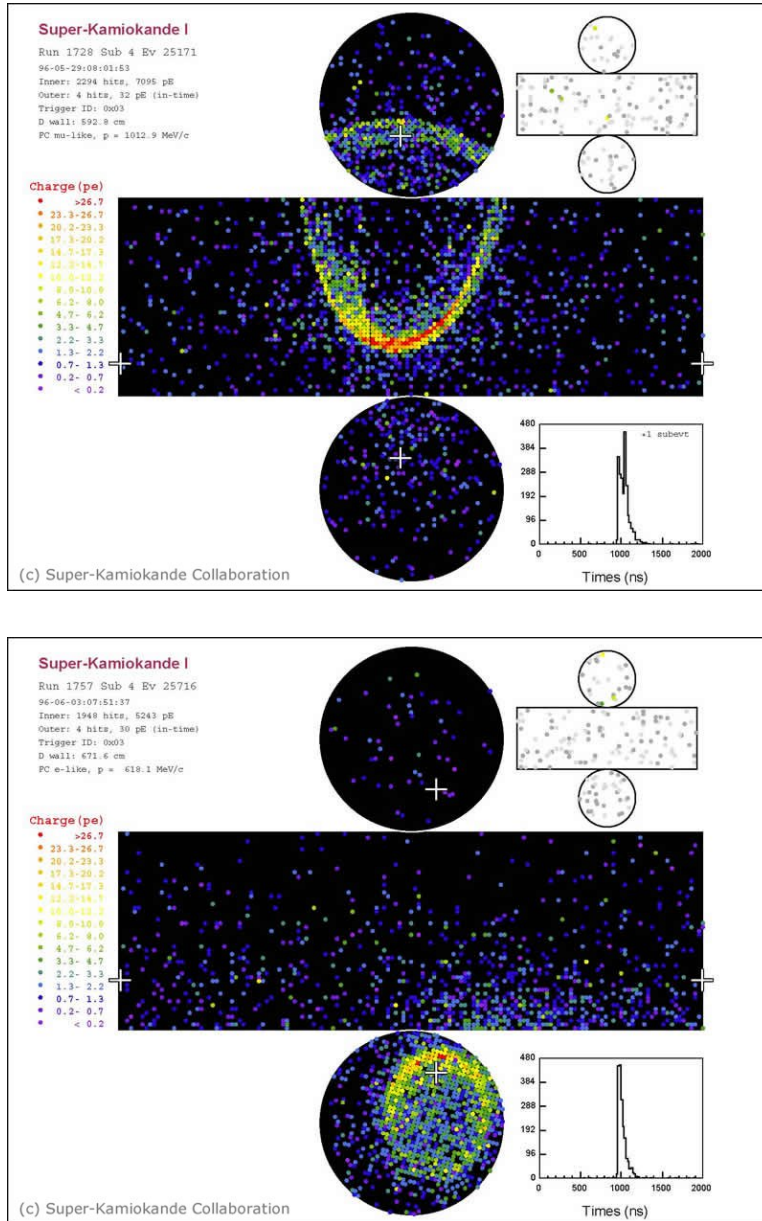
Figure 2.9: Example μ - like event at SK on the top and e - like event on the bottom. These figures are taken from http://www-sk.icrr.u-tokyo.ac.jp/sk/detector/display-e.html.
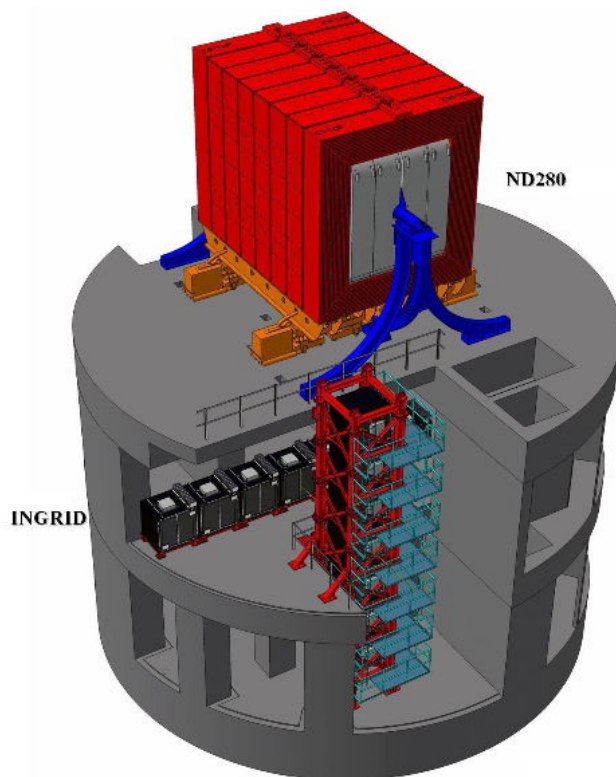
Figure 2.10:   The outline of installation of all near detectors, located 280 m away from the decay pipe. This figure is taken from http://www.t2k.org.

2.4.1   The INGRID Detector

INGRID, the Interactive Neutrino GRID, sits on-axis with respect to the beam line, 280 m from the beam target. The detector is designed to measure the on-axis neutrino flux and beam profile. The main purpose is to estimate systematic uncertainties related to the beam flux [49].

INGRID is a cross-shaped detector, made of 16 identical modules as shown in Figure 2.11. Each module is composed of alternating layers of iron and active scintillator. This is surrounded by veto scintillator planes to reject background events occurring outside the detector. Figure 2.12 shows a single INGRID module.
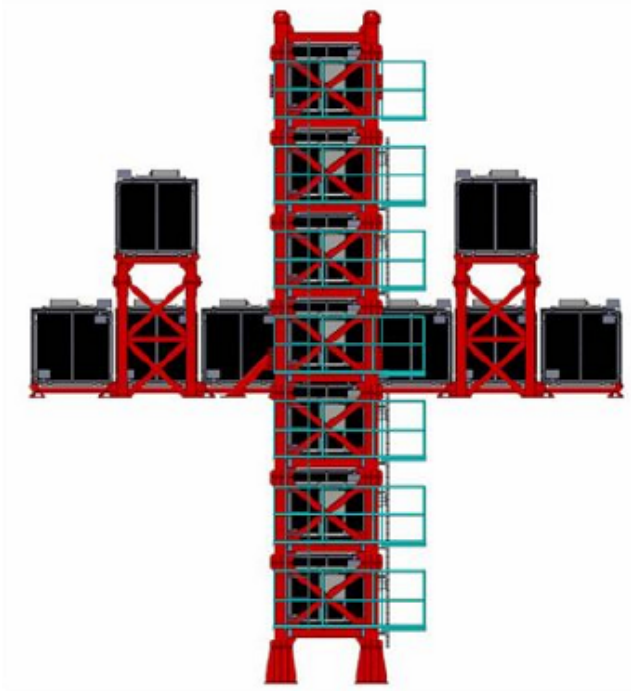
Figure 2.11: The overview of the INGRID detector. 14 identical modules are arranged as a cross and 2 additional separate modules located outside of the main cross. This figure is taken from http://www.t2k.org .

2.4.2 ND280

T2K uses an off-axis beam configuration so that the oscillation is maximum at the far detector around the T2K neutrino energy range. Since the neutrino flux seen by the far detector is off-axis, it is important to also have a near detector off-axis to understand the neutrino beam and interaction properties. The main goal of ND280 is understanding these properties.

The central tracking system of ND280 consists of three time projection chambers (TPCs) and two fine-grained detectors (FGDs). The π^0 detector (P0D) is used to understand π^0 production channels, which are key backgrounds to the ν_e appearance measurement. The electromagnetic calorimeter (ECal) and the side muon range detector (SMRD) surround both the tracker and the P0D. The ECal is designed to detect photons, and the SMRD measures the range of charged particles exiting the tracker.
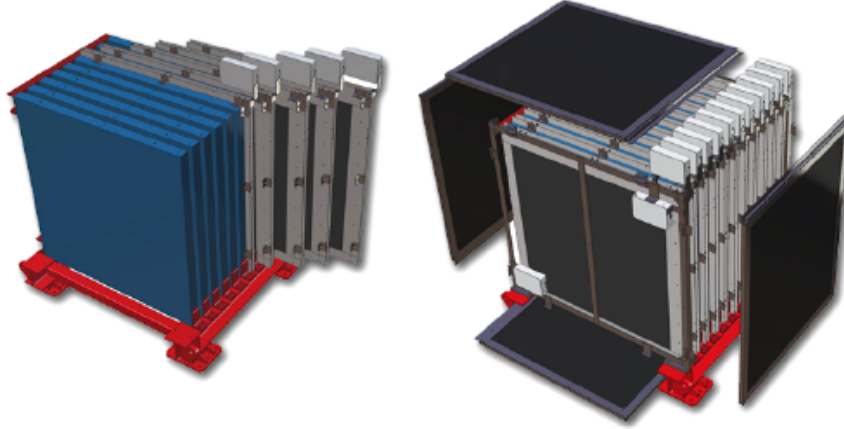
Figure 2.12: A single INGRID module. The module consists of a sandwich structure of nine iron plates and 11 tracking scintillator planes surrounded by veto scintillator planes. This figure is taken from http://www.t2k.org .

All of the tracker, P0D, ECal, and the SMRD are surrounded by the magnet. The magnet provides a horizontal uniform 0.2T magnetic field perpendicular to the beam direction. Because of the magnetic field, particles have curved trajectories in the detectors, so that the momentum and sign can be measured by the curvature of the particles. Figure 2.13 shows the overall configuration of ND280.

Time Projection Chamber

A Time Projection Chamber (TPC) is a gas-filled detector. Figure 2.14 shows a single TPC. Along its width, a TPC is divided by a central high-voltage cathode plane, which makes a uniform electric field between the cathode and the end planes. When particles pass through the TPC volume, they produce ionization in the gas. The electrons from the ionization drift to the end plates, where the MicroMegas (MM) modules lie. Each end plate has 12 MicroMegas modules and each module contains 1728 pads [51].

The MM detect free electrons ionized in the gas that drift to the anode. Because high momentum leptons from CCQE interactions are mostly forward-going, they will be curved in the y direction in the applied magnetic filed. In the yz plane, the trajectory of the particle is determined directly by the MicroMegas detectors, depending on which pad observes charge. x-
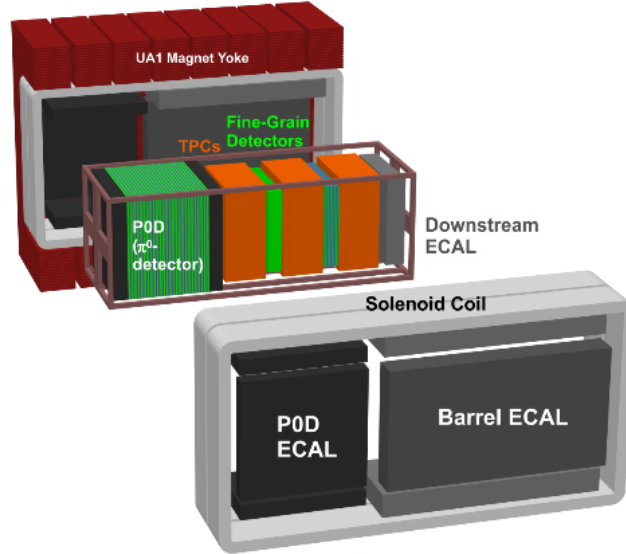
Figure 2.13: All elements in ND280. P0D, FGDs, TPCs, and DsEcal are held inside a stainless steel frame, called the basket. BrEcal and P0DEcal are attached directly to the magnet. The magnet encloses all of the detectors. This figure is taken from http://www.t2k.org .

position information is recovered by looking at the time taken for the drift electrons to reach the MicroMegas modules. A time is needed to set the absolute drift time, so a good initial time coming from the scintillator detectors like the FGDs is required.

A TPC is filled with a gas mixture of Ar, CF_4, and C_4H_{10}. The ratio of gases is chosen to maximize the drift velocity of electrons. The drift velocity in the gas mixture is ~ 77 mm/μs and the maximum drift distance from central cathode to MicroMegas is 897 mm [50]. This reduces the time to readout the detector. The TPC is a slow detector in the sense that it must wait for all the ionization to drift to the readout planes. The faster this happens, the faster the detector can start taking data again [52]. Since the density of this mixture is low, relatively few interactions are expected in the TPCs. Rather, most neutrino interactions occur in the FGDs, which have a large target mass.

T2K uses three identical TPCs for tracking. The primary purpose of the TPCs is to measure muon momenta in CCQE interactions and to identify particles using the measured energy loss in the gas, dE/dx [53].
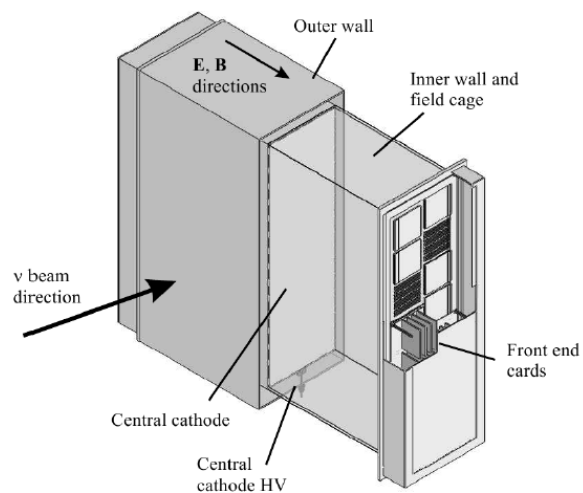
Figure 2.14: An TPC is a double-box. The inner box is actually filled with gas mixture. Electronics are attached to the front of the inner box [50].

The most upstream TPC (TPC1) is located between the P0D and the upstream FGD (FGD1). The second TPC (TPC2) is between the two FGDs. This measures forward going particles from FGD1 and backward-going particles from the downstream FGD (FGD2). The last TPC, placed after FGD2, measures the momentum of particles produced in FGD2 and going forward.
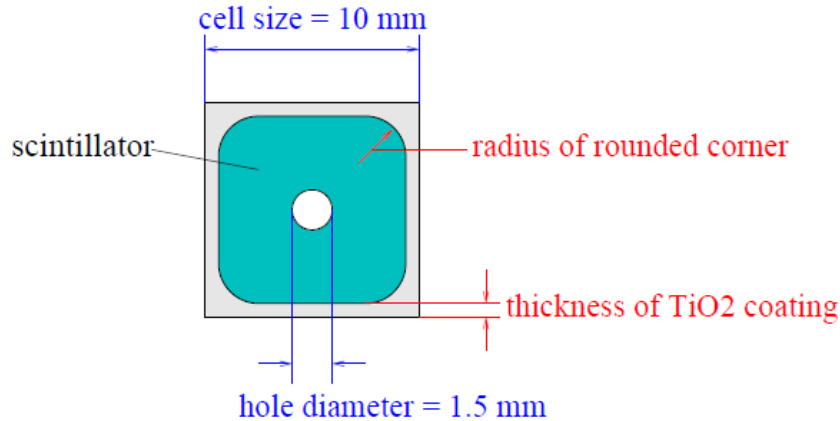
Figure 2.15: A single scintillator bar for FGDs. The scintillator part has rounded corners and is coated by TiO$_2$. At the center, there is a hole for a WLS fiber [54].

Fine-Grained Detector

The Fine-Grained Detectors are the other part of the tracker system of ND280. They are placed between the three TPCs. The two FGDs have the same size, but different internal structure. In each FGD, scintillator bars are arranged in layers along the x or y axis alternatively, perpendicular to the beam direction. This structure gives 3D tracking by alternating measurements of x and y as the track travels in the z-direction. Figure 2.16 shows a part of an FGD and how all components are installed.

Figure 2.15 shows an FGD scintillator bar. Each bar is coated with TiO$_2$ to reduce optical cross-talk which would make noise in other channels [54]. A wavelength shifting (WLS) fiber passes through the center of each bar. One end of the fiber is mirrored and the other end is coupled to a Multi-Pixel Photon Counter (MPPC). When a charged particle hits a bar, the attached MPPC measures the emitted light.

FGD1 has 30 layers of scintillator bars. FGD2 has fewer layers and instead has water layers between the scintillator layers. This allows the determination of neutrino cross sections on water by comparing the rates in the two detectors.

The FGDs provide target mass for neutrino interactions in the tracker,
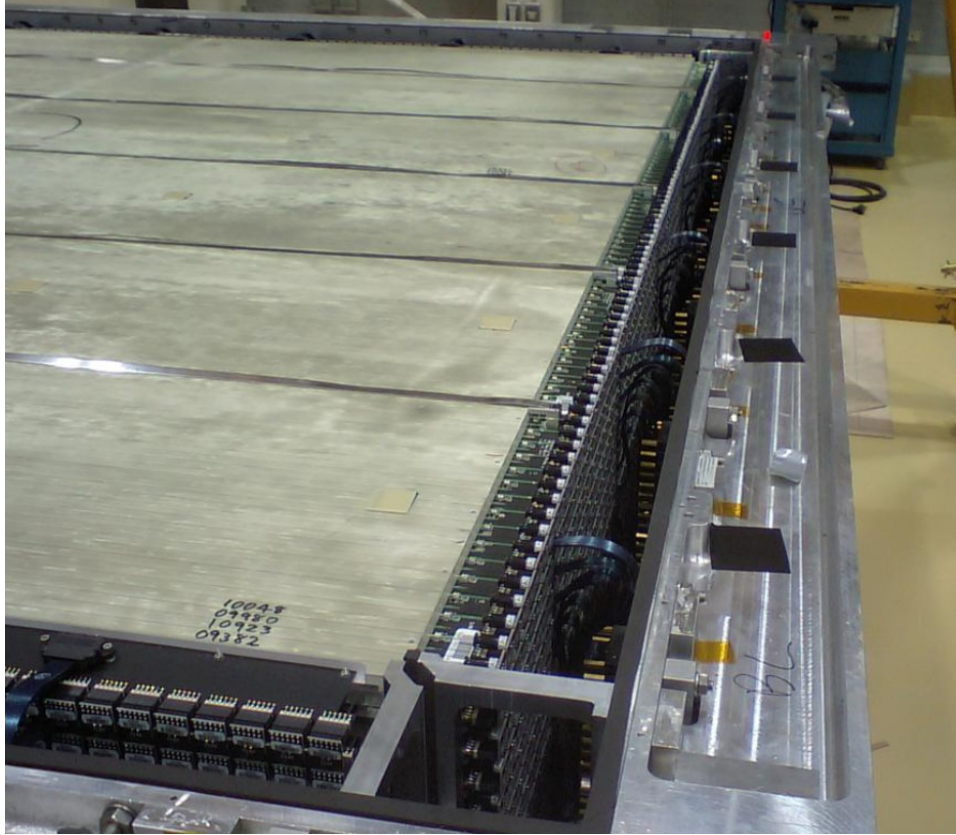
Figure 2.16: A photo of an FGD showing layered structure of scintillators and the MPPCs with the WLS fibers. This is installed vertically so that the plane faces the neutrino beam. This photo is taken from http://www.t2k.org.

but also play the role of tracking particles emerging from the interaction vertex. The tracking system measures the ν_e and ν_μ rate and the neutrino energy spectrum through CC interactions and provides the unoscillated muon and electron neutrino event rates and energy spectrum for the oscillation analysis. There will be more detail about the FGDs later.

π^0 Detector

The pi-zero detector (P0D) is used to understand π^0 production, which is one of the dominant backgrounds for the ν_e appearance analysis. The π^0 detector measures π^0 cross section on water for processes such as,

35
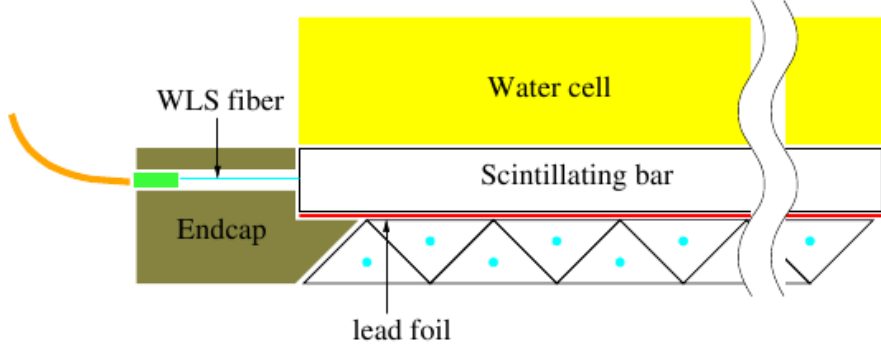
Figure 2.17: The scintillator bars for P0D are triangular to improve position detection. The water cell is removable. This figure is taken from http://www.t2k.org .

$$\nu_\mu + n \to \mu^- + p + \pi^0 \tag{2.5}$$

$$\nu_\mu + p \to \nu_\mu + \Delta^+$$
$$\Delta^+ \to p + \pi^0 \tag{2.6}$$

where n denotes a neutron and p denotes a proton. This allows us to understand one of the important backgrounds, $NC1\pi^0$ interactions, and predict the expected number of π^0 events at SK [55].

The P0D consists of active scintillator layers, brass and lead layers to induce photon conversions, and target water layers. The water layers are removable, so that data can be taken with water in and with water out. Active layers are built of triangular scintillator bars with a fiber coupled to an MPPC. Figure 2.17 shows the P0D bars. Because of the triangular bars, particle positions can be reconstructed with good resolution if more than two layers of bars are hit. The two types of inactive layers are targets and radiators. Targets are water cells providing oxygen target mass.

Radiator layers are made of two different materials, lead and brass. These are using to contain decay photons from π^0. Since the radiation length of lead is shorter than brass, lead will absorb more of the particles from the photon shower, reducing the information available for reconstruction. Because of this reason, lead radiator layers are used as a radiator on the outer layers of the P0D. Otherwise, in the inner layer, brass is used as radiator rather than lead so that it can give better energy resolution [56].

Electromagnetic Calorimeter

The ECals are installed to detect photons. While the TPCs already measure the particle momenta, the ECals cover a larger area and detect neutral particles which are invisible in the TPCs.

The ECals consist of three sections: The Barrel ECal (BrEcal) surrounding the tracker, the P0D ECal surrounding the P0D and the Downstream ECal which is placed downstream of TPC3. Each ECal is a combination of lead and scintillator. Each scintillator layer is orientated perpendicular to its neighboring layer. The BrEcal consists of modules on each side, top, and bottom of the tracker. Each BrEcal module has 31 layers of scintillator bars. The dimensions of the top and bottom modules are $150 \times 50 \times 420$ cm^3. The side modules have different dimensions, $50 \times 230 \times 420$ cm^3. The P0D ECal consists of 6 layers of scintillator bars and has similar dimensions to the BrEcal. The top and bottom modules of the P0D Ecal have dimensions, $140 \times 50 \times 230$ cm^3. The side module dimensions are $50 \times 230 \times 260$ cm^3. The DsEcal has 34 scintillator layers and dimensions of $200 \times 200 \times 50$ cm^3 [55]. The lead layers are ~ 4 mm in thinckness.
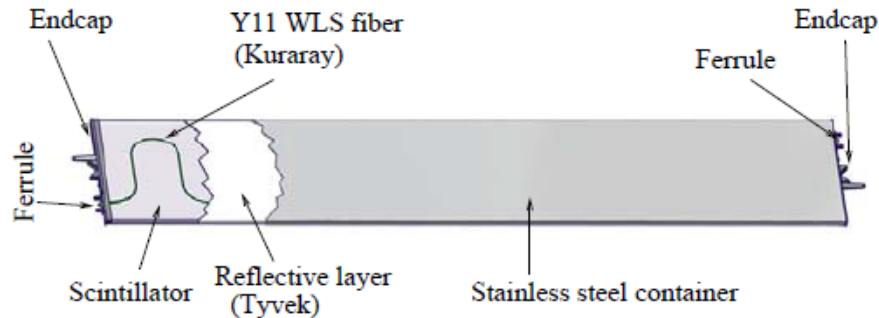
Figure 2.18: Sliced view of a SMRD slab. This figure is taken from http://www.t2k.org .

Side Muon Range Detector

The Side Muon Range Detector (SMRD) allows us to detect particles that exit the central tracker region. For example, a muon emitted at large angles with respect to the beam direction might not pass through the TPCs or just leave a short track in the TPCs. The SMRD is designed to detect these muons with high efficiency.

The SMRD consists of scintillator slabs. An individual SMRD slab is similar to an FGD scintillator bar, but is wider and is coupled to the fiber in a different way. The slab is embedded with s-bent wavelength shifting fibers. Figure 2.18 shows a sliced view of a SMRD slab. The s-bent fiber collects light evenly over the broad surface.

Whereas the other detectors are placed in the inner volume enclosed by the magnet, the Side Muon Range Detector is installed between the steel yokes of the magnet. Therefore the size of the SMRD is determined by the magnet structure.The magnet yoke is split into C-shaped segments on either side of the detector. A single C-like segment consists of 18 iron layers made from 50 mm steel. Each layer is separated by an air gap of 17 mm thick and its dimensions are 90×70 cm^2 [57]. The SMRD modules are held in this air gap [58].

This sub-detector has two purposes. The first is to measure the muon momentum leaving the inner detectors. The muon momentum is measured by how far the muon penetrates into the iron of the magnet. By seeing how many layers of the SMRD are hit, the range can be measured.

2.5 FGD Detail

The FGDs serve as target mass for the tracking system and provides tracking of particles emanating from neutrino interactions in the FGDs. These FGD tracks are combined with the TPCs to provide complete tracking information for the interaction. Target materials are mainly carbon and hydrogen from scintillator bars, small amounts of TiO$_2$ from scintillator coating, and water. The FGD2 contains scintillator bars and water modules, while FGD1 is made of only scintillator bars. By comparing interaction rates in the two FGDs, the cross section of neutrino interactions on water can be estimated. Since the far detector is a water Čerenkov detector, it is important to measure cross section on water target.

In addition, determining the type of interactions occurring inside the volume is crucial. Hence, the FGDs must also have good tracking performance of particle detection. The most useful interactions for measuring neutrino oscillations are CCQE, so this means that it is important to distinguish CCQE and non-CCQE interactions. If non-CCQE interactions are mistaken for CCQE interactions, it leads to a wrong estimation of the neutrino energy spectrum since the important assumption is the mass of the recoiling hadron in reconstructing the energy. Most non-CCQE interactions are associated with pions produced with a muon and nucleon. Therefore,

we should detect pions and reconstruct proton trajectories as accurately as possible.

Though the inner structure of the two FGDs are a little bit different, basically they have same geometry and electronics architecture. Each FGD measures $280 \times 240 \times 36.5$ cm^3. Its depth along the beam direction is relatively thin so that most of charged lepton produced inside FGDs can penetrate into the TPCs, which can then provide a measurement of the particle momentum. Each scintillator module hangs inside a light-tight box made of aluminum.

When charged particles pass through the scintillator bars, they produce light. The MPPC converts the light into an electrical signal. Since the FGD electronics are designed to provide both timing and charge measurements, they rely on digitizing the photosensor waveform to extract time and charge.

Every single scintillator bar has a MPPC, and this MPPC is attached to a photosensor daughter board. FGD1 contains 5760 MPPCs and associated daughter boards, and FGD2 contains 2688 MPPCs and boards. 16 of the boards and photosensors are together on a photosensor bus board.

No one can access the electronics boards during data running, so it is important to build a robust slow control system which is able to monitor and control the condition of the boards.

Furthermore, the temperature must be carefully controlled in order to ensure proper operation of the photosensors. The bias voltage of each photosensor must also be set individually in order to obtain an uniform detector response. Thus, a slow control system must be built to monitor the electronics and photosensor as well as to control the photosensor bias voltage.

2.5.1 Water Module

The water modules in FGD2 are a series of layers of water in polycarbonate vessels. The ends of each vessel are sealed by epoxy.

Since the detectors have lots of water-sensitive electronics, it is important to make sure the water never leaks out. A negative pressure system using a vacuum pump provides water leak protection in the case of minor leaks in the module. The water pressure is kept below atmospheric pressure by the system.

2.5.2 Scintillator Module

The scintillator produces the light that is detected by the MPPC. The scintillation light is produced when the charged particles ionize the molecules

in the material.

The basic building block of a scintillator module is a scintillator layer. The layer consists of 192 scintillator bars alternating between x and y in the xy plane. One X layer and one Y layer are glued together and form a single XY module. The dimensions of each module are $186.4 \times 186.4 \times 2.2025$ cm^3. A scintillator bar contains a fiber in its central hole. The fiber is not glued to the bar, but coupled to the bar through the air gap. One end of a fiber is mirrored to reflect light back along the fiber and improve light collection efficiency. The other end is coupled to a Multi-Pixel Photon Counter to measure light and its timing.

The FGD1 has 15 XY modules, 30 layers in total. The FGD2 has 7 XY modules, alternating with water modules.

Single Cladding WLS fiber

Cladding (PMMA)   Core (PS)

Cladding Thickness : T = 3% of D
Numerical Aperture : NA = 0.55
Trapping Efficiency : E = 3.1%

Double Cladding WLS fiber

Outer Cladding (FP)   Inner Cladding (PMMA)
Core (PS)
Ti
To

Cladding Thickness : T = 3%(To)+3%(Ti) = 6% of D
Numerical Aperture : NA = 0.72
Trapping Efficiency : E = 5.4%
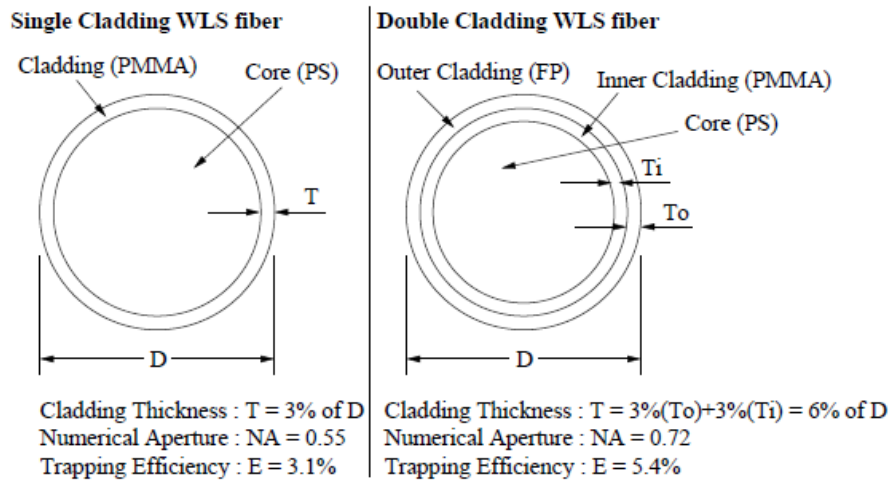
Figure 2.19: Wave-length shifting fiber comparing single cladding and double cladding fibers [54].

Wavelength Shifting Fiber

Light from scintillator bars travels through a fiber inside the bar. This fiber is a double-clad wavelength shifting fiber(WLS). Figure 2.19 is the cross section of the fiber. Double cladding improves capture and transmission of light in the fiber.

The produced light in the scintillator is in the UV range, $100 \sim 400$ nm, while the MPPC is sensitive at the range of green light, ~ 500 nm. For this

reason, we use WLS fibers. Its peak absorption wavelength is $\sim$ 430 nm, and subsequent emission spectrum is peaked at 476nm. Figure 2.21 shows the detection efficiency of the MPPC as a function of wavelength.
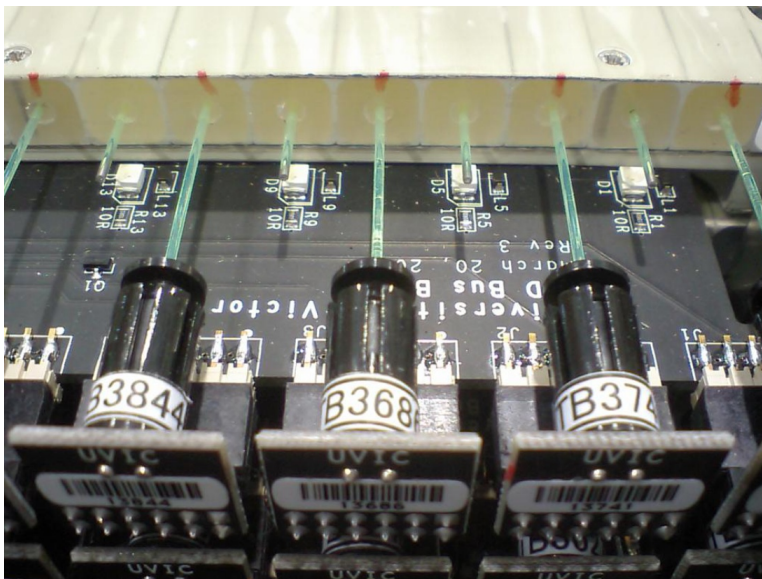
Figure 2.20: A photo of the MPPCs with the WLS fibers. This photo is taken from http://www.t2k.org.

Multi-Pixel Photon Counter

For choosing proper photosensors for the FGDs, a number of requirements were considered. The sensors should be compact and robust. They should also have high gain with low voltage and high detection efficiency. Moreover, since the photosensors will be used inside a magnet, they must be insensitive to magnetic field. The MPPCs satisfy these features, so T2K selected them.

The MPPC is a pixellated avalanche photodiode that operates in Geiger mode with 1.3 mm^2 sensitive area, so it has single photon sensitivity. An avalanche photodiode (APD) is a semiconductor electronic device which converts light to electricity. It can amplify the resulting photocurrent when a reverse voltage is applied. If the APD is operated in a reverse voltage above its breakdown voltage, a very high gain($\sim 10^5$) is obtained. This is called "Geiger mode". Figure 2.20 shows the MPPC with the WLS fibers.

Each pixel of the MPPC works independently in Geiger mode, and all the pixels are connected in parallel. Since a single incident photon will fire

41
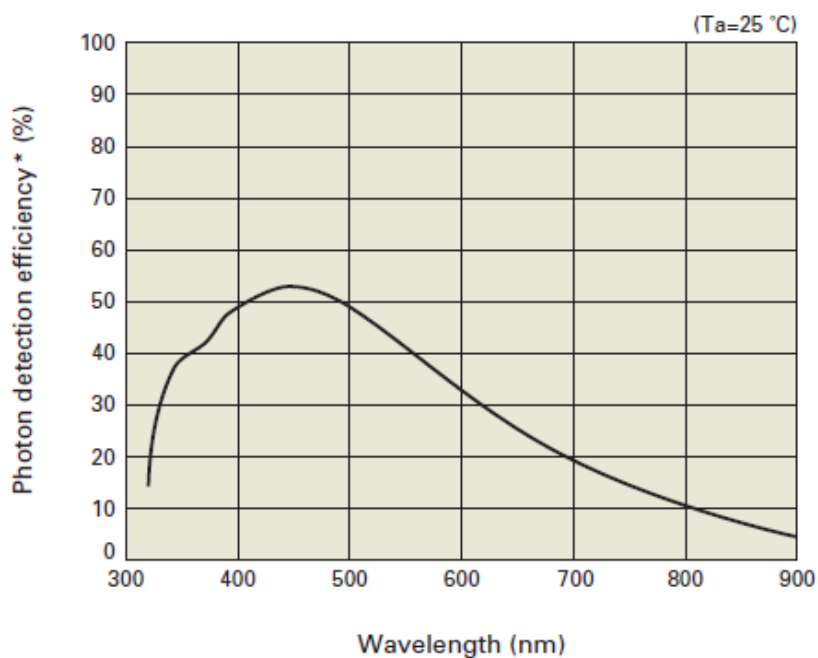
Figure 2.21: The MPPC sensitivity as a function of wavelength. The figure is taken from http://www.hamamatsu.com/.
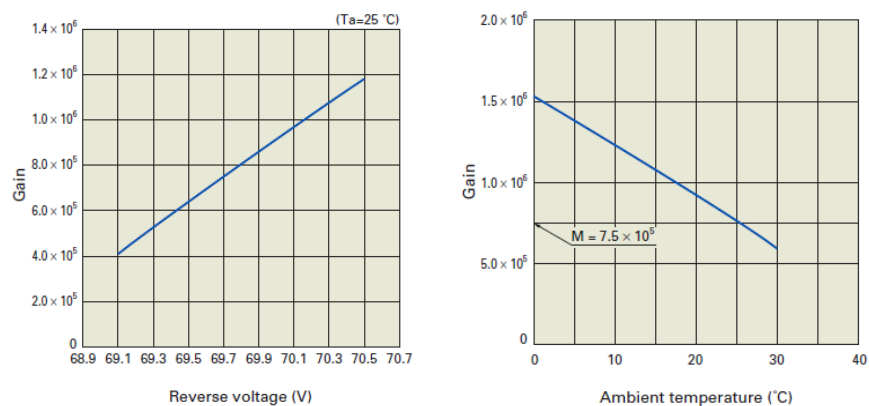
Figure 2.22: The MPPC gain as a function of the reverse voltage (left) and temperature (right). The figures are taken from http://www.hamamatsu.com/.

a single pixel, the number of fired pixels are proportional to the number of incident photons. This device counts the number of photons. But when the number of incident photons is more than the number of pixels in an MPPC, the device is saturated. In other words, the number of fired pixels are not proportional to the number of the photons any more. So the device becomes non-linear at higher light levels.

The gain depends on the operating voltage and the ambient temperature. Figure 2.22 shows the relations. In the left plot, the gain linearly changes with varying reverse voltage. In the right plot, the gain decreases with increasing temperature at fixed reverse voltage. It is important to measure the temperature and operation voltage during data-taking to calibrate the MPPCs.

The MPPC measurement has three main sources of uncertainties; cross-talk, dark noise, and after-pulsing. Cross-talk is when 1 pixel fires an adjacent pixel in the same MPPC resulting in more than one pixel fired by a single photon. Dark noise is from avalanches induced by thermal excitation without an optical signal. Lastly, after-pulsing is caused by a second avalanche from the same photon.

2.5.3 Electronics

As mentioned earlier, each FGD is covered by a dark box. The front-end electronic system, back planes, and the mini-crates are attached around the outside of the dark box. The back-end electronics, which monitor and control the overall system of the FGDs and give connection between the FGDs and the database, are located outside of the magnet.

The photosensors are very sensitive to temperature. However, the necessary electronic components continuously emit significant heat. It is thus important to locate the readout electronics outside of the dark box. Moreover, cooling water circulates around the dark box to cool the electronics.

Only the scintillator bars, fibers, photosensors, and the passive electronic components are housed within the dark box, thus providing thermal isolation. Figure 2.23 shows the overall installation of the electronics.

Photosensor Connection

Two types of boards are used to provide electrical connectivity to the photosensors; the photosensor daughter boards (PDB) and the photosensor bus boards (PBB).
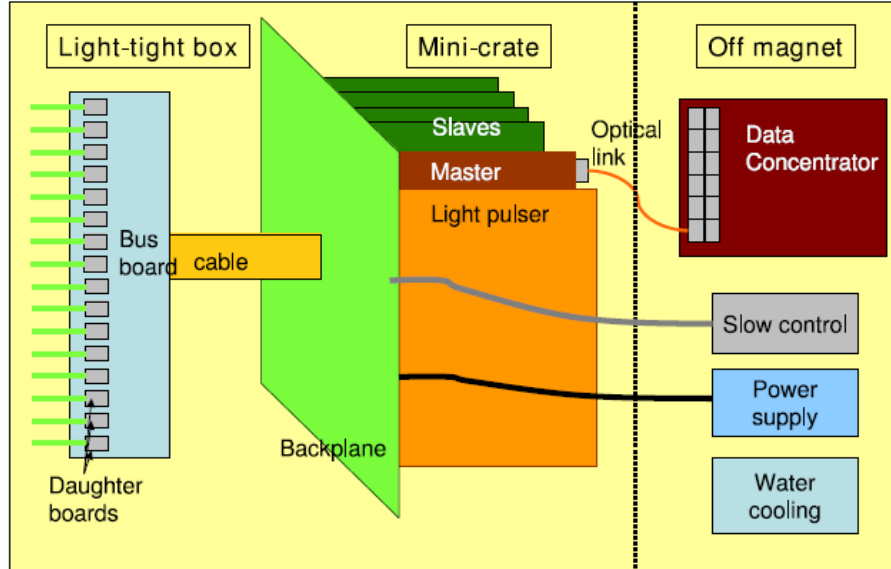
Figure 2.23: FGD Electronics. Only photosensor daughter boards and bus boards are in the dark box. Mini-crates including Light Pulsar Boards, Crate Master Boards, and Front End Boards are outside of the dark box. All of them connects to Data Concentrator Cards and the slow control system [54].

The PDBs connect individually to the MPPCs and 16 of these are collected on a PBB. The PBBs provide electrical connection between PDB and monitoring/controlling systems. Each PBB has two temperature sensors, and they are monitored by the slow control system. It also has 16 LEDs to flash the fiber to calibrate the measurements.

The PBBs are connected to the Front-End Board(FEB) located outside the dark box with cables.

Front End Electronics

There are two main purposes of the Front-End Electronics. First, they amplify and digitize the signals from the photosensors. Second, they also control the photosensor bias voltages and monitor currents and temperatures.

Each scintillator bar has a photosensor and a LED. The LED is used to calibrate the waveform measured at a photosensor. So the FGD electronics is designed to read out and collect data from photosensors and to control

measuring components like the LEDs.

There are three types of boards for different uses. A Front-End Board (FEB) generates photosensor bias voltages and digitizes the analog waveforms coming from the sensors. A FEB handles 64 MPPC channels. FEBs must provide stable and flexible bias voltage for the photosensors, because the gain and noise rates of the sensors are highly sensitive to the applied voltage and vary from sensor-to-sensor.

A Crate Master Board (CMB) controls communication between the front-end and the back-end electronics. CMBs handle communication with the back-end electronics. The CMB receives clock and trigger signals from the Data Concentrator Card (DCC) and distributes them to the FEBs. The CMB also receives the data from the FEBs and compresses the data. Only important data such as carge and time of a large pulse are stored by the online pulse-finding algorithm. The compressed data are transfered to the DCC.

A Light Pulser Board (LPB) controls the duration and intensity of LED pulses and provides electrical pulses to flash the LEDs. The LPB controls the LEDs which are used for photosensor calibration and finding dead channels. If CMBs receive a light calibration trigger from DCCs, the LPBs flash the LEDs. The LEDs provide a method for identifying dead channels and calibration the MPPCs.

A mini-crate houses all of these boards: 15 PBBs(one per XY module), 1 CMB, 1 LPB, and 4 FEBs for FGD1. The mini-crates in FGD2 are the same, except that only 2 FEBs are required.

Back End Electronics

The back-end electronics are located outside of the magnet and are connected to the front-end electronics by a combination of electrical and optical cables. This system monitors the condition of inner electronics elements, control power and flow of data, and also packages the data for storage.

The Data Concentrator Cards (DCC) make the connection between the front-end electronics and the data acquisition (DAQ) server. The DAQ is responsible for collecting the data taken from the detector electronics. One DCC covers 4 mini-crates, so 12 DCCs are needed in total. While the data are compressed on CMBs, further compression is done on the DCCs.

The back-end electronics also include the slow control system, which interacts with detector components to set and monitor detector parameters. All of the boards in the mini-crates are connected to a slow control system link. The system controls power and bias voltages, and monitors tempera-

	FGD1	FGD2
XY modules	15	7
Layers	30	14
Channels	5760	2688
Photosensor Bus Board	360	168
Front End Boards	96	48
Crate Master Boards	24	24
Light Pulser Boards	24	24
Mini-Crates	24	24
Data Concentrator Cards	6	6

Table 2.1: List of electronics

ture and current. The slow control system also provides an alarm system when specified limits are exceeded and presents a unified interface to the users. A summary of the full electronics is shown in Table 2.1.

Chapter 3

ND280 Software

3.1 Overviews of ND280 Software

The ND280 Software is a set of software packages which are closely associated with each other. The packages handle all aspects of the offline handling of ND280 data, including data handling, calibration, reconstruction and analysis output, as well as the Monte Carlo simulation (MC) of the detector. It also contains classes, called oaEvent, to store the information from the various stages of processing.

The MC simulation consists of several parts. JNUBEAM simulates the neutrino beam. The beam flux determined by this stage. The neutrino interactions based on the simulated flux is then generated using the two external particle generators, NEUT [59] and GENIE [60] with the geometry from nd280mc, which is the ND280 simulation package. This provides the final state particles for each interaction. nd280mc handles the particle tracking and generation of hits through the detector geometry and material. nd280mc relies on the external particle generation and tracking framework Geant4 [61]. Based on the flux and the geometry, it simulates how outgoing particles from the interactions propagate through ND280 and what the energy deposits are. The generated events are propagated to the electronics simulation package, elecSim, to generate the simulated electric response, which then are passed through the rest of the ND280 Software chain in the same way as the real data. Further details will be described in Section 3.2.

Unlike the MC simulation, real data is output in a different format by the MIDAS-based data acquisition. Thus an additional step is needed to
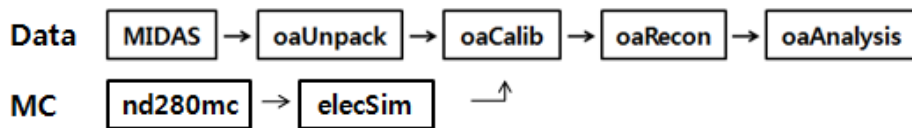

Figure 3.1: The ND280 Software

47

decode this data into the oaEvent format that can be processed by the ND280 software.

Figure 3.1 shows a simple schematic for the ND280 software process. For the data, the first step is to "unpack data". At this step, raw data are converted to oaEvent-based classes and which are stored in the ND280 ROOT files. oaEvent depends on the ROOT framework and defines the ROOT file structure for ND280 data. The second step is "oaCalib". At this step, calibration constants for each sub-detector are calculated and then applied to calibrate charge, time, and other observed variables. The next step is "oaRecon". Reconstruction is finding tracks, vertices, and clusters based on the measured hits. The package receives the calibrated hits and reconstructs the neutrino interactions over all detectors, from the P0D to the DsECal. Each detector has its own reconstruction package. Then the global reconstruction (oaRecon) combines the results from the individual reconstruction to form reconstructed objects that span all of ND280.

The last step is "oaAnalysis", which makes simple ROOT trees from which the user can perform analysis using ROOT macros.

Since this thesis focuses on the FGDs, we will have more description of the FGD software than other detectors. This will be described in Section 3.5.

3.2   Monte Carlo Simulation

Currently, we have two stages of detector simulation. One is nd280mc for detector simulation, and the other one is elecSim for electronics simulation.

Geant4 is used as the platform for nd280mc [61]. It provides a way to take into account complicated detector geometry. It also tracks the particles through geometry, accounting for things like energy loss and deposition in the materials, and hadronic interactions. It generates hits, which are energy depositions in the active elements of the detector. The hits are stored in a class called TG4Hits and are translated into the detector response via elecSim.

elecSim is the second stage of the detector simulation. It generates electronic responses for sub detectors by modeling detection components. The first step simulates the scintillator bars and the WLS fibers. These are simulated considering the average light yield of the scintillator and the attenuation length of light in the WLS fibers. For the scintillator, the output of this step is the predicted number of photons and their times at the MPPC. The next step is the MPPC response simulation. The simulation takes ac-

count of photon detection efficiency, cross-talk and dark noise. The MPPCs are treated as a grid of pixels, and each pixel releases a charge if a photon is incident on the pixel. The noise caused by cross-talk or after-pulsing effects are also simulated to make the simulation more realistic. The output is a list of charges and times of the simulated hits.

elecSim also simulates the TPC response. TPC elecSim calculates the number of ionization electrons created in the TPCs as a charged track traverses the gas volume. Then, it simulates electron drift and diffusion, which is how the electrons move towards the MicroMegas planes, and the electric responses in the MicroMegas planes.

3.3   oaEvent

The fundamental structure for ND280 data is provided by the package oaEvent. The package strongly depends on ROOT, which is a programming package offered by CERN for particle physicists. oaEvent defines the data format of ND280 output files based on ROOT, and handles writing, opening and reading of files. The ROOT files made by oaEvent record information in several classes that mirror the way in which the information is produced in order to facilitate access to the information that is stored. For example, the ROOT files save raw data, simulated data, and reconstructed data separated into different classes for which oaEvent provides methods to set, access and modify these data structures.

An individual measurement of charge and time is stored as a single hit, with hits from different sub-detectors stored separately in different lists.

oaEvent has three main data classes: MC truth classes, raw data classes, and reconstructed data classes.

MC truth classes store information such as the true primary vertices or true particle trajectories. In ND280 terminology, the term "trajectory"is used to distinguish the true path of the particle from its reconstructed counterpart, which is called a "track". Subclasses within the vertex and trajectory classes store pertinent information such as the position, momentum, charge and particle type.

The raw data classes are handled by two sub packages, oaRawEvent and oaUnpack. These packages decode the MIDAS banks, which contain the raw data, into the oaEvent format which is readable by the other ND280 software packages.

oaEvent also contains the reconstruction classes, which store reconstruction information. The classes are split into several categories: TReconBase,

49

TReconCluster, TReconShower, TReconTrack, TReconPID and TRecon-Vertex. TReconBase objects have lists of reconstructed hits called nodes. The nodes are points on the reconstructed tracks, while the hits in general have their own definition of position. TReconCluster, TReconShower, TReconTrack, TReconPID and TReconVertex are different types of reconstructed objects. All these classes are derived from the base class TReconBase. A TReconCluster object is a collection of hits in space that represents a blob of energy deposition. A TReconVertex object is also a collection of hits, but is different from a cluster in that hits in a vertex are at the same point in space. If a vertex is associated with a neutrino interaction, this is a primary vertex. If a particle coming from a primary vertex make an interaction such as decay, a vertex associated with the interaction is called a secondary vertex. A TReconTrack object is a collection of clusters or hits, which defines a path of particles. It contains information such as position, direction, charge and curvature. If a track is identified with a particle type, it becomes a TReconPID. A TReconShower object is a path with a null curvature. It might represent electromagnetic shower, for example.

3.4 Example Event Displays

In the following, event displays for various different event types are shown. Figure 3.2 shows a sand muon event passing through all sub detectors from P0D to the DsECal. Sand muons are muons entering the detector that are produced by neutrino interactions in the sand surrounding the detector hall. In the figure, the left-most region in brown represents P0D, after that 3 TPCs and 2 FGDs. The right-most box is the DsECal. One can see that each sub-detector contains a single track corresponding to the muon, and that the tracks recorded in each detector match to form a single track across all the detectors.

Figure 3.3 depicts a cosmic event coming from the upper left in the P0D. It also shows one clear reconstructed global track.

Figure 3.4 and Figure 3.5 show neutrino interactions occurring in the P0D and FGD1 respectively. Interaction in FGD1 can be separated from interactions in the upstream P0D by rejecting events with any tracks in the P0D or TPC1.
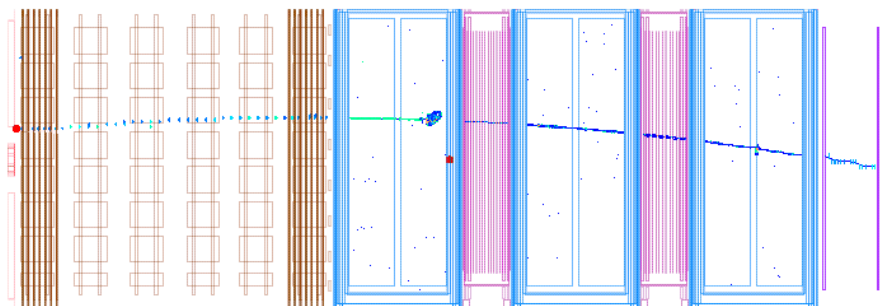
Figure 3.2: Sand muons going through all subdetectors.
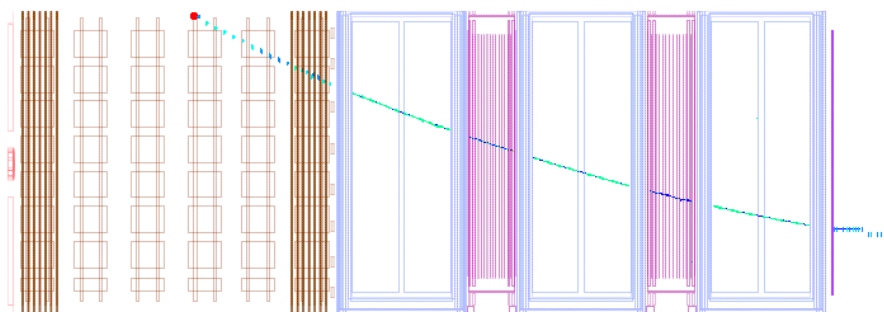
Figure 3.3: Cosmic track reconstructed across all detectors

3.5   FGD Software Packages

The FGD data analysis is separated into two stages. The first stage uses raw MIDAS data as input files. The raw data contains waveforms resulting from digitizing the activity in the MPPCs as recorded in a switched capacitor array (SCA). Figure 3.6 shows an example waveform [62].

A set of routines performs pulse-finding and fitting on the waveforms. For each pulse, a raw pulse height is measured from a digitized MPPC waveform, that is related to the energy deposit on the scintillators. After that, charge and time are extracted based on the pulse heights and positions in the wave form. These tasks are performed in fgdRawData, which is responsible for decoding the raw data, finding pulses in waveforms, fitting the pulses, and extracting charge/time from the pulses. The information is then available for further analysis.

51
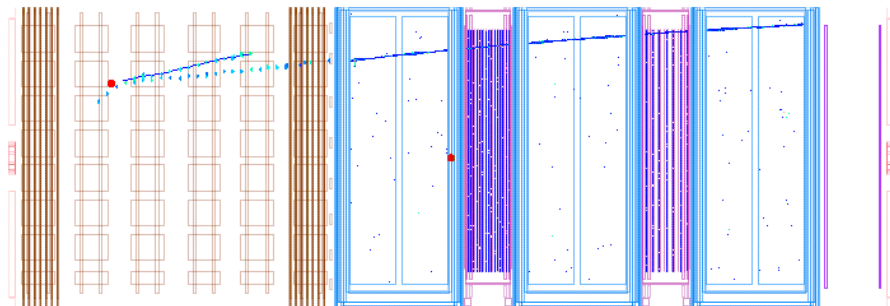
Figure 3.4:   Neutrino event in P0D sending single negative track into TPC1/FGD1/TPC2.

Event number : 24083 | Partition : 63 | Run number : 4200 | Spill : 0 | SubRun number :6 | Time : Sun 2010-03-21 22:33:25 JST |Trigger: Beam Spill
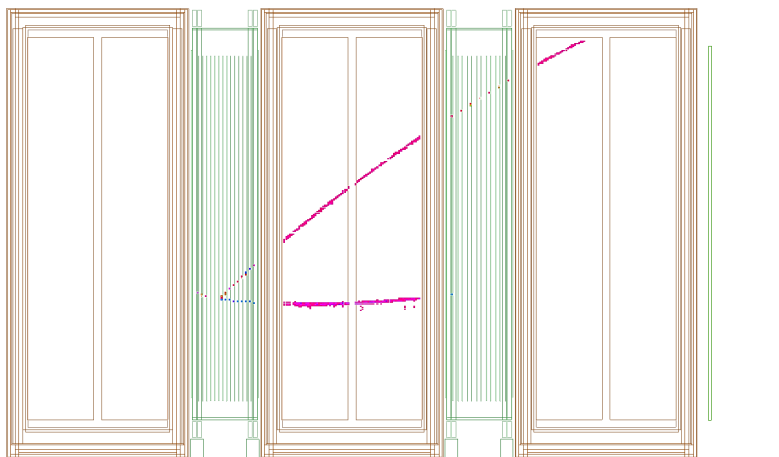

Figure 3.5:   Clean CC interaction in FGD1

The pulse heights are normalized in units of the average pulse height from a single MPPC avalanche, which depends on the operation voltage and temperature of the MPPC. The voltage and temperature can vary during data-taking. We measured how the height changes by varying the MPPC voltage at a fixed temperature. During data-taking, the temperature is measured by the sensors located on the PDB. The measured temperature is used to calibrate the MPPC, because the gain of the MPPC depends on a
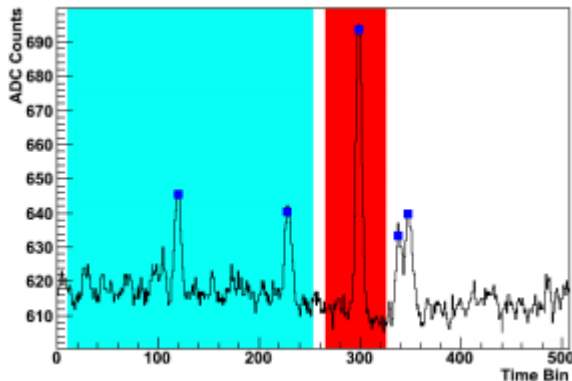
Figure 3.6: An example waveform of an FGD MPPC. The red region is used to measure the pixel fires from optical sources and the blue is used to measure background from dark noise [62].

temperature.

The times extracted from the fitted pulse are corrected for the skew in various clock domains and the different cable lengths. The time and charge information is converted into the oaEvent/THit class and stored in a ROOT file.

3.5.1 FGD Time Binning

A FGD time bin is a cluster of hits from tracks which are passing through the detector at the same time. The time binning algorithm sorts the hits in time and compares the times between the two neighboring hits, starting from the first hit. A pre-fixed parameter used by the algorithm is the maximum time gap, which is 100 ns by default. If the time difference is less than 100 ns, the two hits are put together in a bin. If the time difference is larger than 100 ns, the later hit is put into the next bin. This algorithm is shown in Figure 3.7.

The main purpose of the time binning is tagging Michel electrons and to separate neutrino interactions in different bunches. When a muon stops in the detector, it decays to an electron and neutrinos:

$$\mu^- \rightarrow e^- + \overline{\nu}_e + \nu_\mu \tag{3.1}$$

$$\mu^+ \rightarrow e^+ + \nu_e + \overline{\nu}_\mu \tag{3.2}$$
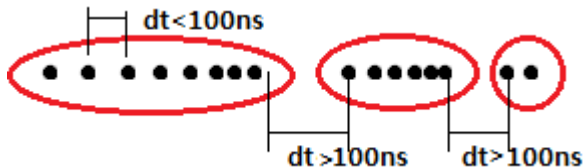
Figure 3.7: Time binning schematic. Time runs along the horizontal axis. Black points represent times of individual hits and red circles encompass hits which are placed into the same time bin.

The decay electrons are called Michel electrons. Since the muon lifetime (~ 2.2 μs) is much longer than the fixed time gap, the Michel electrons form isolated time bins. This is used for CCQE selection.

In Chapter 4, the Michel electron detection efficiency using cosmic data is discussed. We will see how often the Michel electron is found by the FGD time binning method.

3.5.2 FGD Reconstruction

Particles traversing through the FGDs with some energy and direction are represented as a set of hits which record point-like information along its path based on the position of the bars which are hit. In the data, we cannot know any true information of particles. Instead, we have methods to reconstruct the path, energy, or direction based on the hit information. The reconstruction algorithm finds 2D tracks in the xz or yz planes first by matching reconstructed hits, then 3D tracks are found by matching the 2D tracks.

The FGD reconstruction has two goals; finding hits in the FGDs which match to tracks reconstructed in the TPCs such as muon tracks, and finding short isolated tracks that start and stop in FGDs such as proton tracks.

Since the FGD reconstruction strongly depends on the TPC reconstruction, they share a unified algorithm. Before doing the FGD reconstruction, the TPC reconstruction must be done first. Once TPC tracks are reconstructed, the tracks are extended into FGDs and matched hits identified using the Kalman filter.

Hits which were not used in the FGD-TPC matching process are saved and reconstructed separately. This algorithm identifies short tracks which start and stop in an FGD and therefore are not matched to TPC tracks. A standalone hit clustering algorithm, called a Cellular Automaton, is used

for isolated reconstruction. The method creates segments, which are sets of hits in adjacent layers. If the segments in different layers form a quasi-straight line, they are connected together. The sets of connected segments form tracks [63].

FGD reconstruction has several types of objects. Cluster is a collection of hits in space, represents a blob of energy. Vertex is also a collection of hits, but a difference to Cluster is that hits in a vertex are at the same point in space. If all particles are emerging from a vertex, it could be a primary vertex. If at least one particle enters a vertex and some particles are emerging from it, it could be a secondary vertex. Track is a collection of clusters or hits, which defines a path of particles. It contains information of position, direction, charge, and curvature. Shower is a path with null curvature. It might represent electromagnetic shower for example.

The FGD tracks are split into a few categories. fittedFgdTpcTracks are TPC-FGD matched tracks. xyFgdTracks, yzFgdTracks, and fitted-FgdTracks are the tracks from the FGD isolated reconstruction in 2D and 3D respectively. These kinds of tracks are fully contained in an FGD.

Chapter 4

Cosmic Muon Studies

4.1 Introduction

4.1.1 Michel Electron Tagging

The neutrino interactions via CC channels can be identified by the primary charged lepton in the final state, since NC interactions have a primary neutrino instead of a charged lepton. In CC interactions, we are primarily interested in CCQE interactions because the neutrino energy reconstruction is possible by two-body kinematics. So it is important to distinguish CCQE and non-CCQE interactions. Michel electron tagging is a powerful method for this purpose.

For ν_μ CC interactions, both CCQE and non-CCQE have muons in the final state. We call these primary μ. The primary μ usually have high enough momentum to exit the FGDs. However, CC1π^+, which are the majority of non-CCQE interactions, have additional π^+ produced via the Δ resonance. They share energy with the nucleon produced in the decay of the Δ. Thus the pion typically has less momentum than the muons from CCQE. The pions with low momentum often stop in an FGD and decay to muons. We call these muons secondary μ. The secondary μ also stop shortly, usually in the same FGD where the pions stop, and decay to Michel electrons. For this reason, the Michel electron tagging can be used to discard non-CCQE interactions.

The Michel electron tagging is made by the identification of a delayed time bin following the first time bin associated to the stopping muon itself. But the problem is that other particles can also make delayed time bins as well. Therefore, other criteria are required to distinguish Michel electrons and non-Michel electrons bins. Figure 4.1 shows the total deposited charge distribution in all delayed time bins for different interaction channels in simulated neutrino interactions. Most CCQE (red) interactions have lower charge deposit, while CC resonant pion (light green) and CC DIS (blue) interactions have a noticeable bump with higher charge deposit. It is clear from the plot that eliminating events with delayed time bins having charge

56
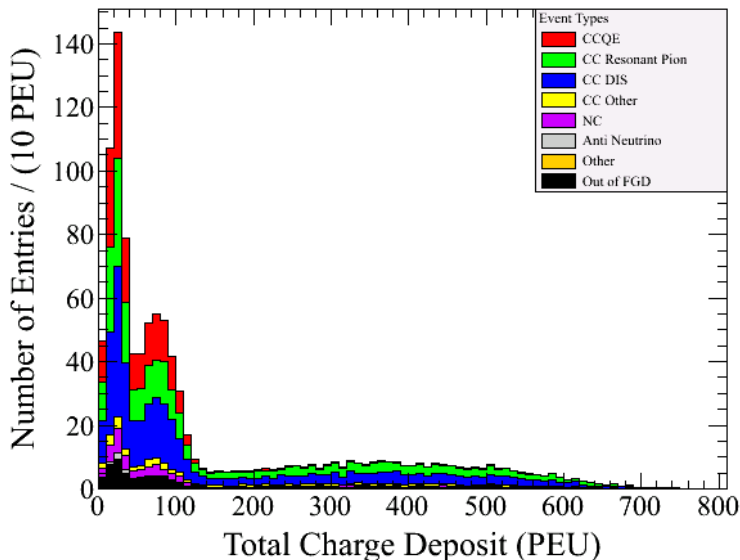
Figure 4.1: Charge distribution of all delayed time bins for different interaction channels.

deposit higher than 200 PEU (pixel equivalent units, i.e. the number of fired pixels of the MPPCs) will reduce CC1π^+ without removing CCQE.

In conclusion, an event is vetoed as a non-CCQE event if it has more than one delayed time bin and the bin with the highest charge has greater than 200 PEU.

However, we may fail to identify a Michel electron, even if there is a Michel electron decay. This is what we are interested in this thesis will be studied using cosmic data. We will look at the Michel electron detection efficiency. The efficiency is defined as

$$\text{Efficiency} = \frac{\text{Number of stopping } \mu \text{ with an identified Michel electron}}{\text{Number of all stopping } \mu}$$

(4.1)

4.1.2 Cosmic Rays

Cosmic rays consist of energetic particles produced in outer space. The composition of cosmic rays depends on which part of the energy spectrum is observed. But, generally, almost 90% of the incoming cosmic rays to the

Earth are protons. When the protons enter the Earth, they interact with molecules in the atmosphere and produce lighter particles, typically mesons such as pions and kaons. The resulting pions decay to muons in flight. So cosmic rays produce many muons and can provide a large sample of stopping muons in the FGDs. It allows us to understand how often a Michel electron is found by the FGD time binning method when a cosmic muon stops in FGD1.

4.2 Data Set Description

For the analysis, we use cosmic events recorded by the detector at Tokai in 2010. During the data taking, cosmic events are triggered by the external Cosmic Trigger Modules (CTM). ND280 have two CTMs. The FGD cosmic trigger is one of them. We have two FGDs and each FGD has 24 trigger primitives to the FGD CTM. It is organized as a 6×6 matrix as shown in Figure 4.2 [64]. The trigger in its current configuration requires a coincidence between hits in the two FGDs. The CTM generates a trigger that provides cosmic rays that pass deposit energy in both FGDs [65].

The Monte Carlo simulation of cosmic rays is done by the external simulation package called Corsika. Corsika is a computer software package for the simulation of air showers induced by the incoming cosmic rays [66].

The total numbers of events are 82,042 of the MC simulation and 7,697,733 of the data. Note that the MC simulation has much smaller statistics than the data.

4.3 Direction Convention

In ND280, the beam direction is along $+z$ axis. Tracks traveling along the beam direction are called forward-going tracks, while tracks in the opposite direction are called backward-going tracks. The scintillator layers in FGD1 are numbered starting from the left with respect to the beam direction. So the left end (upstream) layer is first and the right end (downstream) layer is last.

In a ND280 event display (See Figure 4.3), the beam direction ($+z$) is from left to right. The left-most box is TPC1, the next box is FGD1 and the right-most box is TPC3.
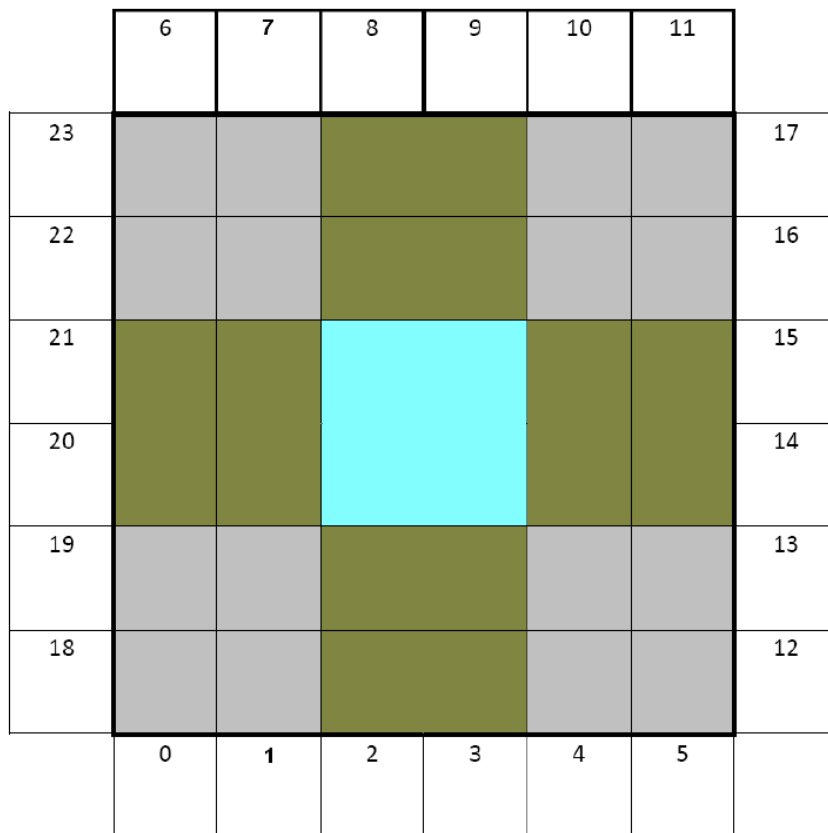
Figure 10: FGD tower segmentation

Figure 4.2:   The projective tower structure of the FGD cosmic trigger primitives [64].

4.4   Example Cosmic Event

While most cosmic rays pass through the whole tracker, some muons stop in one of the FGDs and produce secondary particles such as Michel electrons. Some muons with more vertical trajectories enter the tracker at a large angle and clip the corner of an FGD without stopping.

Figure 4.3 shows a through-going event. It spans TPC2, TPC3 and all the FGDs to the P0D. Another through-going event is in Figure 4.4, but with a large angle. Because the ray enters the detector quite vertically, it clips the corners of FGD1 and FGD2.
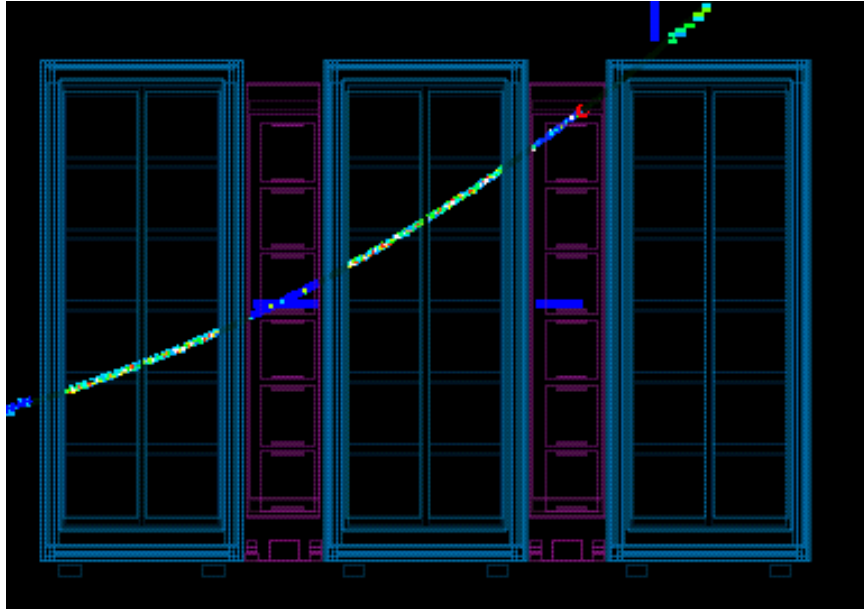
Figure 4.3: A going-through cosmic ray.
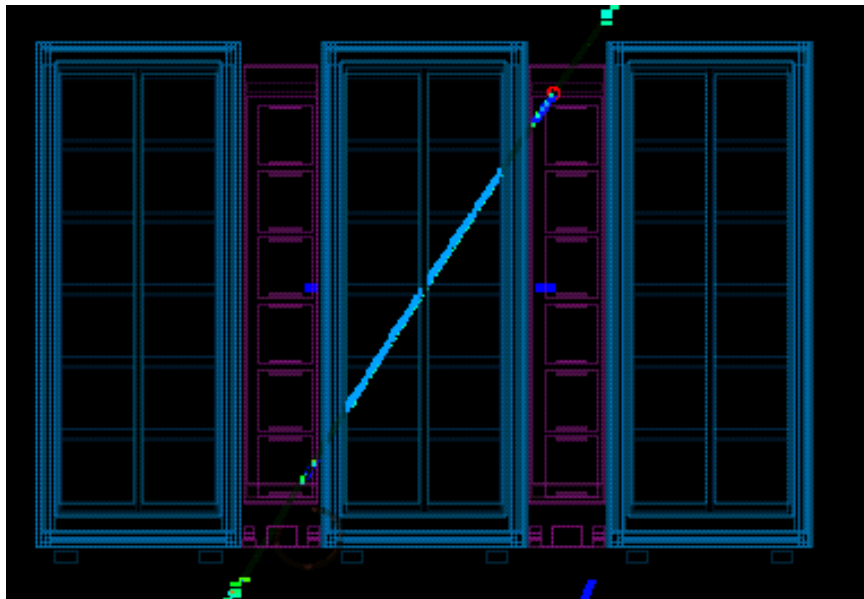
Figure 4.4: A going-through cosmic ray with a large angle.
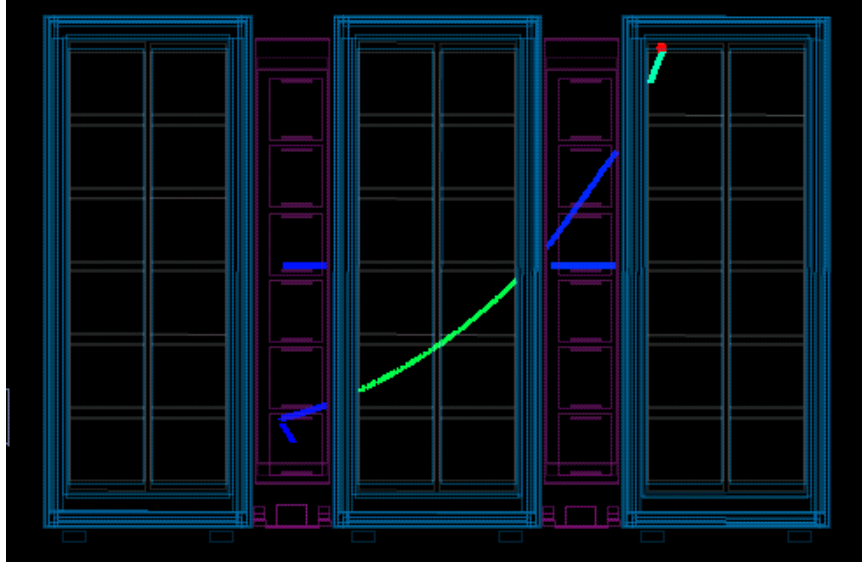
Figure 4.5: A stopping cosmic ray in FGD1. Then it produces a secondary particle in FGD1.

A stopping track is shown in Figure 4.5. The muon stops in FGD1 and produces a secondary particle, a Michel electron. The secondary track is the small blue one at the end of the primary track in FGD1. This kind of event is the type we are interested in. In the following section, we will describe how to select the stopping events.

4.5 Event Selection

4.5.1 Select a Clean Sample of Stopping Muons

Select stopping particles

Since cosmic rays contain not only muons but also other particles such as electrons, it is important to select a clean sample of stopping muons. This is the control sample to test the Michel electron detection. The sample is defined through two steps, stopping particles selection and non-muon elimination.

The first step is to select tracks stopping in FGD1. Basically, this is done by considering the position of the stopping point. Using time bins, the stopping point is determined by the upstream-most hit with respect to the
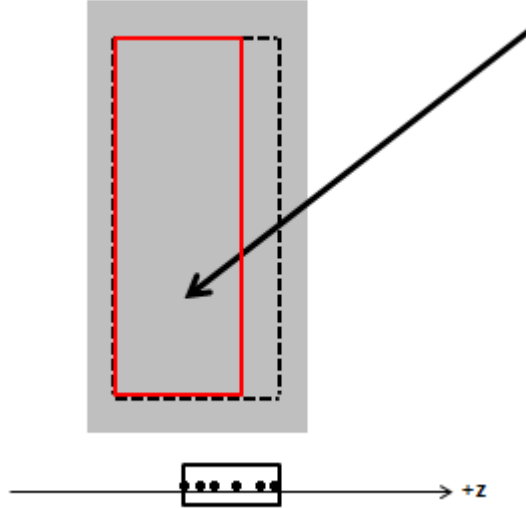
Figure 4.6: FGD1 on the yz plane. The gray box is the actual FGD1 detector of active layers not including the dark box. The dotted black box is fiducial volume. The solid box, the smallest one, is the defined box with the reduced downstream z position compared to the fiducial volume. The upstream-most hit of the first time bin with the minimum z position must be in the solid box. The boundary in the xz plane is also made in the same manner.

beam direction of the first time bin. The first bin is associated to the track of a cosmic particle entering the detector. The outermost hits are the hits having the minimum z or the maximum z in a bin. That is, each bin has two outermost hits; one with the minimum z and the other with the maximum z. Because the cosmic events are required to go through both FGDs by the FGD cosmic trigger, the tracks that stop in FGD1 are necessarily going in $-z$ with respect to the beam direction. So we use the outermost hit having the minimum z in the first bin to designate the stopping point of the cosmic tracks.

Figure 4.6 shows the detailed geometry of how tracks which do not stop in FGD1 are vetoed. The dotted box is the FGD1 fiducial volume. The fiducial volume is the effective detection area. It is smaller than the true FGD1 volume. Table 4.1 summarizes the position of the fiducial volume

and the true edge of FGD1. The solid red box in Figure 4.6 is the allowed region. If the upstream-most hit is in the defined box, it is considered a stopping track. Figure 4.7 shows the minimum z distribution of the first time bins in FGD1 fiducial volume. The MC (blue triangles) has relatively more tracks stopping in the last several layers. This is believed to be due to a mis-modeling of the FGD trigger in the MC simulation. It is not expected that this discrepancy will affect the analysis results. So the downstream z should be further upstream than the fiducial volume to make sure the MC simulation and the data are consistent. This discrepancy is currently not understood and will be investigated in the future.

In addition, there is a strange peak at the 7th layer (~ 190 mm) in the data. This results from a noisy channel in the layer. Some events have only one or two hits in FGD1 and one of the hits is produced the noisy layer. These events are not from actual cosmic events and are not simulated in the MC simulation. The discrepancy will be removed after the event selection cuts.

The x or y boundaries are also required based on the plane of the outermost hit. If the hit is in a xz plane, the y cut does not matter. Otherwise, if the hit is in a yz plane, the x cut does not matter. The cuts remove clipping tracks as shown in the left figure of Figure 4.8. Even if the minimum z position of the track is within the allowed region, the track does not satisfy the cuts on x or y.

	FGD1 edge (mm)	FGD1 fiducial volume (mm)	allowed region (mm)
minX	-932.17	-874.51	-874.51
maxX	932.17	874.51	874.51
minY	-877.17	-819.51	-819.51
maxY	987.17	929.51	929.51
minZ	115.95	136.875	136.875
maxZ	447.05	446.955	350.00

Table 4.1: FGD1 true edge, the fiducial volume cuts and the position of the red box in Figure 4.6.

Sometimes, a forward-going track stops in FGD1 and does not have hits on the first several layers, as shown in the right figure of Figure 4.8. In this case, the track is misidentified as a backward-going stopping track. So we also require there is a track in TPC2 (between FGD1 and FGD2) but not
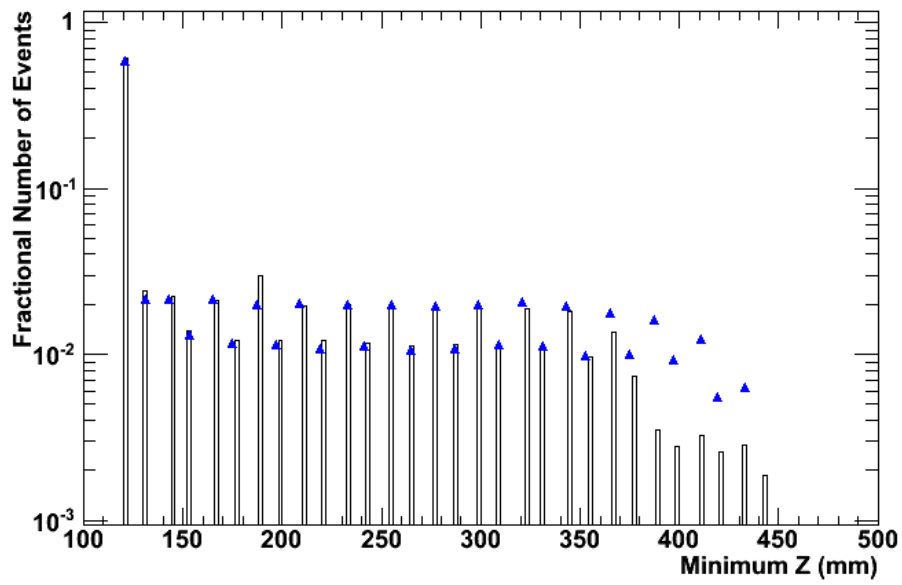
Figure 4.7: The distribution of the minimum z position of the first time bin in FGD1 fiducial volume of the data (black circles) and the MC simulation (blue triangles). Each bin corresponds to each layer. On the last layer, there are events in the MC simulation, but it is too small to appear in the plot.
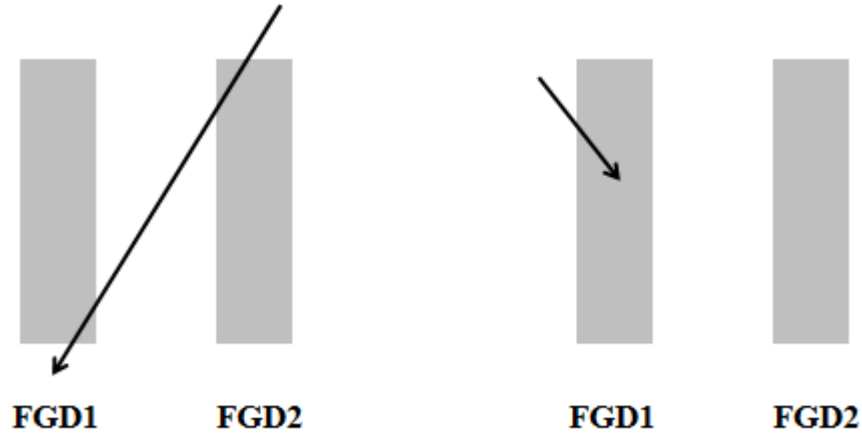
Figure 4.8: The left is a track that clipped the corner of FGD1. It forms a time bin that looks like a stopping track in FGD1. The right is a forward-going and stopping track. This stops in FGD1, but we do not need this kind of event.

in TPC1.

Figure 4.9 shows the charge distribution of the first delayed time bin for all stopping tracks having more than one delayed time bin. There is a discrepancy near zero charge between the MC simulation and the data, indicating that there are more stopping tracks with low charge in the first delayed bin. The very low charge indicates that the delayed bin has only few hits, which may be a form of noise such as after-pulsing of the MPPCs or a broken piece of the first time bin that are not simulated in the MC simulation. The data also has large tail with high charge deposit which are not shown in the MC simulation either. The discrepancy is removed after adding other cuts on the TPC2 track. TPC2 track should have enough number of hits to maker sure the track is fully contained in TPC2 and low enough momentum to make sure the tracks are allowed to stop in FGD1.

- Number of hits > 60

- Momentum < 300 MeV/c

Since there are 72 columns in the MicroMegas, we expect a track passing through TPC2 from beginning to end to typically have $\sim$ 72 hits. The
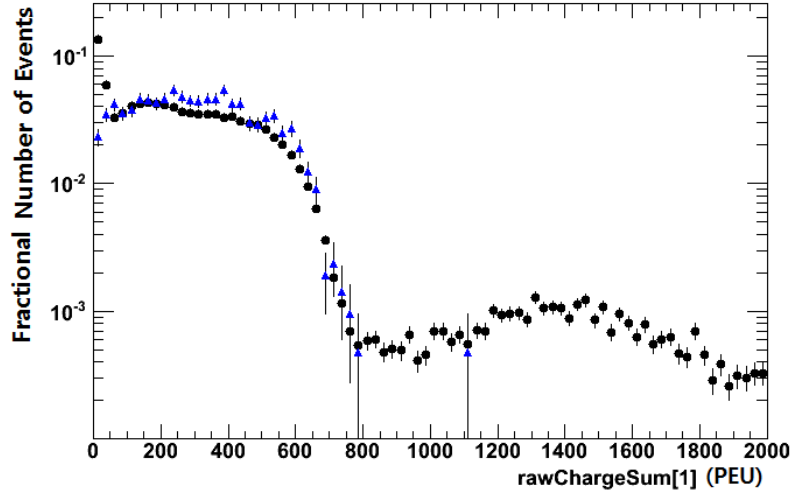
Figure 4.9: Charge distribution of the first delayed time bin for all stopping tracks. In the data, there is a large peak near zero. The data is black circles and the MC simulation is blue triangles.
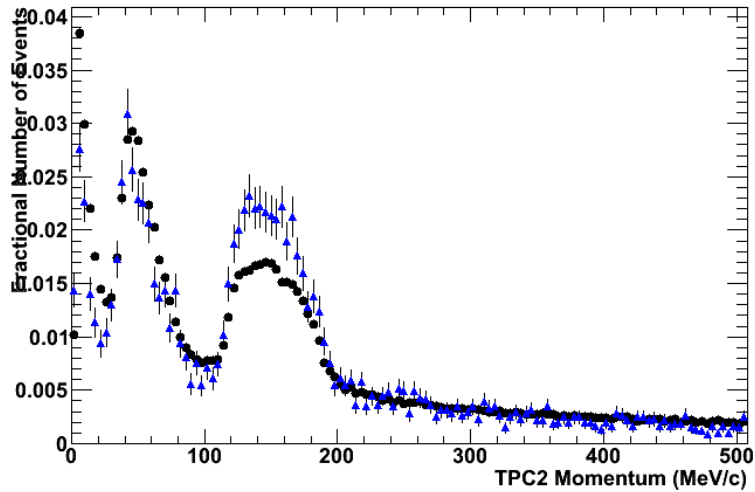

Figure 4.10: TPC2 momentum distribution after the geometry cut.

momentum cut was chosen to be as loose as possible to avoid biasing the sample.

Figure 4.10 shows the TPC2 momentum distribution after the geometry cut. Most events have momentum less than 200 MeV/c. We chose the cut on 300 MeV/c which is further than 200 MeV/c, so that we do not lose too many events by the cut.
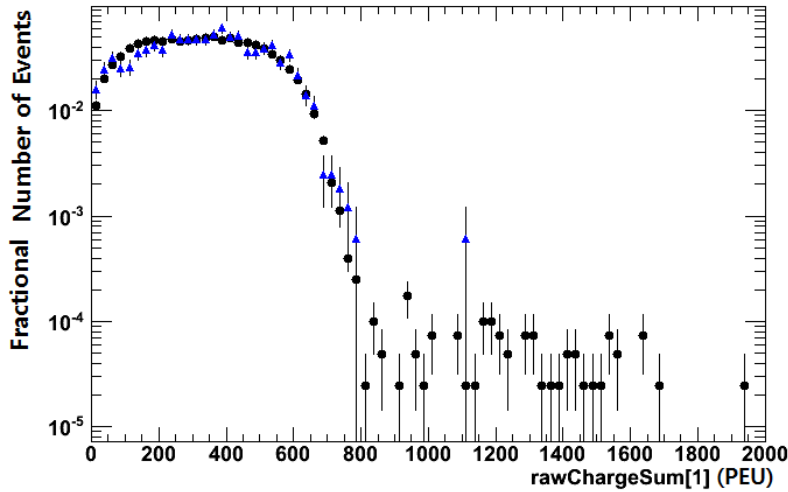

Figure 4.11: Charge distribution of the first delayed time bin for all stopping tracks after TPC2 quality cuts of the MC simulation (blue triangles) and the data (black circles).

Figure 4.11 is the charge distribution after TPC2 quality cuts. The discrepancy is removed, indicating that the cuts reduce the noise in the data.

Select stopping μ

The selected events contain all kinds of stopping particles (i.e. muons and other particles). The next step is to improve muon purity in the events. This is particle identification and can be done by TPC pulls based on the energy loss of a particle in TPCs. The pull for a track is defined via C_T. C_T denotes the truncated mean of dE/dx, which means discarding the low and high ends of dE/dx distribution. The truncated mean is less sensitive to large fluctuations in the energy loss. It is defined as

$$\text{Pull}_\alpha = \frac{C_T^{meas} - C_T^{exp,\alpha}}{\sqrt{\sigma_{C_T^{meas}}^2 + \sigma_{C_T^{exp,\alpha}}^2}} \qquad (4.2)$$

where α denotes a particle type, $C_T^{exp,\alpha}$ is the expected value of a particle of type α, C_T^{meas} is the corresponding value measured by the TPCs, and σ is the standard deviation of the C_T distribution. The C_T is scaled by the expected variations in the measurement so that its value can be interpreted as the number of standard deviations the measured C_T is from the expectation for a given particle hypothesis.
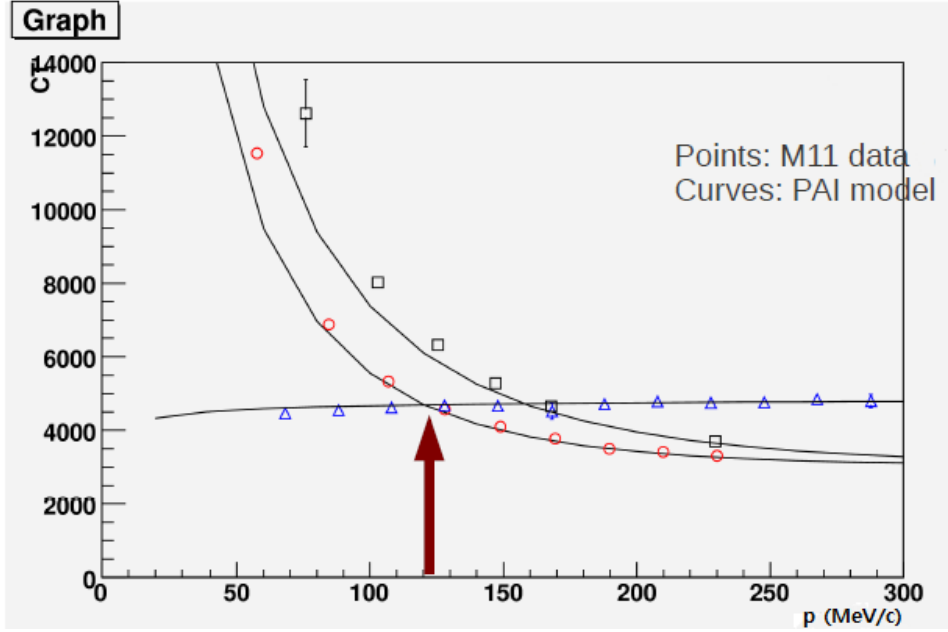

Figure 4.12: C_T versus momentum distribution. The blue triangles are the measured C_T values for electrons, and the red circles are for muons. The lines are the predicted values. The muon line and electron line cross at 120 MeV/c [67].

If Pull_α is close to zero, the reconstructed object has dE/dx consistent with the particle α. If Pull_α has a large positive value, the measured C_T is larger than the expected C_T relative to the expected uncertainty. Otherwise, if Pull_α has a large negative value, the reconstructed object has much lower measured C_T than the expected C_T. The latter two cases cannot satisfy the α particle hypothesis.
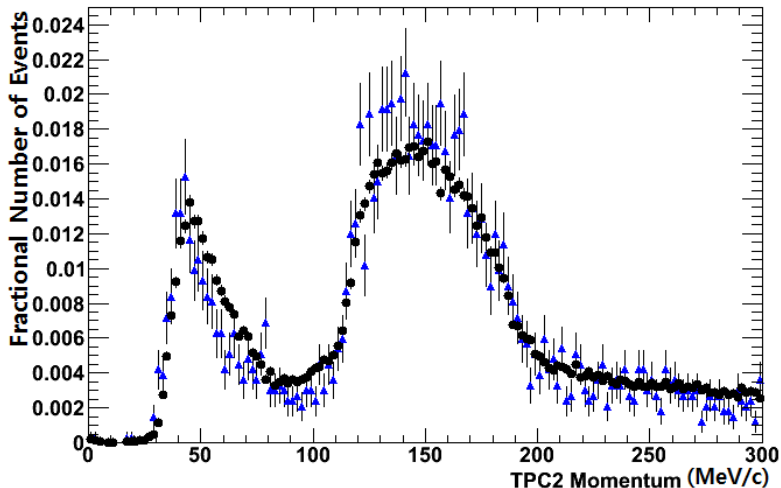
Figure 4.13: Momentum distribution of the stopping events of the MC simulation (blue triangles) and the data (black circles). The peak is at around 150 MeV/c close to where the μ line and e line cross in Figure 4.12.

In principle, the TPC pulls can be used to identify particle type by accepting or excluding the particle hypothesis. For example, to select μ and reject e, the electron hypothesis is excluded and the μ hypothesis is accepted. In other words, events with Pull_μ close to zero will be accepted, while events Pull_e close to zero will be excluded.

The Pull_μ and Pull_e distribution of the stopping events are shown in Figure 4.14 and Figure 4.15. Pull_μ is peaked at zero. However, Pull_e distribution has two peaks, one centered at zero and one at slightly negative values.

Figure 4.12 shows the mean C_T versus momentum for μ and e below 300 MeV/c. The markers are measurements of C_T from M11 beam test at TRIUMF and the lines are predicted behavior from a model called PAI [68]. The line which follows the triangular markers, which is quite flat, is the expected electron C_T from this model. The μ line is the curve plot which follows the circular markers. They cross at 120 MeV/c. Figure 4.13 shows the momentum distribution of the TPC2 track for the sample of stopping muons we are using. As we will see later, in the figure, the left peak (50 MeV/c) corresponds to electrons, while the right peak (150 MeV/c) corresponds to muons. Usually, the cosmic electrons have less momentum

69
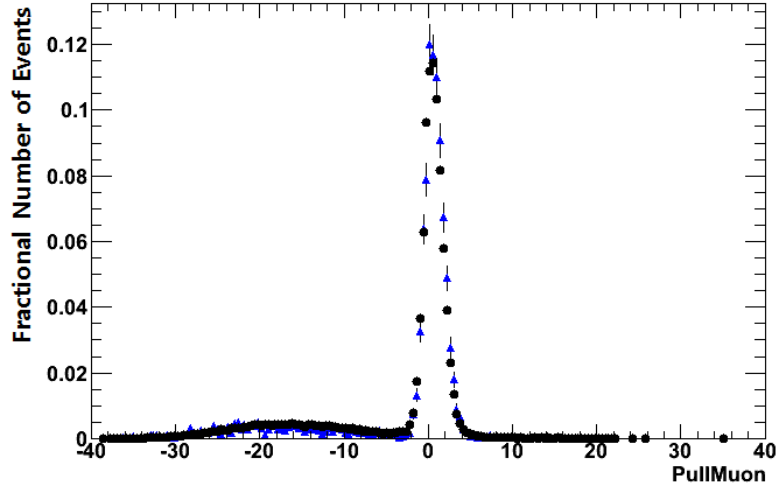
Figure 4.14: Muon pull of the stopping events for the MC simulation (blue triangles) and the data (black circles).
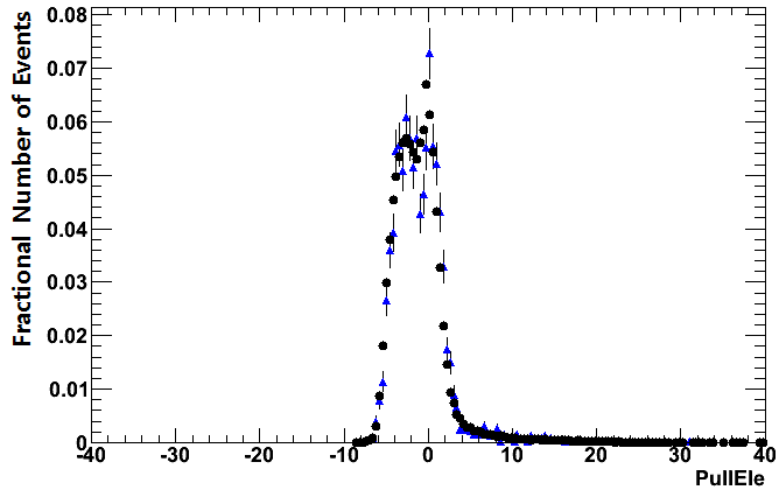

Figure 4.15: Electron pull of the stopping events for the MC simulation (blue triangles) and the data (black circles).

than the cosmic muons [69]. The higher momentum corresponding to muons is peaked at 150 MeV/c which is the momentum where the lines cross in Figure 4.12. So it is difficult to separate muons and electrons using C_T at this momentum. The next few paragraphs and plots illustrate the difficulty in using C_T to select muons and reject electrons.
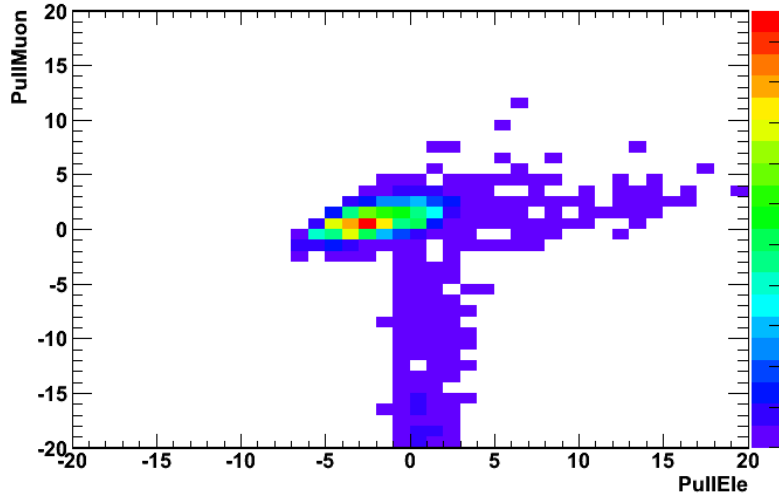

Figure 4.16: Muon pull versus electron pull for the stopping events of the MC simulation.

Figure 4.16 and 4.17 show Pull$_\mu$ versus Pull$_e$ plots of the stopping tracks for the MC simulation and the data, respectively. The highest density region is centered at zero Pull$_\mu$. But the stopping tracks also include electron-like events (the low density vertical band centered at zero Pull$_e$). If we reject the band, we also lose some events which are likely muons.

In Figure 4.12, C_T of muons is larger than that of electrons at momentum higher than 120 MeV/c. If the measured C_T is close to the predicted value on the muon line, Pull$_\mu$ has a small value near zero, while Pull$_e$ is negative.

Figure 4.18 shows the pull distribution of the events with momentum lower than 120 MeV/c for the data. These low momentum events are mostly electron-like (red dashed box). But some of them with large positive Pull$_e$ might be low momentum muons (black dotted box).

Figure 4.19 shows the pull distribution of the events with momentum higher than 120 MeV/c for the data. For the events, the distribution is roughly linear. This is because of the fact that Pull$_\mu$ and Pull$_e$ are both
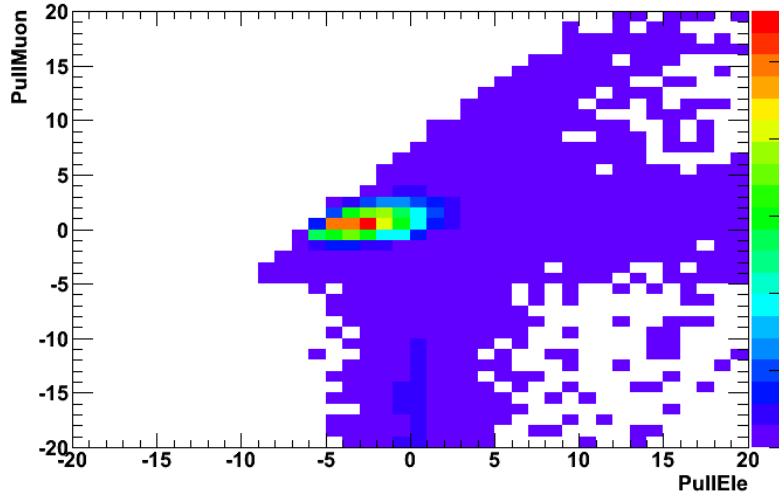
Figure 4.17: Muon pull versus electron pull for the stopping events of data.
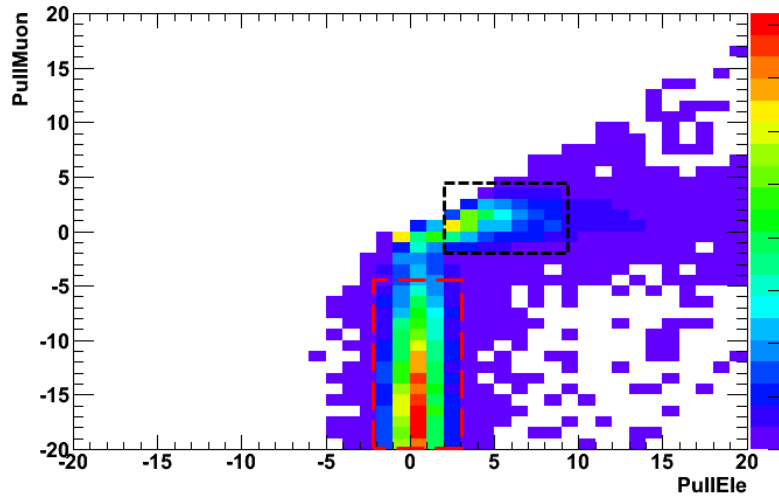
Figure 4.18: Pull$_\mu$ versus Pull$_e$ for the stopping tracks with momentum lower than 120 MeV/c, which is the intersection point in Figure 4.12 (the data). The events in the dashed red box are electron-like, while the events in the dotted black box are muon-like.
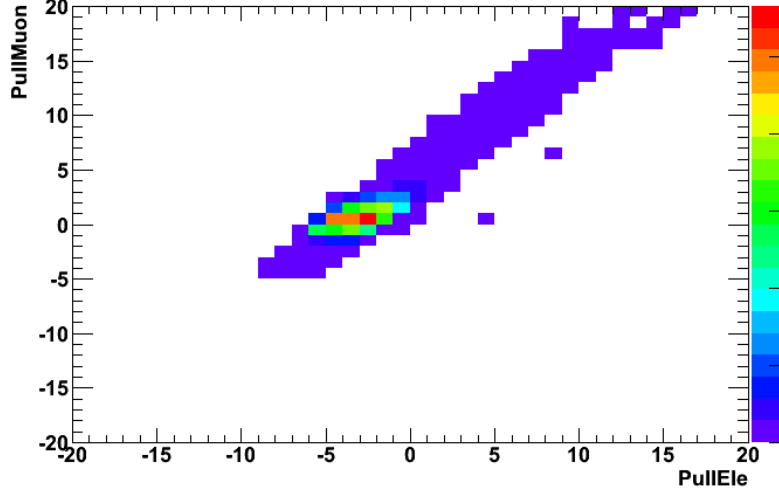
Figure 4.19:   Pull$_\mu$ versus Pull$_e$ for the stopping tracks with momentum higher than 120 MeV/c, which is the intersection point in Figure 4.12 (the data).

roughly flat when the momentum is above 120 MeV/c.

As discussed previously, the behavior Pull$_e$ and Pull$_\mu$ in the momentum region of the sample we are using is not much different. That is, it is hard to use Pull$_e$ to remove electron contamination. Instead of the TPC pulls, we also consider the relation between track length in FGD1 and momentum coming from the TPC2 track. We assume that the track enters from the downstream, so that the track length estimation is based the upstream-most hit in z and the track angle. Figure 4.20 explains how this is done.

We used the downstream z of the fiducial volume of FGD1 rather than the maximum z position of the first time bin, because we already know where the track is coming from and what the maximum z position should be. We expect typically a muon track is shorter than a electron track at the same momentum because it has higher mass.

Figure 4.21 and 4.22 clearly shows two separated dense bands for both the MC simulation and data, respectively. The right band is from μ. To only select μ, we put two boundaries on either side of the μ band. The left line passes the two points (90 MeV/c , 100 mm) and (150 MeV/c , 400 mm). The right line passes the two points (160 MeV/c , 100 mm) and (220 MeV/c , 400 mm). The equations of the lines are
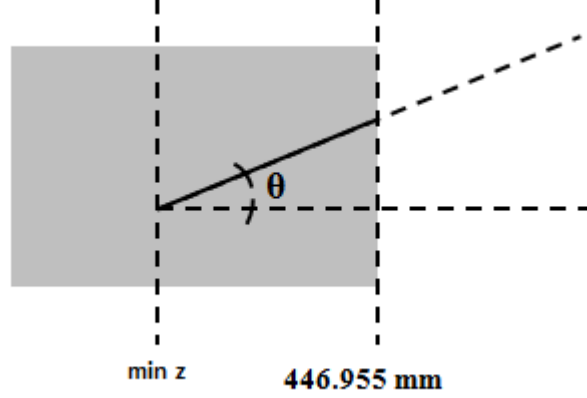
Figure 4.20: The θ is a polar angle with respect to the direction of TPC2 track. The z position difference is calculated by subtracting of the downstream edge of FGD1 and the minimum z position of the first time bin.

$$(d - 100 \text{ mm}) = \frac{(400 \text{ mm} - 100 \text{ mm})}{(150 \text{ MeV/c} - 90 \text{ MeV/c})}(p - 90 \text{ MeV/c}) \qquad (4.3)$$

$$(d - 100 \text{ mm}) = \frac{(400 \text{ mm} - 100 \text{ mm})}{(220 \text{ MeV/c} - 160 \text{ MeV/c})}(p - 160 \text{ MeV/c}) \qquad (4.4)$$

where d is the track length in mm and p is the momentum in MeV/c.
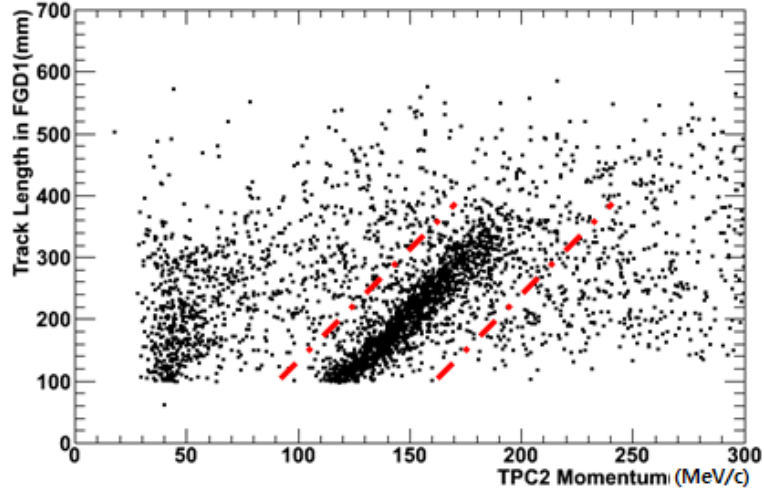
Figure 4.21: Track length in FGD1 versus momentum in the MC simulation. Muon candidates are selected between the red dashed lines.
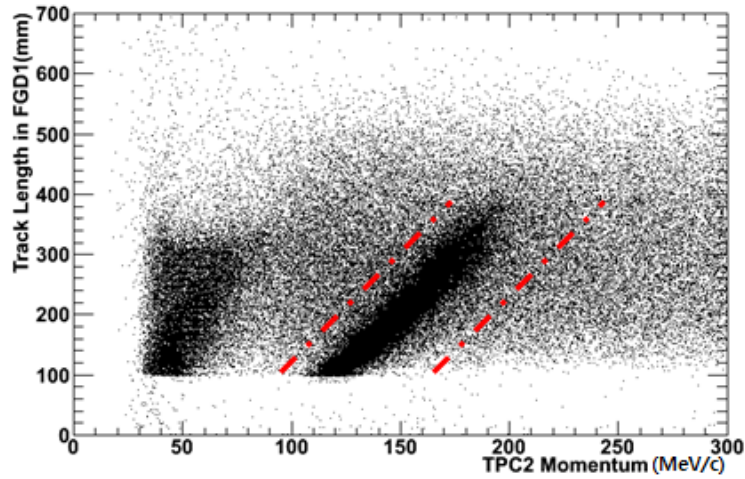

Figure 4.22: Track length in FGD1 versus momentum in the data. Muon candidates are selected between the red dashed lines.

The Pull$_\mu$ distribution after the track length cut is shown in Figure 4.23. The bump below zero is gone. (See Figure 4.14) and only muon-like events are left. Meanwhile, Figure 4.24 shows Pull$_e$ distribution after the cut. The peak at zero corresponding to electrons is removed, but the other peak corresponding to muons remains.
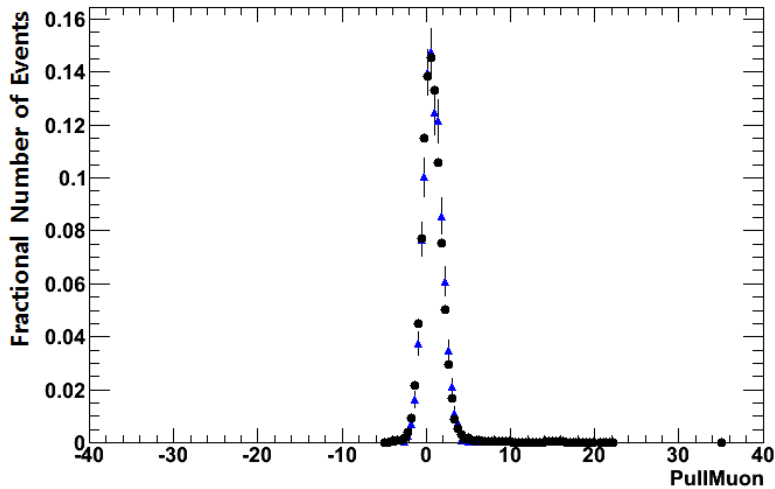
Figure 4.23: After the track length cut, muon pull of the stopping events for the MC simulation (blue triangles) and the data (black circles).

To be more clear, looking at Figure 4.25 and Figure 4.26, the track length cut successfully removes the tail in Pull$_\mu$ and the peak in Pull$_e$ which correspond to tracks that are not μ. But, the data still has a tail where Pull$_\mu$ and Pull$_e$ have similar values. To reduce these events, an additional cut requiring $|\text{Pull}_\mu| < 2.0$ is made.
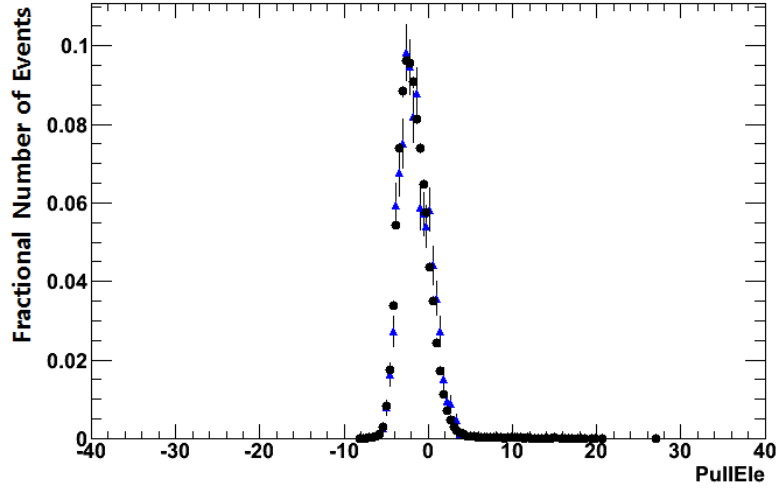
Figure 4.24: After the track length cut, electron pull of the stopping events for the MC simulation (blue triangles) and the data (black circles).
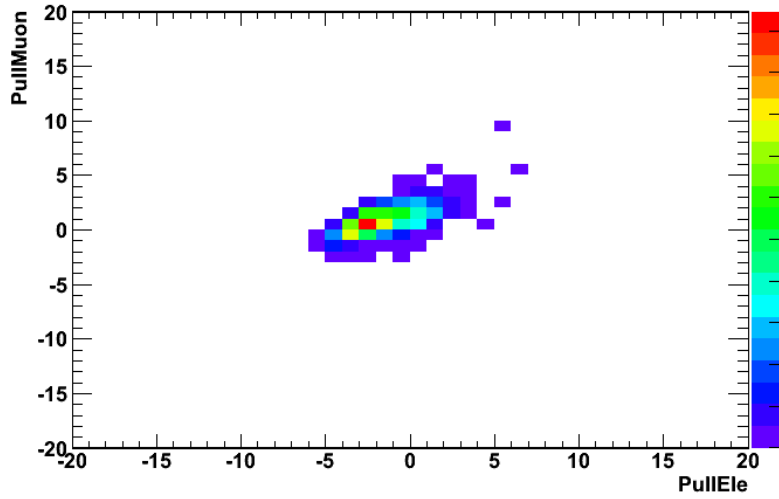
Figure 4.25: After the track length cut, muon pull versus electron pull for the stopping events of the MC simulation.
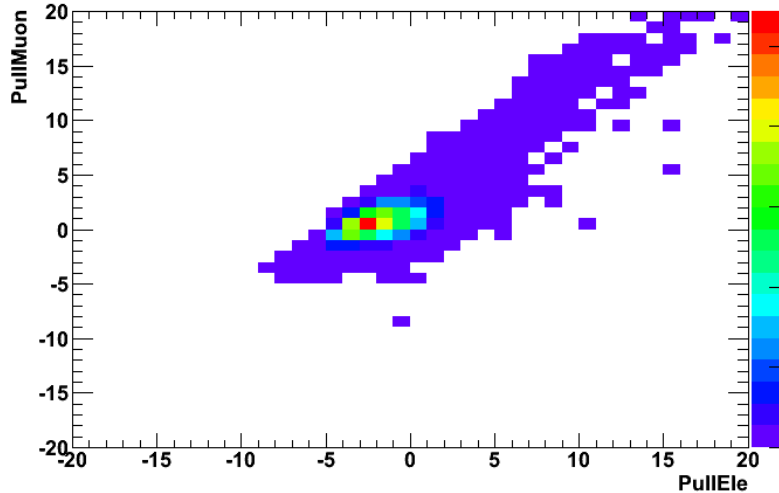
Figure 4.26: After the track length cut, muon pull versus electron pull for the stopping events of data.

4.5.2 Select μ with a Michel Electron

Now we have a clean sample of the stopping μ selected from the cosmic events. Finally, to see how many Michel electrons are tagged by the FGD time binning method, we apply the Michel electron cut in the same way as in the ν_μ analysis. We identify muons which

- have more than one delayed time bin

- the highest charge time bin has a charge higher than 200 PEU

4.6 μ Lifetime Plots

The time difference distribution is expected to be exponentially decaying. The function to fit the distribution of the time difference is defined as

$$f(\Delta\mathrm{T}) = p_0 + p_1 \times e^{-\Delta\mathrm{T}/p_2} \qquad (4.5)$$

where $\Delta\mathrm{T}$ is the reconstructed time difference of the first bin and the delayed bin with the highest charge. The p_0, p_1, and p_2 would be determined using a fit to the data. p_0 accounts for any remaining background such as cosmic

78

rays within the same event that is flat in this time difference. p_1 depends on the size of samples and p_2 represents the mean lifetime of muons.

A time bin has the minimum/maximum time of hits within the time bin and the bin time is defined as the average of the two times:

$$\text{BinT} = \frac{\text{minT} + \text{maxT}}{2} \tag{4.6}$$

The μ^- lifetime in carbon is 2.02 μs [70]. In the B-field perpendicular to the beam direction, the backward-going positive particles are bent downwards and leave the detector before stopping in FGD1. Hence, most μ stopping in FGD1 are negative. Sometimes the μ^- might be captured by a nucleus. In these cases, there is no Michel electron, thus the μ^- lifetime is shorter than the normal μ lifetime of 2.2 μs.

Since the capture process does not produce a Michel electron, the Michel electron cut does not actually fail to identify a Michel electron. As the result, the Michel electron detection efficiency will include the capture rate as part of the inefficiency in these cases.

Element	Mean lifetime(ns)	Total capture rate(s^{-1})
C	2020 ± 20	$44 \pm 10 \times 10^3$
O	1812 ± 12	$98 \pm 3 \times 10^3$

Table 4.2: μ^- lifetime and capture rates in different materials [70].

The μ^- lifetime of the MC simulation, measured by the stopping μ with a Michel electron, is in Figure 4.27. The fitted value of the lifetime is $2.22\pm0.17\mu$s. While the MC simulation has low statistics, it is consistent with the expected lifetime. For the data, the lifetime is $2.05\pm0.03\mu$s, consistent with the actual muon lifetime.

4.7 Summary of Selection Cuts

To understand the Michel electron detection efficiency, it is necessary to first have a pure sample of stopping muons. The first two cuts, geometry and TPC2 quality, are to veto non-stopping particles. The next two cuts, track length and Pull_μ, remove electrons, which are not expected to produce Michel electrons. The last cut is the current Michel electron cut used in the current ν_μ CCQE selection. Up to the fourth cut, the stopping muon
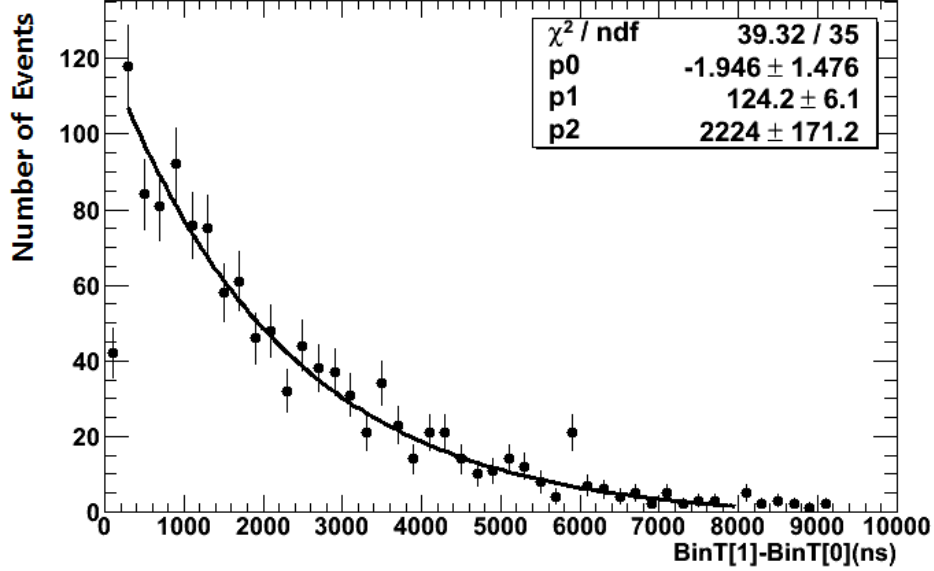
Figure 4.27: Bin time difference for stopping μ with a Michel electron (the MC simulation). Fit with Equation 4.5.

purity is improved. Afterwards, only the muons with a Michel electron are identified by the Michel electron cut.

1. Select stopping events

   - Geometry

     The outermost hit of the first bin have to be in the box defined in Figure 4.6
   - TPC2 Quality

     No TPC1 track and 1 TPC2 track

     Number of hits in TPC2 track > 60

     Momentum of TPC2 track < 300 MeV/c

2. Select μ in the stopping events

   - $5(\frac{\text{mm}}{\text{MeV/c}})(\text{p} - 160 \text{ MeV/c}) + 100 \text{ mm} < \text{d} < 5(\frac{\text{mm}}{\text{MeV/c}})(\text{p} - 90 \text{ MeV/c}) + 100 \text{ mm}$
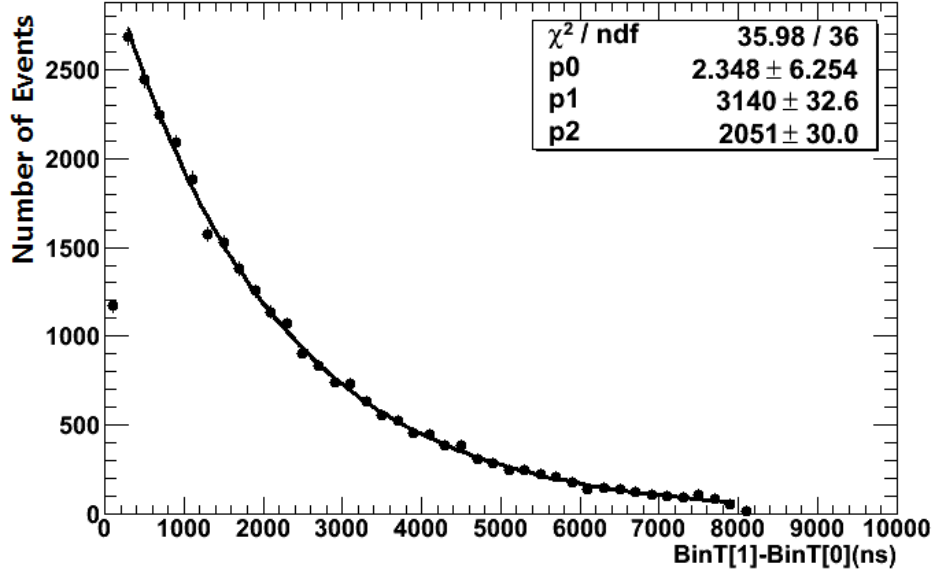
Figure 4.28: Bin time difference for stopping μ with a Michel electron (the data). Fit with Equation 4.5.

- $|\text{Pull}_\mu| < 2.0$

3. Select μ with a Michel electron in the stopping μ events

- Charge deposit in one of the delayed time bins should be larger than 200 PEU

4.8   Data and MC Simulation Comparison

Now we look at how many events survive after each cut with the MC simulation compared to the data. The numbers of events passing each cut are summarized in Table 4.3. In this section, the fractional number of events is defined relative to the events passing the previous cut:

$$\text{Fractional number of event} = \frac{\text{number of events passing the cut}}{\text{number of events passing the previous cuts}}$$
(4.7)

	MC		data	
	Events	Fraction	Events	Fraction
Total Events	82,042		7,697,733	
Geometry	15,941	0.194	801,432	0.104
TPC2 quality	3,339	0.209	96,487	0.120
Length in FGD1	1,909	0.572	50,396	0.522
Pull Muon	1,636	0.865	43,618	0.866
Charge Sum	1,051	0.642	25,865	0.593

Table 4.3: The numbers of events passing single cut. The fraction takes a ratio of the number of events passing a cut to the number events passing the previous cut.
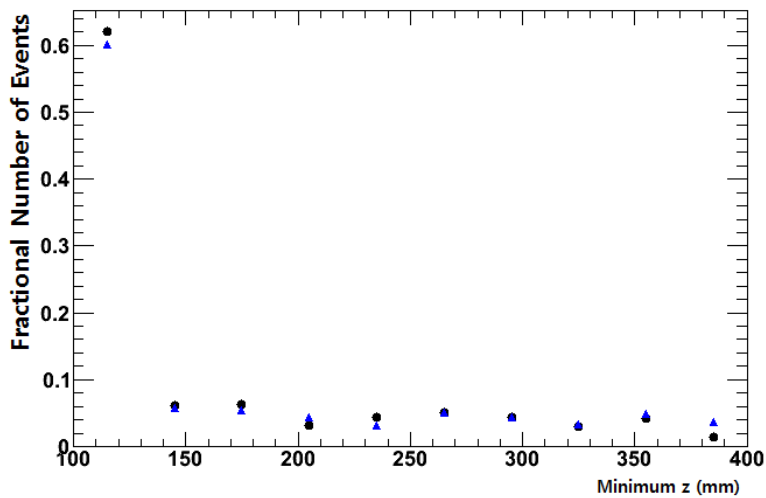
Figure 4.29: The distributions of the minimum z position of the first time bin of the MC simulation (blue triangles) and the data (black circles).

Figure 4.29 shows the distributions of the minimum z position of the first time bin for all total cosmic events. Almost 60% events are at 110 mm for both the MC simulation (blue triangles) and the data (black circles). These are through-going events.

By applying the geometry cut, the through-going events are rejected. The fraction of events surviving the cut as a function of the minimum z

position is shown in Figure 4.30. This ratio shows how the cuts affect the data and the MC simulation. The events stopping at the last couple of layers are also removed by the reduced downstream z cut.
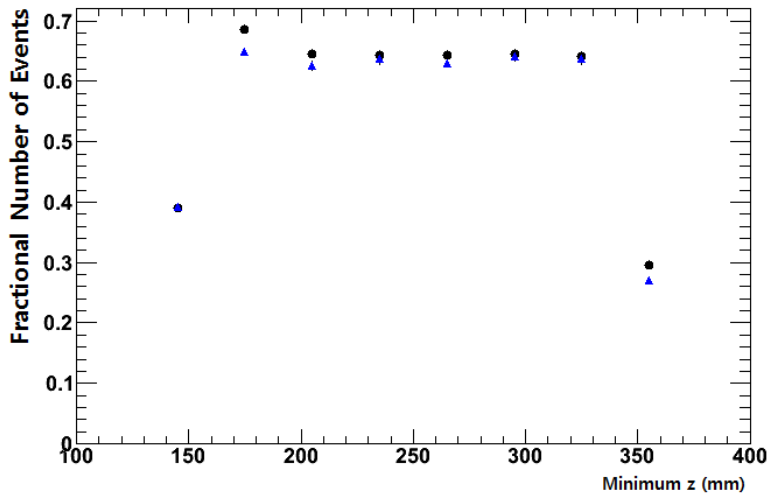

Figure 4.30: The fractional number of events after the geometry cut as a function of the minimum z position of the first time bin for the MC simulation (blue triangles) and the data (black circles).

After the TPC2 quality cut, the fractional number of events of the MC simulation and the data do not agree as shown in Figure 4.31. Fewer events in the data pass the TPC2 cut compared to the MC simulation, so there is a background present in the data that is not present in the MC simulation which increases the denominator. This is consistent with the result that the MC simulation/the data discrepancy on the charge distribution has been eliminated by the cut. The data also has worse resolution so the fractional number of events in the data may be worse.

Figure 4.32 shows the fractional number of events after applying the muon selection cuts, which are the track length cut and the pull muon cut. Now the fractional number of events looks more similar. But it seems that the fractional number of events is higher for the MC simulation for longer tracks. As shown in Figure 4.26, there are more contamination in the data after the geometry cut, the TPC cut, and the track length cut, while there are not in the MC simulation. Therefore, less events in the data pass the pull muon cut. This causes the lower fractional number of events in the

83
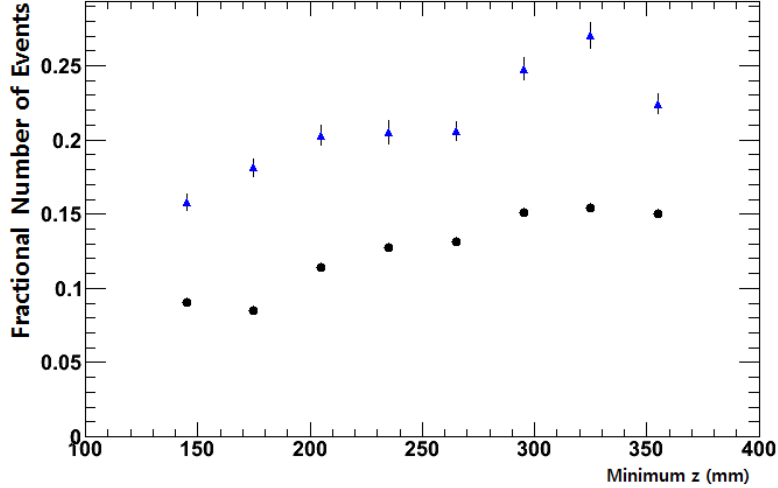
Figure 4.31: The fractional number of events after the TPC cut as a function of the minimum z position of the first time bin for the MC simulation (blue triangles) and the data (black circles).

data.

Finally, the top of Figure 4.33 shows the fractional number of events after the Michel electron cut, which is the Michel electron detection efficiency in FGD1.

4.9 Result

The bottom plot in Figure 4.33 shows the minimum z position distribution of the first time bin of the MC simulation (blue triangles) and the data (black solid line). The minimum z of FGD1 fiducial volume is 136.875 mm and the maximum z is 446.955 mm. The top plot is the efficiency as a function of the minimum z position. Over most of the z range, the MC simulation (blue triangles) and the data (black circles) agree reasonably well.

The total numbers of cosmic events are 82,042 for the MC simulation and 7,697,733 for the data.

In the MC simulation, 1,636 stopping μ were identified, of which 1,051 events passed the Michel electron cut, resulting in an efficiency of 0.642±0.012. Meanwhile, in the data, 43,618 stopping μ were identified, of which 25,865 events are left. The efficiency is 0.593±0.003 (See Table 4.3).

84
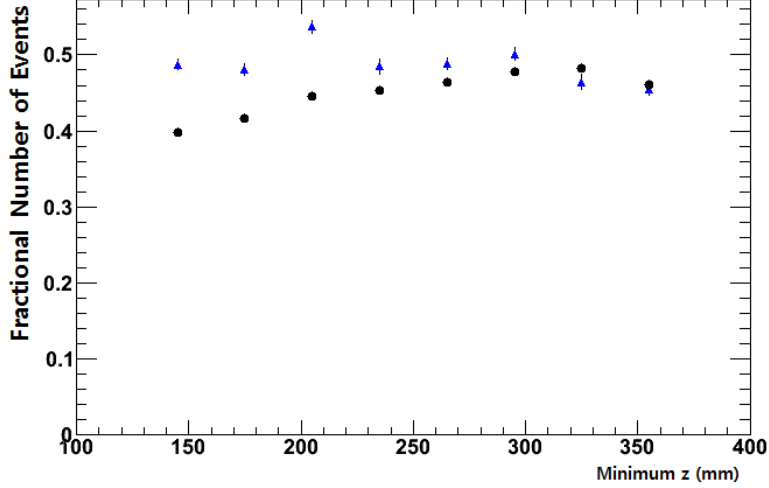
Figure 4.32: The fractional number of events after the muon selection cuts, the track length and pull muon, as a function of the minimum z position of the first time bin for the MC simulation (blue triangles) and the data (black circles).

The data efficiency is lower than the MC simulation efficiency and the difference is 0.087±0.012. The difference is calculated as

$$\text{Difference} = \frac{(\text{MC Efficiency}) - (\text{data Efficiency})}{\text{data Efficiency}} \tag{4.8}$$

4.10 Implications for the Neutrino Interactions

Michel electron studies using time-bin analysis in the neutrino beam are difficult because the beam data has background in which there are delayed time bins not due to Michel electrons.

So we used cosmic events. Cosmic muons have a well known behavior in the detector and are abundant compared to the neutrino interactions, allowing a high statistics study. The purpose of the study is to estimate how often a Michel electron is found when μ stops in FGD1 and how different the detection efficiency is in the data and the MC simulation.

Using the result, we can infer how many events the Michel electron cut will remove in real beam data compared to the beam MC.
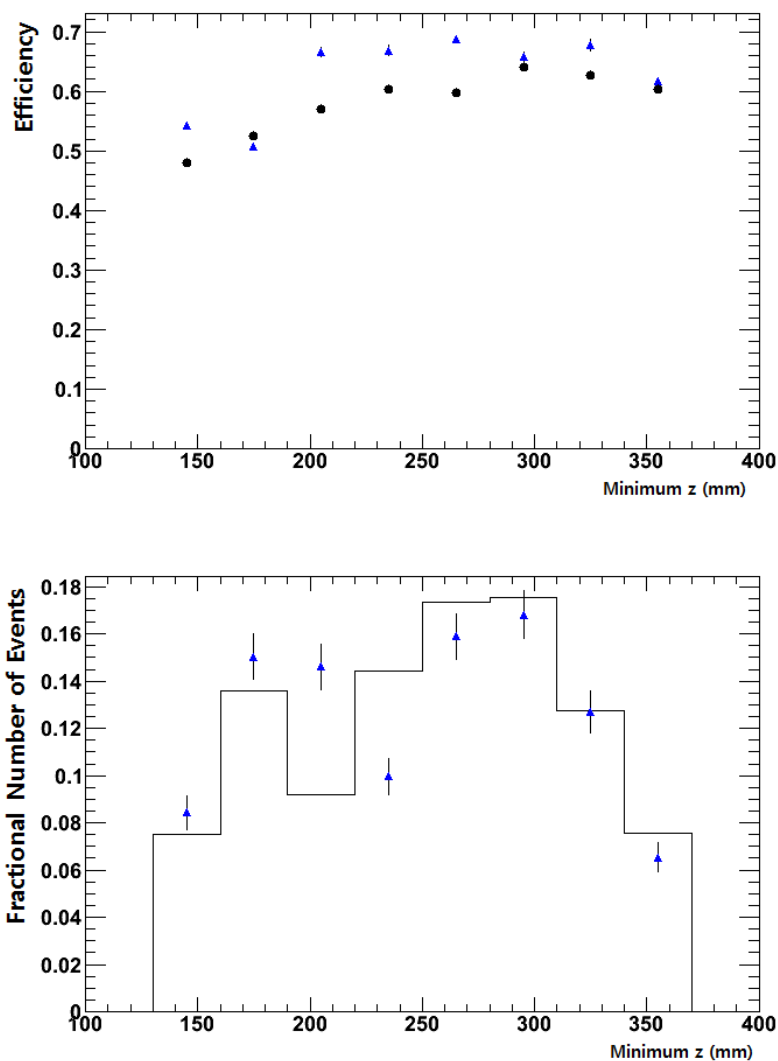
Figure 4.33: The top figure is the final efficiency as a function of the minimum z position of the first time bin. The bottom figure is the corresponding z distribution of the finally selected events. The numbers of events are normalized to 1. Blue indicates the MC simulation and black is the data.

4.10.1 The Inclusive CC Selection

The majority of neutrino interactions are CC interactions. The ν_μ analysis starts from the inclusive ν_μ CC selection. Since the incoming ν_μ are transformed to μ^- via W^+ boson, the ν_μ CC interactions can be identified by the outgoing μ^-. That is, the main idea to select inclusive CC events is identify μ^--like particles with high momentum in the FGD fiducial volume. The CC selection cuts are

- the highest momentum track in the event should be negative

- the highest momentum track in the event is required to have muon PID

The muon PID cut is based on the PID likelihood, which is defined as

$$Likelihood_\mu = \frac{\text{Prob}(\mu)}{\text{Prob}(\mu) + \text{Prob}(\pi) + \text{Prob}(p) + \text{Prob}(e)} \qquad (4.9)$$

The PID is based on the TPC dE/dx.

To be a muon track, the track has to be satisfy $Likelihood_\mu > 0.05$.
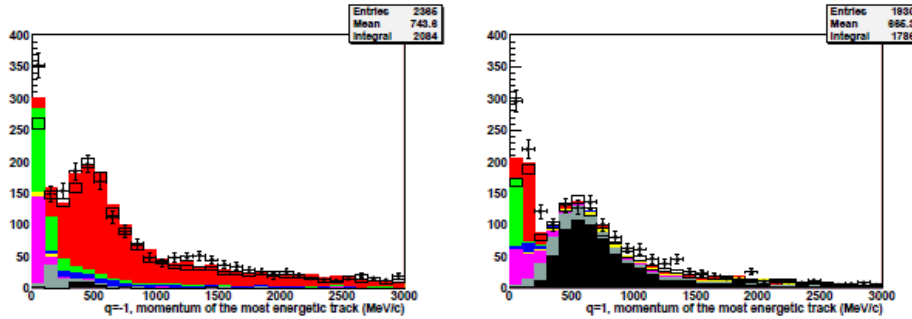
Figure 4.34: Momentum distribution of the highest momentum tracks for negative (left) and positive (right) tracks [71]. Muons are in red and protons are in black.

Figure 4.34 shows the momentum distributions of the highest momentum tracks for negative and positive tracks [71]. As shows in the left figure in red, the negative tracks with the highest momentum are mostly muons.

The inclusive CC selection selects 88.83% of all ν_μ CC interactions in Run 1 (from Jan. 2010 to Jun. 2010) and 88.99% in Run 2 (from Nov. 2010) according to the MC simulation. The result is shown in Table 4.4.

	Run 1	Run 2
CC	88.83%	88.99%
NC	$2.93 \pm 0.31\%$	$2.75 \pm 0.31\%$
interactions in non-Fiducial	$7.55 \pm 0.77\%$	$7.57 \pm 0.49\%$
anti-neutrino interactions	$0.69 \pm 0.24\%$	$0.75 \pm 0.16\%$

Table 4.4:   The inclusive CC ν_μ selection result [72].

After the inclusive CC selection, the next step is to separate CCQE and non-CCQE interactions in the inclusive CC samples. In general, CCQE interactions produce a negative muon and a proton in the final state, while $CC1\pi^+$ have an additional pion. The pion usually has less momentum than a muon from CCQE, so it often stops and decays to a muon in an FGD. The muon typically stops and decays to an electron. Using these characteristics, further cuts are used to select CCQE from the events passing the inclusive CC cuts [71].

- not more than 2 tracks in the event

- one negative track

- no Michel electrons

Figure 4.35 shows an example of CCQE interactions with two global tracks. After CCQE selection, the CCQE efficiency and purity are 38.9% and 71.5% respectively.

4.10.2   Conclusion

In the MC simulation, after the inclusive CC ν_μ selection, 1,706 events are left. The current Michel electron cut removes 85 events. According to the study, the efficiency in the data is 8.7% lower than the MC simulation, so we expect 77 events will be removed in the data. The change of 8 out of 1,706 events is a 0.5% systematic error. The numbers in the MC simulation are normalized to the data POT.
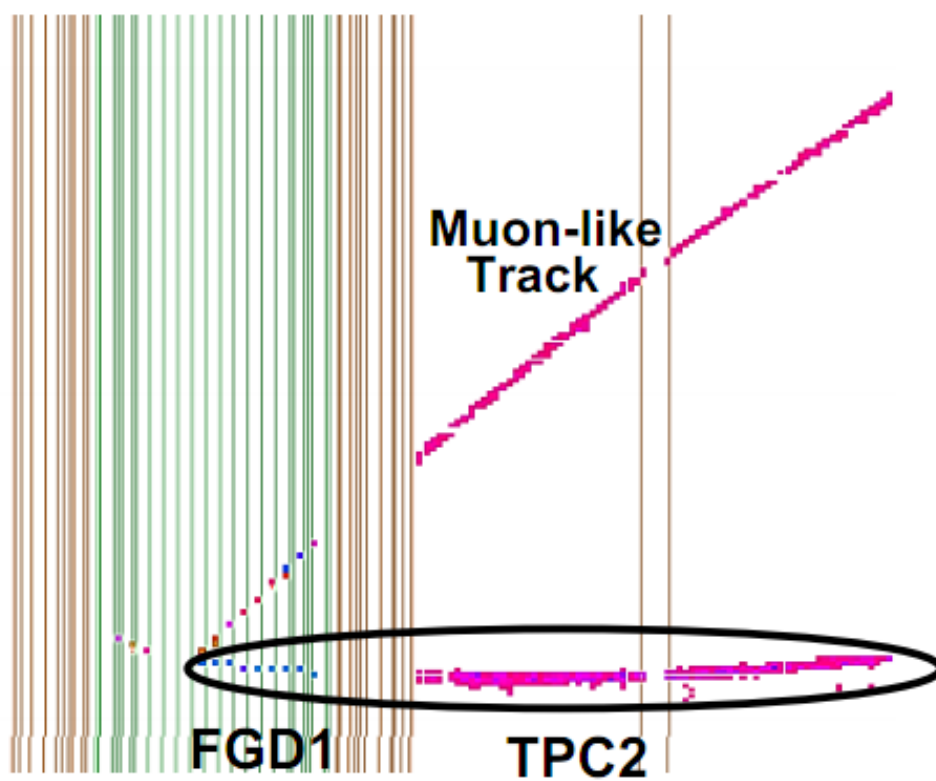
Figure 4.35:   An example of CCQE interactions with two tracks [72].

Chapter 5

Conclusion

In this thesis the efficiency of Michel electron detection has been discussed. Cosmic rays provide a large sample of muons with which to test the Michel electron identification efficiency. If a muon stops in FGD1 and decays, there is a Michel electron. The Michel electron can be identified by the FGD time binning algorithm. Since muons in FGD1 are most after negatively charged, sometimes a stopping muon does not produce a Michel electron by the capture process. This process is well understood so it should be accurately reproduced by the MC simulation. By identifying a clean sample of muons stopping in FGD1 and determining how often a Michel electron is detected, one can measure the efficiency for the Michel electron reconstruction.

Because cosmic rays have non-muon particles as well, it is necessary to identify a clean muon samples first. The stopping tracks are identified by the location of the downstream-most hit. The downstream-most hit must be in the allowed region, which is defined as the FGD1 fiducial volume with more stringent downstream z cut. We require that there is a track in TPC2, but that there is no track in TPC1. The TPC2 track should have more than 60 hits, and momentum lower than 300 MeV/c.

To reduce non-muon contamination in the selected stopping sample, particle identification using the TPC2 pull, which is based on dE/dx measurements, and the track length are used. We require the cut on the muon pull, $|\mathrm{Pull}_\mu| < 2.0$. Meanwhile, the track length cut is also required. Since electrons travel further in FGD1 before stopping than muons at the same momentum, we can distinguish electron and muons based on track length in FGD1 and momentum relation.

With these cuts, we obtain a clean sample of stopping muons that are selected independently of the Michel electron cut.

Finally, the Michel electron requirement is applied to the sample to see how many muons have Michel electrons and how well the MC simulation and the data agree. The Michel electron cut requires the charge deposit in one of the delayed bins higher than 200 PEU.

The efficiency of the MC simulation is 0.642±0.012 and the efficiency of the data is 0.593±0.003. The difference between the MC simulation and the

data is 0.087±0.012. This will be incorporated as a systematic uncertainty in the ν_μ CCQE and non-CCQE selection, which utilizes Michel electron identification.

References

[1] E. Fermi. Versuch einer theorie der β-strahlen. *Zeitschrift für Physik A Hadrons and Nuclei*, 88:161–177, 1934. 10.1007/BF01351864.

[2] Chadwick J. Intensitätsverteilung im magnetischen Spektrum der β - Starhlen von Radium B+C. *Verh. der Deutschen Physikalischen Ges.*, 16:383, 1914.

[3] F. Reines and C. L. Cowan. Detection of the free neutrino. *Phys. Rev.*, 92(3):830–831, Nov 1953.

[4] G. Feinberg. Decays of the mu Meson in the Intermediate-Meson Theory. *Phys.Rev.*, 110:1482–1483, 1958.

[5] G. Danby, J-M. Gaillard, K. Goulianos, L. M. Lederman, N. Mistry, M. Schwartz, and J. Steinberger. Observation of high-energy neutrino reactions and the existence of two kinds of neutrinos. *Phys. Rev. Lett.*, 9(1):36–44, Jul 1962.

[6] K. Kodama et al. Observation of tau-neutrino interactions. *Phys. Lett.*, B504:218–224, 2001.

[7] B. Pontecorvo. Neutrino Experiments and the Problem of Conservation of Leptonic Charge. *Soviet Journal of Experimental and Theoretical Physics*, 26:984–+, May 1968.

[8] C. Giunti and C. W. Kim. *Fundamentals of Neutrino Physics and Astrophysics*. Oxford, 2008.

[9] B. Pontecorvo. Mesonium and antimesonium. *Sov. Phys. JETP*, 6:429, 1957.

[10] Q. R. Ahmad et al. Direct evidence for neutrino flavor transformation from neutral-current interactions in the Sudbury Neutrino Observatory. *Phys. Rev. Lett.*, 89:011301, 2002.

References

[11] J. N. Bahcall and M. H. Pinsonneault. Standard solar models, with and without helium diffusion, and the solar neutrino problem. *Rev. Mod. Phys.*, 64(4):885–926, Oct 1992.

[12] Raymond Davis, Don S. Harmer, and Kenneth C. Hoffman. Search for neutrinos from the sun. *Phys. Rev. Lett.*, 20(21):1205–1209, May 1968.

[13] John N. Bahcall, Neta A. Bahcall, and Giora Shaviv. Present status of the theoretical predictions for the ^{37}Cl solar-neutrino experiment. *Phys. Rev. Lett.*, 20:1209–1212, May 1968.

[14] H. A. Bethe. Energy production in stars. *Phys. Rev.*, 55:434–456, 1939.

[15] John N. Bahcall, Aldo M. Serenelli, and Sarbani Basu. New solar opacities, abundances, helioseismology, and neutrino fluxes. *The Astrophysical Journal Letters*, 621(1):L85, 2005.

[16] J. N. Bahcall, William A. Fowler, I. Iben, Jr., and R. L. Sears. Solar neutrino flux. *Astrophys. J.*, 137:344–346, 1963.

[17] S. Turck-Chieze, S. Cahen, M. Casse, and C. Doom. Revisiting the standard solar model. *Astrophysical Journal*, 335:415–424, Dec 1988.

[18] K. S. Hirata et al. Experimental Study of the Atmospheric Neutrino Flux. *Phys. Lett.*, B205:416, 1988.

[19] K. S. Hirata, T. Kajita, and T. Kifune et al. Observation of ^8B solar neutrinos in the Kamiokande-II detector. *Phys. Rev. Lett.*, 63(1):16–19, Jul 1989.

[20] S. Fukuda et al. Solar ^8B and hep Neutrino Measurements from 1258 Days of Super-Kamiokande Data. *Phys. Rev. Lett.*, 86:5651–5655, 2001.

[21] Y. Ashie et al. A Measurement of Atmospheric Neutrino Oscillation Parameters by Super-Kamiokande I. *Phys. Rev.*, D71:112005, 2005.

[22] Q. R. Ahmad, R. C. Allen, and T. C. Andersen et al. Measurement of the rate of $\nu_e + d \rightarrow p+p+e^-$ interactions produced by ^{8}B solar neutrinos at the sudbury neutrino observatory. *Phys. Rev. Lett.*, 87:071301, Jul 2001.

[23] E. Lisi, A. Marrone, and D. Montanino. Probing possible decoherence effects in atmospheric neutrino oscillations. *Phys. Rev. Lett.*, 85:1166–1169, 2000.

References

[24] Ziro Maki, Masami Nakagawa, and Shoichi Sakata. Remarks on the unified model of elementary particles. *Prog. Theor. Phys.*, 28:870–880, 1962.

[25] Makoto Kobayashi and Toshihide Maskawa. CP Violation in the Renormalizable Theory of Weak Interaction. *Prog. Theor. Phys.*, 49:652–657, 1973.

[26] Makoto Kobayashi and Toshihide Maskawa. CP-violation in the renormalizable theory of weak interaction. *Progress of Theoretical Physics*, 49(2):652–657, 1973.

[27] Oystein Elgaroy and Ofer Lahav. Sub-eV upper limits on neutrino masses from cosmology. *Phys.Scripta*, T127:105–106, 2006.

[28] Y. Fukuda et al. Evidence for oscillation of atmospheric neutrinos. *Phys. Rev. Lett.*, 81:1562–1567, 1998.

[29] S. Yamamoto et al. An improved search for $\nu_\mu \to \nu_e$ oscillation in a long-baseline accelerator experiment. *Phys. Rev. Lett.*, 96:181801, 2006.

[30] T. Araki et al. Measurement of neutrino oscillation with KamLAND: Evidence of spectral distortion. *Phys. Rev. Lett.*, 94:081801, 2005.

[31] V. Barger, K. Whisnant, S. Pakvasa, and R. J. N. Phillips. Matter effects on three-neutrino oscillations. *Phys. Rev. D*, 22:2718–2726, Dec 1980.

[32] B. Aharmim, S. N. Ahmed, and Anthony et al. Low-energy-threshold analysis of the Phase I and Phase II data sets of the Sudbury Neutrino Observatory. *Phys. Rev. C*, 81(5):055504, May 2010.

[33] K. Nakamura and S.T. Petcov(Particle Data Group. Neutrino mass, mixing, and oscillations. 2010.

[34] P. Adamson, C. Andreopoulos, and R. Armstrong et al. Measurement of the neutrino mass splitting and flavor mixing by minos. *Phys. Rev. Lett.*, 106:181801, May 2011.

[35] Y. Ashie et al. Evidence for an oscillatory signature in atmospheric neutrino oscillation. *Phys. Rev. Lett.*, 93:101801, 2004.

[36] P. Adamson et al. Improved search for muon-neutrino to electron-neutrino oscillations in MINOS. 2011.

References

[37] K. Abe et al. Indication of Electron Neutrino Appearance from an Accelerator-produced Off-axis Muon Neutrino Beam. *Phys. Rev. Lett.*, 107:041801, 2011.

[38] K. Matsuoka. *Measurement of the Neutrino Beam with the Muon Monitor and the First Result of the T2K Long-Baseline Neutrino Oscillation Experiment.* PhD thesis, Kyoto University, 2011.

[39] N. Abgrall et al. Calibration and analysis of the 2007 data. CERN-SPSC-2008-018.

[40] L. S. Whitehead. *Measurement of the Single Charged Pion Production Cross Section in Charged-Current Neutrino-Carbon Interactions.* PhD thesis, Stony Brook University, 2007.

[41] T. Ishida. Neutrino and other beam-lines at J-PARC. In *Particle Accelerator Conference PAC07.*

[42] Yuichi Oyama. Current status of the T2K experiment. 2011.

[43] A. Carver. *Electron identification in and performance of the ND280 Electromagnetic Calorimeter.* PhD thesis, The University of Warwick, 2010.

[44] Y. Fukuda et al. The Super-Kamiokande detector. *Nucl. Instrum. Meth.*, A501:418–462, 2003.

[45] K. Abe, Y. Hayato, and T. Iida et al. Solar neutrino results in super-kamiokande-iii. *Phys. Rev. D*, 83:052010, Mar 2011.

[46] D. Green. *The Physics of Particle Detectors.* Cambridge, 2000.

[47] S. Fukuda, Y. Fukuda, and T. Hayakawa et al. The super-kamiokande detector. *Nuclear Instruments and Methods in Physics Research Section A: Accelerators, Spectrometers, Detectors and Associated Equipment*, 501(2-3):418 – 462, 2003.

[48] Claude Amsler et al. Review of particle physics. *Phys. Lett.*, B667:1–1340, 2008.

[49] T2K Collaboration K. Abe, N. Abgrall, and H. Aihara et al. The T2K Experiment. *arXiv:1106.1238*, June 2011.

[50] T2K ND280 TPC collaboration. Time Projection Chambers for the T2K Near Detectors. *arXiv:1012.0865*, December 2010.

References

[51] N. Abgrall, B. Andrieu, and P. Baron et al. Time Projection Chambers for the T2K Near Detectors. *Nuclear Instruments and Methods in Physics Research Section A: Accelerators, Spectrometers, Detectors and Associated Equipment*, 637(1):25 – 46, 2011.

[52] P. Baron et al. Architecture and implementation of the front-end electronics of the time projection chambers in the T2K experiment. *IEEE Trans. Nucl. Sci.*, 57:406–411, 2010.

[53] Marco Zito. SuperBeam Experiments: T2K, NOνA and Beyond. *AIP Conf. Proc.*, 1222:10–14, 2010.

[54] ND280 Fine-Grained Detector Technical Design Report. T2K Internal Document.

[55] ND280 Collaboration. Document for ND280 review. T2K Internal Document.

[56] L. Trung. *Event reconstruction and energy calibration using cosmic muons for the T2K pizero detector*. PhD thesis, Stony Brook University, 2009.

[57] Conceptual Design Report. T2K Internal Document.

[58] M. Ziembicki, R. Sulej, S. Aoki, J. Blocki, J. Brinson, et al. The SMRD subdetector at the T2K near detector station. *Acta Phys.Polon.*, B41:1579–1584, 2010.

[59] Y. Hayato. A Neutrino Interaction Simulation Program Library NEUT. *Acta Physica Polonica B*, 40:2477–+, September 2009.

[60] C. Andreopoulos, A. Bell, and D. Bhattacharya et al. The genie neutrino monte carlo generator. *NUCL.INSTRUM.METH.A*, 614:87, 2010.

[61] John Allison, K. Amako, J. Apostolakis, H. Araujo, P.A. Dubois, et al. Geant4 developments and applications. *IEEE Trans.Nucl.Sci.*, 53:270, 2006.

[62] S. P. Hastings. A Saturation Calibration of Hamamatsu's Multi-Pixel Photon Counter. Master's thesis, The University of British Columbia, 2010.

[63] F. Sanchez, A. Hillairet, and B. Jamieson et al. ND280 reconstruction. T2K Internal Document.

References

[64] W. Qian. T2K ND280 Cosmic Trigger Module. T2K internal document.

[65] P.-A. Amaudruz, M. Barbi, and P. Birney et al. The T2K Fine-Grained Detector. To be published.

[66] D. Heck, J. Knapp, J. N. Capdevielle, G. Schatz, and T. Thouw. *CORSIKA: a Monte Carlo code to simulate extensive air showers.* February 1998.

[67] C. Giganti, J. Tephany, and M. Zito. Momentum calibration with the first ND280 data. T2K Internal Document.

[68] M G P Homem, P Iza, and L S Farenzena et al. Cross-section measurements of photoabsorption and ionization quantum yields for tetrahydrofuran in the vacuum-ultraviolet energy range. *Journal of Physics B: Atomic, Molecular and Optical Physics*, 42(23):235204, 2009.

[69] Lukasz Stawarz, Vahe Petrosian, and Roger D. Blandford. On the Energy Spectra of GeV/TeV Cosmic Ray Leptons. *Astrophys.J.*, 710:236–247, 2010.

[70] T. Suzuki, D. F. Measday, and J. P. Roalsvig. Total nuclear capture rates for negative muons. *Phys. Rev. C*, 35:2212–2224, Jun 1987.

[71] A. Cervera, F. Dufour, and M. Ieva et al. Inclusive ν_μ cc analysis using the entire ND280 detector. T2K internal document.

[72] B. Kirby. Status of ND280 muon neutrino spectrum measurement. T2K internal document.